R-08-25

HMCBG processes related to the steel components in the KBS-3H disposal concept

Lawrence Johnson, Paul Marschall, Paul Wersin
National Cooperative for the Disposal of Radioactive Waste (Nagra)

Peter Gribi, S+R Consult GmbH

May 2008

Svensk Kärnbränslehantering AB
Swedish Nuclear Fuel
and Waste Management Co

Box 250, SE-101 24 Stockholm
Phone +46 8 459 84 00

ISSN 1402-3091
SKB Rapport R-08-25

HMCBG processes related to the steel components in the KBS-3H disposal concept

Lawrence Johnson, Paul Marschall, Paul Wersin
National Cooperative for the Disposal of Radioactive Waste (Nagra)

Peter Gribi, S+R Consult GmbH

May 2008

Keywords: KBS-3H, Steel components, Gas effects, Hydraulic processes, Mechanical performance, Geochemical processes, Microbial activity.

This report is a result of a joint project between SKB and Posiva. This report is also printed as a Posiva WR report, Posiva WR 2005-04.

A pdf version of this document can be downloaded from www.skb.se.

Abstract

An analysis of the Hydro-Mechanical-Chemical-microBiological processes affected by Gas (HMCBG) related to the steel components of the KBS-3H disposal concept has been performed. The outcome of this study is foreseen to contribute to the KBS-3H Process Report for a repository for spent fuel sited at Olkiluoto.

Three different design options for KBS-3H are currently being studied (open tunnel option, two variants of tight distance block option). While the details of the design may influence the short to medium term performance, it is found that the medium to long-term evolution of KBS-3H is not significantly affected by the chosen design option, provided the distance blocks behave according to design.

Under repository conditions, the corrosion of the supercontainer will be fairly rapid. Complete conversion of Fe^0 to oxidised Fe^{2+}/Fe^{3+} species may occur within a few thousands of years. The main corrosion products will be magnetite and, depending on the groundwater composition, also iron sulphide and perhaps siderite. Furthermore, corrosion-derived Fe(II) may react with the clay to form Fe(II)-rich silicates. The supercontainer environment will thus experience a volume change and some loss of plasticity of the buffer between the supercontainer and the rock wall may occur. This might promote bacterial activity at the supercontainer surface, which would lead to an enhancement of localised corrosion and probably to destabilisation of the magnetite layer. Previous investigations indicate, however, that there will be no relevant bacterial activity in the main part of the buffer by virtue of its small pore sizes and low water activity.

In the course of time, the swelling pressure of bentonite will be affected by a number of processes, including magnetite formation, geochemical degradation, intrusion of bentonite into void space either initially present or created by relative displacement of distance blocks and supercontainer, and by subsequent bentonite erosion. The expected differential swelling pressure in the early stages of resaturation between inside and outside the supercontainer may lead to considerable forces acting on the perforated steel shell, causing elasto-plastic deformations and possibly rupturing of the shell.

Based on current understanding, a simplified model of gas pressure evolution and gas migration in the disposal system is developed. This model suggests that gas is predominantly transported by two-phase flow through the fracture network in the host rock. For the major part of the drift sections, there is sufficient transport capacity for gas to escape though the host rock and the calculated gas pressure increases are found to be moderate. In extremely tight drift sections, however, the maximal gas pressures may rise to values near or above the minimal principal stress. Under such conditions, reactivation of low-permeability fractures in the near-field rock and axial gas pathway formation through or around the distance blocks cannot be excluded.

Although no analyses of radiological consequences are performed in the framework of this report, it is concluded that the presented information can be used to perform an assessment of the safety-relevant impacts of the steel components in the KBS-3H disposal system. It is noted that gas generation will be finished after several thousand years, well before radionuclide migration is likely to occur from a container having an initial defect. Various mechanisms are capable of transporting the gas gradually through the host rock or through the tunnel system without significantly disturbing the isolation characteristics of the repository system.

Contents

1 Introduction

In 2002 SKB and Posiva carried out a feasibility study with the overall aim of developing the horizontal emplacement concept, KBS-3H, into a real alternative for the vertical emplacement concept, KBS-3V. The feasibility study included a preliminary assessment of the long-term safety, with the main focus on the buffer material in combination with the perforated disposal container containing the copper-iron canister and bentonite blocks around it.

The Basic Design phase of KBS-3H was completed in 2003 /Thorsager and Lindgren 2004/. The phase was divided into technical development, preparations for demonstration at Äspö and long-term safety studies.

The main activity in 2004 is the planning of the Safety Case and Process Report for KBS-3H. The present study is focused on the **H**ydro-**M**echanical-**C**hemical-micro**B**iological processes affected by **G**as (HMCBG) and is foreseen to contribute to the KBS-3H Process Report.

The work presented in this study concerns analyses of the HMCBG processes related to the steel components of the KBS-3H disposal concept. The main objective of the work is to produce a process report that identifies and provides information on the key long-term safety issues related to steel components of the KBS-3H disposal concept.

The work includes FEP analysis, process descriptions and the potential effects on subsequent radionuclide transport, and is focused on HMCBG processes (including corrosion, gas generation and release, and effects of corrosion products) related to the KBS-3H concept. The emphasis is on near-field aspects, although the detailed HM interactions associated with transport through a canister defect within the context of the defective canister scenario are not treated here. The overall effects of gas transport in and release from upper regions of the geosphere are not evaluated, though it is noted that leakage of large quantities of gas through several hundred metres of rock in the course of thousands of years may be perceived as a significant perturbation of the natural state of the site. Even if analysis of such processes shows that long-term safety is not compromised, the issue may have significance in the public presentation of the concept. The report is structured as follows: Chapter 2 contains a description of the reference system, including a short presentation of the design options currently under investigation. Chapter 3 is dedicated to FEP analysis, covering processes primarily related to the canister, buffer, supercontainer, distance block and the near-field rock. An interaction matrix is developed for post-closure assessment, including the saturation phase, assuming that radionuclides are not available outside the canisters. Chemical and biological issues are discussed in Chapter 4. This includes a discussion of the geochemical conditions in the near field and host rock, steel corrosion, iron/bentonite interaction and possible consequences on radionuclide transport. Chapter 5 contains the analyses of issues related to gas generation, gas pressure build-up and gas migration. Aspects related to the mechanical behaviour of the system (supercontainer, buffer, distance block) are discussed in Chapter 6. In Chapter 7, the system evolution is summarised and Chapter 8 presents the conclusions.

2 Reference system description

2.1 Introduction

KBS-3H requires a disposal system in which the bentonite buffer during and just after emplacement behaves according to a number of defined requirements /SKB 2004/. The chosen design should be simple and robust and its safety-relevant properties should be possible to verify in laboratory and in demonstration tests. A major objective of the overall project is to find out if the horizontal disposal concept will meet requirements equivalent to the vertical emplacement concept (KBS-3V).

The major commonalities and differences between KBS-3H and KBS-3V are as follows /Thorsager and Lindgren 2004/:

- General conditions (depth, environment, etc) should be the same for both the vertical and horizontal concept.
- Copper-iron canisters should be the same.
- Saturated bentonite buffer density should be the same.
- A perforated container ("supercontainer") for canister and bentonite buffer will be used for transport and deposition in KBS-3H.
- Zupercontainers will be placed in an array with bentonite blocks ("distance blocks") in between.

Three different design options for the distance block are under investigation (see Section 2.2). At the current stage of project development, no decision on the design option has been taken. In the present study of HMCBG processes, all three design options are addressed. In the subsequent sections, issues related to saturation of the deposition drifts and the relevant properties of the excavation-damaged zone (EDZ) and host rock are briefly discussed in turn.

A comprehensive set of input parameter values for the present study is given in Appendix A. These parameter values were approved by SROY on the 29.06.04. A summary of the most relevant parameter values is given in the following sections where appropriate.

2.2 Design options for distance blocks

Currently, three different design options for the distance blocks are being studied:

- Design option 1: Open tunnel option (Figure 2-1, /Börgesson et al. 2005/).

The open tunnel option involves centred distance blocks emplaced on steel feet and a slot of about 4 cm between distance block and drift walls. This allows free water flow on the bottom of the inclined drift in an initial phase after emplacement before swelling of the distance blocks is achieved. Preliminary analysis of the functioning of the system has raised a number of questions that are mainly related to the behaviour of the distance blocks under partially saturated conditions. In the more permeable drift sections, the effects of air humidity and water dripping from

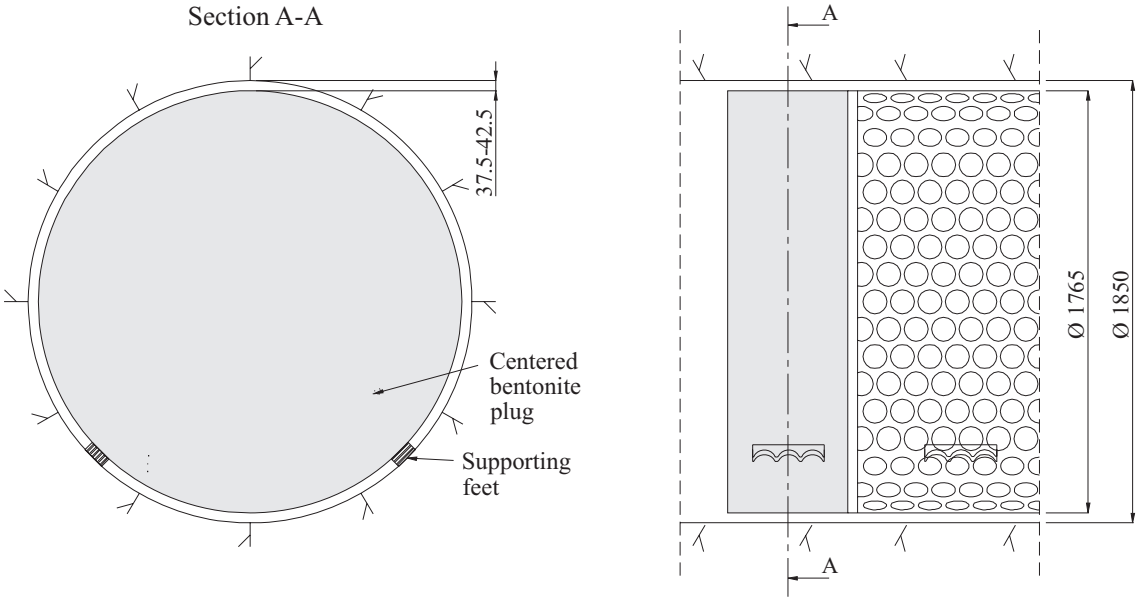

Figure 2-1. *Open tunnel option for the deposition drifts at Olkiluoto involving a centered distance block emplaced on steel feet with a slot of about 4 cm (design option 1) /Börgesson et al. 2005/.*

the drift walls on the bentonite blocks may lead to quick swelling of bentonite, gel formation and erosion of bentonite. If bentonite swelling occurs too quickly then one canister section may be pressurised before the neighbouring canister sections are properly emplaced. In such a case, large axial forces may exist leading to the displacement of the distance block and high axial hydraulic gradients may develop that could lead to the formation of pathways along the outside of the partially saturated/swelled bentonite (piping) and, as a consequence, bentonite erosion by flowing water may take place. Piping/erosion may also lead to dislodging pieces of bentonite, which could fall down and swell, thereby enhancing the effects of piping/erosion.

- Design option 2a and 2b: Tight distance block option (Figure 2-2, /Börgesson et al. 2005/.

An alternative design for handling the effects of piping/erosion due to water flows is to emplace distance blocks that rapidly come into contact with water, swell and thereby seal the slot between distance block and drift walls. This slot must either be very small (a few mm) or filled with sealing material to avoid piping/erosion phenomena when the water pressure within the emplaced canister section increases. Design option 2a involves a centred distance block with a slot of about 4 cm filled with bentonite pellets. A steel ring bolted to the rock counteracts axial forces induced by the rise of hydraulic pressure and by swelling of bentonite blocks. A second steel ring attached to the supercontainer keeps the pellets in place. Design option 2b involves a tightly fitted distance block formed of several conical pieces with a slot of a few mm, a steel ring bolted to the rock to counteract axial forces, but no steel ring attached to the supercontainer. Due to the relatively rapid sealing by swelling of the distance blocks, each canister section forms an individual hydraulic cell after a short period of time. It is noted that the effects related to water pressure increase and hydrostatic forces are much more pronounced for design options 2a and 2b than for design option 1.

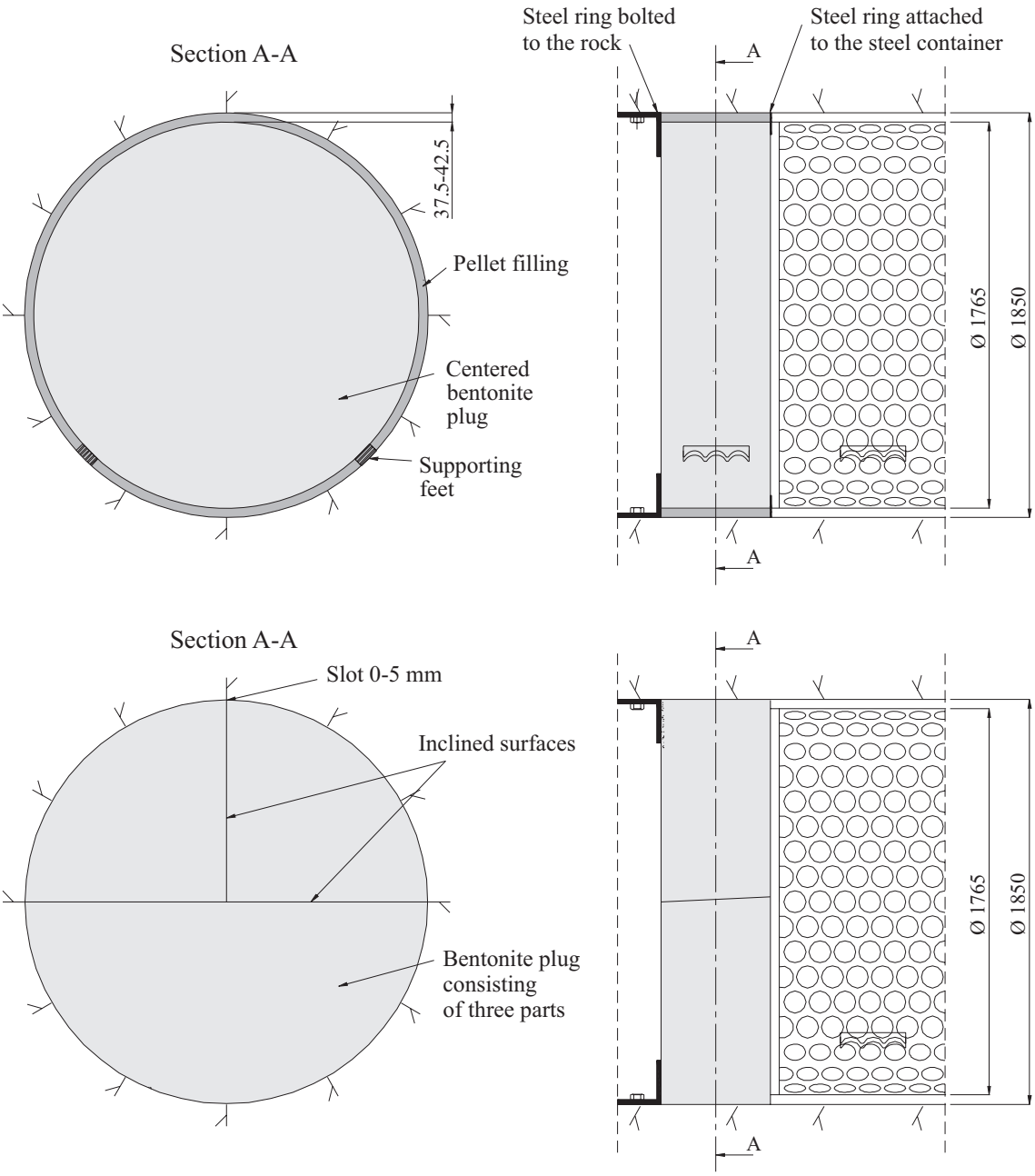

Figure 2-2. *Tight distance block options for the deposition drifts at Olkiluoto. Upper figure: Design option 2a (tight option with centered distance block and pellets kept in place by steel rings); lower figure: Design option 2b (tight option with tightly fitted distance block formed of several conical pieces) /Börgesson et al. 2005/.*

All design options are still under investigation. Changes to the design may be found necessary in the course of project development. The main characteristics of the three design options are summarised in Table 2-1. A comprehensive list of parameters used in the HMCBG study can be found in Appendix A.

Table 2-1. Main characteristics of the three design options.

Parameter	Unit	Parameter value		
		Option 1	Option 2a	Option 2b
Diameter of deposition drift	mm		1,850	
Diameter of supercontainer	mm		1,765	
Length of supercontainer	mm		5,546	
Length of distance block	mm		5,350 4,650 3,050 2,550	(BWR/Posiva) (PWR/Posiva) (BWR/SKB) (PWR/SKB)
Void slot between distance block and drift wall	mm	37.5–42.5	37.5–42.5	0–5
Supporting feet: distance block/supercontainer	–	yes/yes	no/yes	no/yes
Steel ring bolted to rock	–	no	yes	yes
Steel ring attached to supercontainer	–	no	yes	no
Total mass of steel per canister section	kg	944	1,557 (2,507)[1]	1,457 (2,407)[1]

[1] A more massive steel structure, with a weight of about 1,500 kg and also bolted to the rock, may be envisaged as a design variant in the options 2a and 2b.

2.3 Saturation of deposition drifts

After emplacement of the supercontainer, inflow of water from the host rock will lead to swelling of bentonite blocks and to sealing of the individual canister sections. This causes saturation of any void space in the deposition drift. The time needed for saturation of the deposition drifts depends on the chosen design option (open tunnel option and tight distance block option) and on the rate of water inflow and thus on the hydraulic conductivity of the host rock.

Saturation calculations were performed using a finite element program, Code_Bright, taking coupled thermohydraulic processes and water vapour transport into account /Börgesson et al. 2005/. For the tight distance block option, the saturation time was found to vary from 10–12,000 years, depending on the hydraulic conductivity of the host rock. For the open tunnel option, saturation starts only when the deposition drift is sealed, i.e. some extra time must be added (a few months). Two saturation regimes were identified by /Börgesson et al. 2005/: For hydraulic conductivities in excess of 10^{-11} m s^{-1}, the saturation time was found to be 10 years, irrespective of the hydraulic conductivity. This was attributed to the hydraulic resistance of the bentonite buffer. For rock hydraulic conductivities below 10^{-12} m s^{-1}, the saturation time increases continuously from about 10 years to 12,000 years, the longest saturation time corresponding to a hydraulic conductivity of 10^{-15} m s^{-1}.

In these calculations, the gas phase was held at constant atmospheric pressure and no gas generation and migration was assumed to occur. It has been noted that gas entrapment within the pore space of the near field could lead to longer saturation times. In fact, if gas generation is taking place sufficiently rapidly, then full saturation may not take place and a residual gas phase may remain in the near field. These issues will be discussed in more detail in Chapter 5.

2.4 Excavation-damaged zone

The excavation-damaged zone (EDZ) adjacent to the surface of KBS-3H deposition drifts may have an impact on the transport of gas and radionuclides. The damage is a result of rock tool impacts and stress relaxation. In addition to this type of damage, the rock around the deposition drifts undergoes deformation caused by the stress redistribution, which includes elastic deformation of rock and displacements of fractures intersecting the holes /Autio 1996, Autio et al. 2003/.

A number of samples were taken from the experimental deposition holes in the Prototype Repository Tunnel in Äspö HRL and Research Tunnel at Olkiluoto /Autio et al. 2003/. Based on these analyses, the EDZ adjacent to the walls of the experimental deposition holes can be divided into three different zones, starting from the excavated surface as follows:

- Crushed zone (adjacent to the excavated surface, thickness 4 mm).
- Microfractured zone (beneath the crushed zone, thickness 5 mm).
- Zone of minor damage (beneath the microfractured zone, thickness 14 mm).

The properties of these three zones as well as average properties for the entire EDZ are summarised in Table A-1 based on the results from the Research Tunnel at Olkiluoto. The investigations of the fracture network show that 90% of the fracture population in the crushed zone have apertures below 5.4 μm. Features with apertures above 5.4 μm are microfractures which form 10% of the fracture population and which are located randomly in the crushed zone. Fractures with apertures larger than 10 μm are mainly parallel to the excavated surface. These features are not directly connected to each other and do not form a continuous network. However, these larger aperture fractures are connected by fractures with apertures less than 5 μm. The mean fracture aperture in the crushed zone is 2 μm /Montoto et al. 1999, 2003/.

The microfractured zone and even more so the zone of minor damage are characterised by a smaller porosity, fracture density and fracture aperture. These zones are considered to be less important for transport of gas and radionuclides than the crushed zone.

The average porosity and intrinsic permeability of the EDZ are estimated to be 0.34% and 3×10^{-19} m^2 /Autio et al. 2003/.

The conceptual picture presented in Appendix D suggests that the hydraulic significance of the excavation-damaged zone around the underground structures is almost negligible. The total thickness of the damage zone is estimated to be 23 mm – it is possible that such an EDZ would diminish significantly in the post-closure phase due to self-sealing processes (e.g. drift convergence, swelling of backfill). Furthermore, any break in the axial continuity of this thin zone would prevent to a great extent groundwater or gas flow along the backfilled drifts.

On the other hand, the extent of the EDZ is subject to a variety of rock-specific and site-specific conditions as well as to the repository layout and engineering techniques applied (rock strength, rock stress at repository level, orientation and size of the drifts, excavation method). Comprehensive investigations have been conducted to characterise the EDZ around underground facilities in crystalline rock formations /Chandler et al. 1996, Emsley et al. 1997, Sugihara et al. 1996, Marschall et al. 1999/. There is general agreement that the effect of the EDZ on the hydraulic properties of the rock is restricted to a zone around the drifts, which is typically less than 1 m. In the EDZ, flow takes place preferentially along excavation-induced fractures where the connectivity of those EDZ fractures is strongly determined by site-specific conditions, as mentioned above. The EDZ conceptualisation summarized by Autio in Appendix D assuming a thin, homogeneous skin of enhanced hydraulic conductivity around the bored tunnels may therefore be seen as part of a wider spectrum of possible conceptualisations, including heterogeneous fracture network models of the EDZ /e.g. Marschall et al. 1999/. Fracture network models are of particular importance when gas transport phenomena are assessed, because transport properties (e.g. gas entry pressure) and transport mechanisms (e.g. pressure-dependent transmissivity) of fractured media may differ significantly from those of a homogeneous porous medium.

The analyses of gas behaviour are performed based on the reference values of Appendix D. To assess the role of the gas transport capacity of the EDZ, an impermeable EDZ is analysed in a special calculational case (see Chapter 5). The potential effects on gas behaviour of a more extensive EDZ have not been explored in the present study.

2.5 Host rock

Thorough investigations of bedrock fracturing at the Olkiluoto site have been conducted using several different methods (deep boreholes, outcrop mapping, surface trenches). The observed fracturing is divided into two classes: background rock and fracture zones. The densely fractured and hydraulically most active parts of the boreholes are interpreted as fracture zones with a typical fracture density of > 10 fractures per metre. The rock mass between fracture zones is further subdivided into sparsely fractured zones with a fracture density of 1–3 fractures per metre and jointed sections with 3–10 fractures per metre.

The general data on the host rock has been summarized in Appendix E. It includes water leakage rates into the deposition drifts during the operational and post-operational phase as well as geochemical data and thermal properties. More detailed data on fracture distribution properties are taken from /Poteri and Laitinen 1999/ and /Poteri 2001/, see Section 2.6.

More than 30 deep boreholes have been drilled today at Olkiluoto site and a large number of outcrops were investigated /Posiva 2003/. Generally, the boreholes are sparsely fractured (1–3 fractures per metre) and only 2.4% of the cumulative borehole length has more than 10 fractures per metre. Flow logging with measuring intervals of 10 m and 2 m was used to characterise the hydraulic rock properties along the boreholes. Of the 2 m intervals in the background rock about 90% are below the measurement limit of the flow logging tool (10^{-10} m s^{-1}).

The stress state at the Olkiluoto site has been determined for different depths. At 400 m, the maximal principal stress is 20 MPa with a dip of 30°, while the minimal principal stress is 9 MPa with a dip of 55°.

The most relevant data on the host rock at Olkiluoto is summarised in Table 2-2 and a comprehensive list is given in Table A-1.

Table 2-2. Relevant input data on host rock at a repository depth of about 500 m (Olkiluoto).

Parameter	Unit	Reference value	Alternative values	Comment/Ref.
Gneiss fracture properties				
Fracture type	–	fractures	vein-like	Appendix E
Density	m^{-1}	1–3	3–10	Appendix E
Orientation	–	several sets		Appendix E
Hydraulic transmissivity range (T)	m^2 s^{-1}	10^{-14} to 10^{-7}		/Posiva 2003/
Gneiss average matrix properties				
Porosity	%	0.14		Appendix D
Hydraulic conductivity	m s^{-1}	10^{-14}		Appendix D
Intrinsic permeability	m^2	5×10^{-21}		Appendix D
Leakage rates for 300 m drift				
Operational phase	l min^{-1}	0.1	1–10	Appendix E
Geochemical properties				
Salinity	g l^{-1}	10–25	25–45	Appendix E
Alkalinity	meq l^{-1}	0.4	0.1–1	/Posiva 2003/
pH		7.5–8.2		/Posiva 2003/
Redox potential	mV	–300..–250	≈ –200	/Posiva 2003, Pitkänen et al. 2004/

2.6 Conceptual model of the host rock on the canister scale

Modelling of groundwater flow in the bedrock surrounding the repository is conducted on three different scales to achieve the appropriate level of detail in each model /Poteri and Laitinen 1999/. The nested modelling approach comprises a regional model, a site scale model and a canister scale model. The canister model is a discrete fracture network model (DFN) with a block size of 40×40×40 m^3. For the gas release studies the canister scale model seems to provide an appropriate conceptual framework.

According to /Poteri and Laitinen 1999/ the DFN model is based on the following key assumptions:

- the fracture centres are located randomly in the modelling domain,
- fractures are planar structures with circular shape,
- fracture sizes and transmissivities are distributed log-normally,
- the statistical properties of the DFN are constant through the whole modelling volume.

The canister scale DFN model comprises three subsystems of fracture networks:

- background rock,
- excavation damage zone ,
- fracture zones.

/Poteri and Laitinen 1999/ provide a comprehensive discussion of the fracture statistics for each subsystem for various sites. Table 2-3 presents the representative DFN parameters for the Olkiluoto site. Of particular interest in the context of gas-related studies is the fact that the background fractures have been conceptualised in two alternative ways, namely as homogeneous or heterogeneous fractures. The consideration of the heterogeneous fracture concept was motivated by the experimental evidence, indicating unevenly distributed flow along fracture planes /Hakami 1989/. However, the experimental database was too small to provide reliable correlation functions for the internal distribution of transmissivity along the fractures. In the context of future gas related studies, internal heterogeneity of fractures may need further considerations, because gas release is governed by the internal connectivity of the high transmissivity channels.

Table 2-3. Fracture statistics of the DFN model.

Background rock	
Orientation	Quasi-isotropic
Intensity P_{32} [m^2 m^{-3}]	0.37–0.83
Size – mean radius and STD in [m]	0.9 ± 0.5
Transmissivity – mean log10 *T* and STD	–11 ± 2.5
EDZ (1 m thickness)	
Orientation	Horizontal
Intensity P_{32} [m^2 m^{-3}]	3
Size – constant radius in [m]	0.5
Transmissivity – mean log10 *T* and STD	–8 ± 0.05
Fracture zones	
Orientation	several sets
Intensity P_{32} [m^2 m^{-3}]	4
Size – mean radius and lognormal STD in [m]	1 ± 0.05
Transmissivity – mean log10 *T* and STD	–10 ± 2

The data in this table is based on data from the Olkiluoto site and is taken from /Poteri and Laitinen 1999/. Note that the data on the EDZ is from blasted tunnels and does not apply to KBS-3H deposition drifts.

3 FEP analysis

3.1 Definition of system

In this chapter, a FEP analysis is conducted for the KBS-3H repository near-field. The analysis is in line with the corresponding FEP analysis for KBS-3V discussed in /SKB 1999a/.

Note that in addition to the FEP analysis in /SKB 1999a/, extensive descriptions of all processes are compiled in a Process Report /SKB 1999b/ that supports the analyses and descriptions of the studied system within SR 97. This material was updated by Posiva in a separate Process Report for the spent fuel repository at Olkiluoto /Rasilainen 2004/. In the present report, it is not intended to repeat all the arguments and process descriptions in these two Process Reports. Rather, the aim is to add information that is specifically relevant to the KBS-3H design. This information (particularly the description of additional processes) is given in the various chapters of the present report (see roadmap in Table 3-3).

The part of the repository system covered by the FEP analysis contains the fuel, canister, buffer, supercontainer, distance block and the near-field rock. The perforated steel supercontainer and the distance block are specific to the KBS-3H concept. The canister, surrounded by bentonite blocks and supercontainer, is emplaced in horizontal deposition drifts. Reinforcements, in terms of plugs, rock bolts and grouts are also considered. The access drift system (shafts and adits) and the seals of the deposition drifts are not included. The near-field rock contains deposition drifts, and its outer boundary is taken to represent the distance from the drifts to which they influence the structure and behaviour of the surrounding rock. The interaction matrix is developed for the post-closure phase, including the saturation phase, assuming that no radionuclides have been released from the canister.

3.2 Interaction matrix

The procedure used to set up the interaction matrix is closely related to the procedure discussed in /SKB 1999a/. The interaction matrix consists of 13 diagonal elements and 156 off-diagonal elements. A short description of the diagonal elements is given in Table 3-1 and Appendix B contains the full description. The basis for Table 3-1 is Table 3-2 in /SKB 1999a/, with the following modifications:

- the diagonal element ‘Fuel’ is considered for consistency reasons with /SKB 1999a/, although the fuel contained in the canister is outside the scope of the present report (canisters are assumed to be unbreached),
- the diagonal element ‘Backfill’ (tunnel backfill in KBS-3V concept) is eliminated, because it is not relevant for the KBS-3H concept,
- two diagonal elements are added at the end of the table, namely ‘Supercontainer’ and ‘Distance block’. Note that the FEPs for the bentonite buffer and the distance block are similar (same material). In contrast to the bentonite buffer, however, only one diagonal element is foreseen for the distance block. In this element, only those FEPs specific to the distance block are listed, bearing in mind that all FEPs relevant for the bentonite buffer (elements 3.3, 4.4 and 5.5) also apply.

In the interaction matrix about 180 interactions are identified and assigned priorities. About 44% are red, 7% pink, 18% yellow and 30% green, the colour codings being related to the priorites (Table 3-2). The complete list of identified interactions with assigned priorities is given in Table B-1. In Figure 3-1 the graphical representation of the interaction matrix is shown. The colour coding is identical to the coding in /SKB 1999a/ and is explained in Table 3-2.

Table 3-1. Diagonal elements in the interaction matrix for KBS-3H (based on /SKB 1999a/, with new diagonal elements no. 12.12 and 13.13).

No.	Diagonal element	Short description
1.1	Fuel	Spent fuel and metal components of the fuel, such as Zircaloy cladding, fuel boxes, spacers, springs, grids etc of stainless steel and Inconel in the canister.
2.2	Canister	Copper canister with a cast iron insert in which the fuel is located.
3.3	Smectite/buffer	The buffer consists of smectite-rich clay (bentonite) and accessory minerals and impurities.
4.4	Buffer porewater	Water in the buffer that is in contact with the canister, supercontainer, smectite minerals, other clay minerals, non-clay minerals and impurities.
5.5	Non-smectite minerals/impurities	Non-smectite clay minerals and other mineral impurities as well as colloids and organics belong to this group.
6.6	Gas	All gaseous phases in the buffer (not inside the canister) and near-field rock, but excluding dissolved gas.
7.7	Temperature	Temperature evolution, temperature gradient, all expressed as functions of time after deposition of canisters in the drift. Temperature data for canisters, supercontainer, buffer and near-field rock.
8.8	Groundwater hydrology	Pressure, flow and properties of water contained in the near-field rock.
9.9	Groundwater chemistry	Composition and properties of groundwater in the near-field rock in terms of the content and composition of dissolved species, colloids and microbes.
10.10	Near-field rock	Structure, stress conditions, geometry and properties of the rock surrounding the deposition drift to a distance influenced by excavation.
11.11	Reinforcements	Construction materials, like concrete, cement and bentonite grouts, cement paste, steel reinforcement, and asphalt.
12.12	Supercontainer	Perforated steel supercontainer used for deposition in horizontal drifts, containing canister and bentonite buffer.
13.13	Distance block	Bentonite blocks emplaced between supercontainers for sealing purposes, kept in place by steel rings (options 2a/b only), the voids being possibly filled with bentonite pellets (option 2a). In contrast to the bentonite buffer, only one diagonal element is foreseen for the distance block and only those FEPs that are specific to the distance block are listed (see also explanation in text).

Table 3-2. Colour coding in the interaction matrix for KBS-3H and definition of priorities according to /SKB 1999a/.

Priority No.	Colour	Description
4	Pink	**Important interaction only in the water saturation phase – part of the Performance Assessment.** It can influence other parts of the process system included in this matrix, or other parts of the repository system not included in this matrix.
3	Red	**Important interaction – part of the Performance Assessment.** Could also influence other parts of the process system, (defined in this matrix), or other parts of the repository system. The interaction can be either a prerequisite for the PA or handled by assumptions or modelling efforts in the PA.
2	Yellow	**Interaction present – probably part of the Performance Assessment.** Limited or uncertain influence directly or via this interaction on other parts of the process system, or other parts of the repository system. However, this interaction can be in main focus in other matrices.
1	Green	**Interaction present – do not have to be considered in the Performance Assessment.** Negligible influence on other parts of the process system, (defined in this matrix) and other parts of the repository system.
0	White	No identified interactions

Figure 3-1. *Graphical representation of the interaction matrix for KBS-3H.*

3.3 Comparison of interaction matrix for KBS-3H and KBS-3V

The main differences between the interaction matrix for KBS-3H, as documented in this report, and KBS-3V /SKB 1999a/ are summarised in Table 3-3. In this table, additional FEPs related to gas issues, supercontainer and distance blocks are presented in turn. A complete comparison of interactions identified for KBS-3H and KBS-3V is given in Table B-1.

Table 3-3. Additional FEPs for KBS-3H related to gas, supercontainer and distance block. These FEPs are specific to the KBS-3H design, i.e. they do not appear in the interaction matrix for KBS-3V as discussed in /SKB 1999a/. The last column indicates where a description of the FEPs can be found in the present report.

No.	Additional FEPs	Section where FEP is discussed
	Additional FEPs for KBS-3H related to gas	
6.4	Gas diffusion/advection in bentonite porewater and possibly gas-induced water displacement	5.3.3
6.8/6.9/6.10	Gas diffusion/advection in groundwater Gas-induced displacement of groundwater in host rock/EDZ	5.3.3
6.12	Gas-induced pressurization of supercontainer	6.2.1
12.6	Gas generation by anaerobic corrosion of supercontainer	4.3, 5.2.2
13.6	Cut-off of gas pathways along drifts by swelling of distance blocks	5.3.3
	Additional FEPs related to supercontainer	
12.3	Resistance to swelling of smectite by supercontainer Volume expansion (magnetite formation) Fe/smectite interaction	6.2.1 4.4.3, 6.2.1 4.4
12.4	Ion release from supercontainer to bentonite pore water	4.4
12.5	Volume expansion (magnetite formation) Fe-silicate formation	4.4.3 4.4.2, 6.2.1
12.6	Gas generation by anaerobic corrosion of supercontainer	4.3, 5.2.2
12.7	Heat transport, heat radiation across gaps around supercontainer	6.2.3
12.8	Effect of supercontainer on water flow paths along the periphery of the drift	4.3.3, 6.2.1
12.10/12.11	Effect of expansion (magnetite formation) on host rock and reinforcements	6.2.1
12.13	Effects of supercontainer on distance blocks (similar to effects on buffer)	4.4
1.12	Effects of radiation on supercontainer	4.3.3
3.12	Effect of buffer swelling on supercontainer, breaching of supercontainer	6.2.1
4.12	Steel corrosion Pressurization of supercontainer by bentonite porewater	4.3 6.2.1
5.12/9.12	Steel corrosion	4.3
6.12/8.12/10.12	Pressurization of supercontainer by gas, groundwater and rock	6.2.1
7.12	Thermal effects on supercontainer (expansion/contraction, structural alterations, pressure changes)	6.2.3
13.12	Effects of distance blocks on supercontainer (similar to effects of buffer on supercontainer , see 3.12/4.12/5.12), additionally breaching of end plates	6.2.1
	Additional FEPs related to distance block	
13.3	Displacement of supercontainer/buffer by swelling of distance blocks	6.2.1
13.6	Cut-off of gas pathways along drifts by swelling of distance blocks	5.3.3, 6.2.2
13.12	Effects of distance blocks on supercontainer similar to effects of buffer on supercontainer (see 3.12/4.12/5.12), additionally breaching of end plates	6.2.1
3.13	Effects of buffer swelling pressure on distance block, including displacement of distance blocks	6.2.1
6.13/8.13 (8.3/8.5)	Piping and erosion by gas and water at interface with host rock	2.2, 5.3.3, 6.2.1

Note that in addition to the FEP analysis in /SKB 1999a/, extensive descriptions of all processes are compiled in a Process Report /SKB 1999b/ that supports the analyses and descriptions of the studied system within SR 97. This material was updated by Posiva in a separate Process Report for the spent fuel repository at Olkiluoto /Rasilainen 2004/. In the present report, the description of the additional processes identified for KBS-3H can be found in the relevant chapters, as indicated in the last column of Table 3-3.

3.4 Audit against the BENIPA FEP list for granite

The interaction matrix for KBS-3H has been derived from the corresponding analysis for KBS-3V discussed in /SKB 1999a/, as discussed in Section 3.1. In order to promote completeness of the FEPs listed in the interaction matrix for KBS-3H, an audit is performed against the independently-derived BENIPA FEP List /EC 2001/, which provides a comprehensive list of FEPs related to bentonite barriers in integrated performance assessment (see Appendix C).

The results of the audit can be summarised as follows:

- For the majority (33 out of 49 FEPs) of the BENIPA FEP list, one or several direct counterparts can be found in the interaction matrix for KBS-3H.
- For 9 BENIPA FEPs, only an implicit map to one or several elements in the interaction matrix for KBS-3H can be established.
- 6 BENIPA FEPs were found to be outside the scope of the present study (e.g. intrusion of buffer into failed canister, water turnover in canister, radionuclide transport, etc).
- 1 BENIPA FEP, related to the settlement or sinking of backfill (e.g. crushed rock and bentonite), was found not to be relevant for the KBS-3H concept.

4 Analysis of chemical and biological processes

4.1 General considerations

A large amount of reactive iron is introduced by the steel components within the KBS- 3H concept which, in principle, might affect the geochemistry of the near field (NF). Looking at the design of the engineered barrier, it appears reasonable to assume the largest impact on the NF from the supercontainer relative to the other iron components, such as the retaining ring. Table 4-1 gives the amounts of Fe from the supercontainer and the different iron fractions of the potentially affected bentonite buffer[1]. This comparison reveals that the predominant reduced iron fraction stems from the supercontainer.

The objective of this chapter is not to describe all possible chemical and microbial processes that may be influenced by the steel components, but rather focus on aspects that may be safety-relevant, such as:

- Influence on Eh conditions.
- Potential reduction of bentonite swelling capacity.
- Influence on sorption of radionuclides.
- Influence on microbial processes.

In order to be comprehensive, first the expected conditions in the host rock and the buffer without steel components are described. Then the corrosion process and its influence on redox conditions are outlined. The main emphasis is on the interaction of corroded species with the bentonite clay. We address this topic by evaluating the importance of the different processes with the aid of qualitative and quantitative considerations.

Table 4-1. Iron fractions of different components in the NF.

	Mass [kg]	kmol keq	Comments
Buffer			
Total bentonite material [a]	16,413		Dry density = 1.56 Mg m^{-3} ε = 0.44, length = 5,546 mm, thickness = 0.04 m, (dimensions given in Appendix A)
Montmorillonite [b]	12,309	30.4	75 wt %
Siderite, pyrite [b]	164	1.4	Assumption: 0.5% $FeCO_3$ and 0.5 FeS_2
Fe(III) oxide [c]	16.4	0.2	0.1% FeOOH
Structural Fe $^{3+b}$	338	6.1	
Structural Fe $^{2+b}$	16.9	0.3	
Cation exchange capacity [c]		3.5	75 meq/100 g
Edge sites [c]		0.5	15% of CEC
Steel supercontainer [a]	**869**	**15.6**	length = 5,546 mm, thickness = 8 mm, (dimensions given in Appendix A)

[a] Derived from Appendix A.

[b] /Müller-Vonmoos and Kahr 1983/ for Na-sat form: $Na_{0.30}(Al_{1.55}Fe^{3+}_{0.20}Fe^{2+}_{0.01}Mg_{0.24})(Si_{3.96}Al_{0.04})O_{10}(OH)_2$.

[c] /Bradbury and Baeyens 1997/.

[1] For reasons of conservatism, only the bentonite corresponding to the length of the container is considered and not that from the distance blocks.

Geochemical processes that were identified in the FEP analysis as being particularly relevant for the KBS-3H design (see Table 3-3) are also addressed in this chapter. Note that in Chapter 3, these processes are termed ‘additional FEPs for KBS-3H’, because they were not identified in the FEP analysis for KBS-3V. Table 4-2 inidcates in which sections these FEPs are described.

4.2 Expected conditions without steel components

4.2.1 Geochemistry of host rock

The geochemistry of the Olkiluoto site has been extensively investigated by geochemical and mineralogical analysis of a number of deep boreholes. /Posiva 2003/ and /Pitkänen et al. 2004/ give a comprehensive picture of the baseline conditions of the hydrogeochemistry based on chemical and isotopic analyses.

The hydrochemical evolution is complex and is strongly affected by the Quaternary history of the Baltic Sea. At least five different water types (recent meteoric, recent Baltic, ancient Baltic = Litorina, glacial melt water and very old brine water) have influenced groundwater compositions by various degrees of mixing. While the upper part is characterised by a dynamic hydraulic regime and a significant imprint of young meteoric waters, this is not the case for groundwaters below 300 m depth. These are characterised by glacial and older components. The salinity gradually increases from 300 to 500 m depth and the water type gradually shifts from Na-Cl to Na-Ca-Cl. Below 500 m, very old and highly saline waters (Ca-Na-Cl type) predominate.

The redox conditions are illustrated in Figure 4-1 (taken from /Pitkänen et al. 2004/). Microbially-driven sulphate reduction is the dominant redox reaction between 100 and 400 m depth, whereas methanogenesis, accompanied by high hydrogen levels predominates below 400 m. Isotopic data suggest that at around 400 m concomitant sulphate reduction and methane oxidation occurs. In this zone sulphide is enriched (a few mg l^{-1}), whereas Fe concentrations are low. These species are controlled by metastable FeS and perhaps partly also by pyrite solubility. Pyrite coatings in fractures are frequent and constitute about 7% of the average coating area /Pitkänen et al. 2004/. Below 400 m, sulphide concentrations drop to insignificant levels, whereas Fe concentrations show an increase with depth, reaching several mg l^{-1} in the brine-rich waters. Iron in the fracture fillings occurs predominantly in divalent state at greater depths and Fe(III) does not appear to play a significant role as an electron acceptor.

The estimated Eh values in the sulphidic zone are in the range of –200 to –250 mV with respect to the SHE. In the methanogenic (carbonate reduction) zone, the Eh is estimated to be about –300 mV.

Table 4-2. Additional FEPs related to the geochemical behaviour of KBS-3H. These FEPs are taken from Table 3-3. In the first row, the FEP number is given. The last column indicates where a description of the FEPs can be found in the present report.

No.	Additional FEPs for KBS-3H related to gas	Section where FEP is discussed
4.12/5.12/9.12	Steel corrosion	4.3
12.6	Gas generation by anaerobic corrosion of supercontainer	4.3, 5.2.2
12.3/12.5 (12.13)	Volume expansion (magnetite formation) Fe/smectite interaction Fe-silicate formation	4.4.3, 6.2.1 4.4 4.4.2, 6.2.1
12.4	Iron release from supercontainer to bentonite pore water	4.4
12.8	Effect of supercontainer on water flow paths along the periphery of the drift	4.3.3, 6.2.1
1.12	Effects of radiation on supercontainer	4.3.2

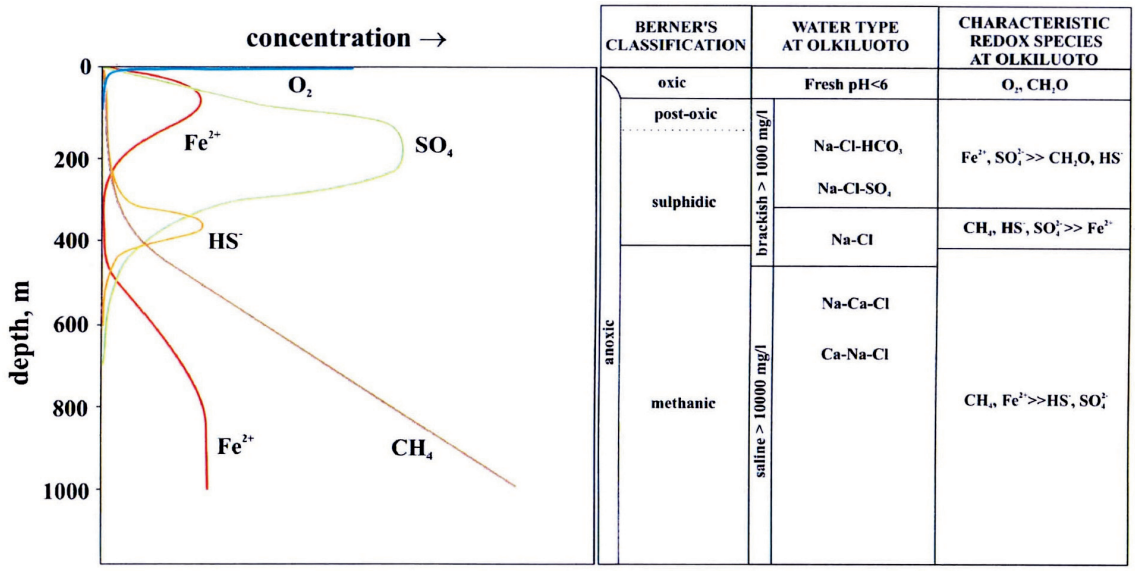

Figure 4-1. *Redox zones at Olkiluoto as function of depth /from Pitkänen et al. 2004/.*

Microbial studies on a few samples have been carried out /Haveman et al. 1998, 2000/ and more samples are currently being investigated. Microbial activity was found to be low, which is typical for nutrient-poor deep crystalline environments. Sulphate-reducing bacteria were generally the most abundant species, but iron reducers were also detected. The presence of methanogens and acetogens was noted, but, because of the low amount of cultivatable cells, interpretation of these data is hampered. The presence of autotrophic methanogens (which use inorganic carbon together with hydrogen) in saline samples, together with high amounts of dissolved hydrogen and methane gases, indicate that carbonate reduction is an important process at great depths.

Calcite is ubiquitous in fracture fillings and consequently groundwaters are close to saturation with respect to this mineral. pH values are generally in the range of 7.5–8.5. Alkalinity and DIC show an increase with depth at shallower levels due to respiration processes. At levels below 200 m, a significant decrease of these parameters is noted which has been explained by mixing of different waters and calcite precipitation /Pitkänen et al. 2004/. Ca concentrations follow the reverse trend, thus obeying the calcite equilibrium condition.

Besides calcite, clay minerals (illite, smectite, kaolinite, vermiculite, chlorite) make up most of fracture filling. As mentioned above, pyrite is also abundant, mainly as coatings on calcite grains.

Due to continuing postglacial uplift, it is expected that fresher water gradually displaces saline water towards depth until the next glaciation.

In summary, the pH conditions in the deep aquifer system at Olkiluoto are well buffered by the presence of abundant carbonate and clay minerals. This is also true for redox conditions, which are buffered by the presence of iron sulphides and microbially-mediated redox processes.

Effect of repository on redox conditions

The effect of the repository on the hydrologic and geochemical groundwater regime is subject to considerable uncertainty /Vieno et al. 2003/. It is expected that the construction of ONKALO at 400 m depth will lead to increased mixing of water types. In particular, a drawdown of sulphate-rich waters is envisioned /Posiva 2003/. By virtue of the large buffering capacity of the water-conducting fracture system, this should not lead to significant changes in Eh and pH

conditions. On the other hand, upconing of saline groundwater to the repository level due to repository construction or future glaciation effects also represents a viable scenario /Vieno 2000, Vieno et al. 2003/.

The inflow of massive amounts of oxic waters from the near-surface is unlikely, but has not been ruled out at this point /Posiva 2003/. This scenario is not treated in this report.

Table 4-3 gives the "reference" groundwater composition, as used in this report. It corresponds to the composition within the sulphate reduction zone, measured recently at about 360 m depth in the KR 13 borehole and is referred to as "brackish SO_4" /Pitkänen et al. 2004/. This is a somewhat arbitrary choice, but is deemed to reflect the expected composition reasonably well once the site is constructed and natural conditions have been restored. According to the ongoing evaluation of groundwater data by Posiva this water composition may reflect some mixing of different waters that occurred during sampling. However, for the purpose of this report this is not critical.

Also considered here are saline conditions (represented by a sample at 740 m depth from borehole KR12) and dilute/brackish water conditions (represented by a sample taken at 58 m depth from borehole KR6) as bounding compositions of the expected possible variations (Table 4-3).

Table 4-3. Compositions of groundwaters taken from selected measurements in /Pitkänen et al. 2004/. Calculated values obtained with PHREEQC. Concentrations in mmol l^{-1}.

	"Reference" water KR13/362/2	**Saline water [a] KR12/741/1**	**Dilute water KR6/58/1**
pH	7.8	8.3	7.54 [b]
log(pCO_2)	–3.56	–4.99	–2.34
Ionic strength (I)	162	1,180	20
Ca	22.6	268	2.15
Mg	2.28	1.56	1.07
Na	87.7	380	9.80
K	0.21	0.51	0.20
Cl	138	908	10.4
Alkalinity	0.786	0.137	3.44
$S(6)_{tot}$	1.26	0.056	1.31
$S(–2)_{tot}$	0.0157 [c]	0.0013	6E–4
Fe	9E–04	0.0038	0.024
CH_4(g) (ml l^{-1})	15.2	518.2	
Calc. parameters			
Eh	–233 mV S(6)/S(–2)	–299 mV C(4)/C(–4)	–35 mV $Fe(OH)_3$/Fe(2)
$SI_{calcite}$	0.12	0.57	0.00
$SI_{siderite}$	–3.48	–2.11	0.34
SI_{pyrite}	10.8	6.4	16.2
$SI_{FeS(ppt)}$	0.31	–0.11	0.0

[a] For this high I, the applied Debye-Hückel correction may induce uncertainties in calculated concentrations.

[b] Not measured; calculated from assumed equilibrium with calcite.

[c] The measured data indicated unrealistically high values. Therefore, the sulphide conc. was arbitrarily lowered by a factor of 10, which gives a typical value expected for this water.

SI = Saturation index.

4.2.2 Near field

Porewater composition of bentonite buffer

The reference buffer material is highly compacted Na-rich MX80 bentonite clay (dry density = 1.56 Mg m^{-3}). Under saturated conditions the main fraction of the interstitial water is "bound" water occurring in the interlayers and at the outer surfaces of the smectite and only a small fraction is "free", i.e. not affected by the clay surface charge. The thermodynamic properties of this porewater, being thus strongly affected by the electric double layer of the negatively charged clay particles, are not fully understood.

Nevertheless, simple thermodynamic models (that largely ignore these effects) appear to adequately describe the porewater composition. This has been shown for example by modelling of bentonite – water interaction experiments performed at VTT /Muurinen and Lehikoinen 1999/, which covered a large range of solid/liquid ratios. In fact, a modelling exercise performed by /Curti and Wersin 2002/ and /Wersin 2003/ revealed that experimental data could be simulated by conventional ion exchange and surface complexation models /Wanner et al. 1994, Bradbury and Baeyens 1997/. Furthermore, as shown by geochemical modelling, a high acid – base buffering capacity of compacted bentonite results from the high cation exchange and proton exchange capacity and the presence of calcite.

As a consequence, the bentonite porewater chemistry is expected to remain fairly stable over long time periods. The main change will be induced by the exchange of Ca for Na at the clay exchanger /Wanner et al. 1992, Bruno et al. 1999/. Irreversible processes caused by temperature gradients, such as illite formation or cementation, which would reduce the swelling capacity, are expected to be insignificant below 100°C /e.g. Pusch and Karnland 1990/.

Table 4-4 shows the porewater composition for bentonite equilibrated with the reference groundwater and the two alternative waters given in Table 4-3. The conventional model of /Bradbury and Baeyens 1997/, as applied by /Curti and Wersin 2002/, under the constraint of constant pCO_2 was used in this case. The assumption that pCO_2 is constrained by the rock is justified if long term conditions are considered, because diffusion of dissolved CO_2 in bentonite is fast relative to the timescales of interest (> 10,000 years).

The results indicate that, due to cation exchange and dissolution of calcite and gypsum, some changes in composition of the buffer porewater relative to the groundwater will occur. The changes are obviously greatest in the case of the bentonite contacting the "dilute" groundwater where the equilibrium with the ion exchanger will lead to increased cation concentrations. It is important to note, however, that because of strong buffering of the clay surface and the presence of calcite, the pH conditions will remain remarkably stable. The main change predicted for long timescales is enrichment of Ca relative to Na on the exchanger.

Redox conditions

Wyoming bentonite generally contains Fe(II) mineral impurities, such as pyrite and siderite /Müller Von-Moos and Kahr 1983/. In addition, traces of iron oxides /Baeyens and Bradbury 1997/ are present. Because of the variability in bentonite composition and possible oxidation of Fe^{2+} during processing of the raw material, the relative amounts of reactive iron phases may vary considerably. Moreover, the smectite fraction in MX80 typically contains about 2 wt% of structural iron, most of which is Fe(III) /Vogt and Köster 1978/.

The redox conditions in the near field will pass from oxic to anoxic after repository closure. The time frame of this transition will be rather short, as is indicated from simple bounding calculations. Thus, /Wersin et al. 1994/ calculated timescales for the vertical KBS-3 design on the basis of the reaction of O_2 with pyrite in the bentonite to range within 7 and 290 years. This estimate used a conservative pyrite oxidation model (shrinking core model) and neglected the O_2 migration and reaction in the host rock as well as reaction with the Cu canister. Moreover,

Table 4-4. Calculated bentonite porewater composition for three groundwater compositions. Concentrations in mmol l^{-1}.

	Reference water	Saline water [a]	Dilute water
pH	7.83	8.03	7.39
log(pCO_2)	–3.56	–4.99	–2.34
Ionic strength (I)	280	1,169	220
Ca	17.8	167	10.4
Mg	5.79	24.9	3.65
Na	243	645	167
K	0.76	2.3	0.53
Cl	139	924	15.1
Alkalinity	0.46	0.072	2.50
$S(VI)_{tot}$	42.5	11.9	74.2
$S(-II)_{tot}$	0.0157	0.0013	–
Fe	9E–4	0.0038	0.024
NaX	1,990	1,890	1,990
CaX_2	249	324	248
MgX_2	69.4	49.8	70.3
KX	23.3	22.1	23.5
SOH	220	203	250
SO^-	68.6	86.1	35.4
SOH_2^+	0.335	1.3	5.68
Eh (mV) magnetite/Fe^{2+}_{rock}	–188.1	–280.1	–201.7
Eh (mV) magnetite/siderite	–356.5	–493.6	–222.3
	Fe^{2+} = 0.07 mM	Fe^{2+} = 0.968 mM	Fe^2 = 0.04 mM
Eh (mV) magnetite/FeS	–186.3	–271.4	–203.3
	Fe^{2+} = 0.002 mM S(-II) fixed	Fe^{2+} = 0.004 mM S(-II) fixed	Fe^{2+}fixed S(-II) = 0.002 mM

[a] For this high I the applied extended Debye-Hückel correction may induce uncertainties in calculated concentrations.

microbially-mediated reactions in the host rock are expected to accelerate O_2 consumption rates, as was shown in the REX experiment at Äspö /Puigdomenech et al. 2001/. From these considerations, the timescale for O_2 depletion is likely to be a few years to a few decades.

Compacted bentonite acts as an efficient filter towards microbes. As shown by /Pusch 1999/ sulphate-reducing bacteria (SRB) are immobile in bentonite exceeding 1.9 Mg m^{-3} saturated density. Moreover, experiments performed by Pedersen and co-workers /e.g. Pedersen 2000/ showed that the activity of SRB in bentonite ceases at densities higher than 1.5 Mg m^{-3}. Studies performed by /JNC 2000/ confirmed that SRB introduced into bentonite surrounding steel samples had no effect on corrosion rates and were not cultivatable after the test. As a consequence, it is not expected that microbially-mediated sulphate reduction will occur in compacted bentonite.

The Cu canister will experience oxidative corrosion during the short oxic stage. Afterwards corrosion will be very slow and canister lifetimes are expected to exceed 100,000 years /e.g. King et al. 2001/.

4.3 Corrosion process of the steel supercontainer

4.3.1 Influence on depletion of residual oxygen

At first sight, it might seem that supercontainer corrosion traps most of the residual NF oxygen. However, considering that during the initial stage the heat from the canister will move the water front towards the outer side of the buffer, the cathodic reaction may be limited by slow diffusion, especially in case of low hydraulic conductivity of the host rock. Calculations performed for the Swiss design concept (initial bentonite dry density = 1.5 Mg/m^3; initial moisture content = 2%) under the assumption that O_2 is consumed entirely by steel corrosion at fully saturated conditions indicate timescales for oxygen depletion of about 20–50 years /Wersin et al. 2003/. This estimation is based on the assumption the O_2 depletion occurs entirely by inorganic reaction processes. As indicated from the REX experiment at Äspö, microbially-induced reactions are expected to lead to much shorter timescales (< 1 year).

From these considerations, it is unlikely that the steel supercontainer will significantly affect the timescales of oxygen depletion.

4.3.2 Corrosion rates and corrosion products

Iron is unstable in water and corrodes by forming an oxide-type surface layer. The corrosion of carbon steel under aerated conditions in the initial aerobic stage is relatively rapid, as has been pointed out in the previous section. Under anoxic conditions iron corrodes by the reaction with water according to the overall reaction:

$$3Fe + 4H_2O \rightarrow Fe_3O_4 + 4H_2 \qquad \text{(Equation 4-1)}$$

The reaction is shown for the corrosion reaction to magnetite, which is the corrosion product observed in the great majority of the experiments relevant to repository conditions. The formation of the protective oxide layer leads to a strong decrease in corrosion rate. This is shown by a number of corrosion experiments under a variety of solution conditions in which a significant decrease of the corrosion rates with time is noted. Thus, corrosion rates determined from weight loss and hydrogen production measurements show a decrease from 20 µm a^{-1} to less than 5 µm a^{-1}. This is illustrated in Figure 4-2 that was taken from a compilation of /Andra 2001/. The results suggest that the nature of anions (chloride, carbonate, sulphate) does not significantly affect corrosion rates under anoxic conditions.

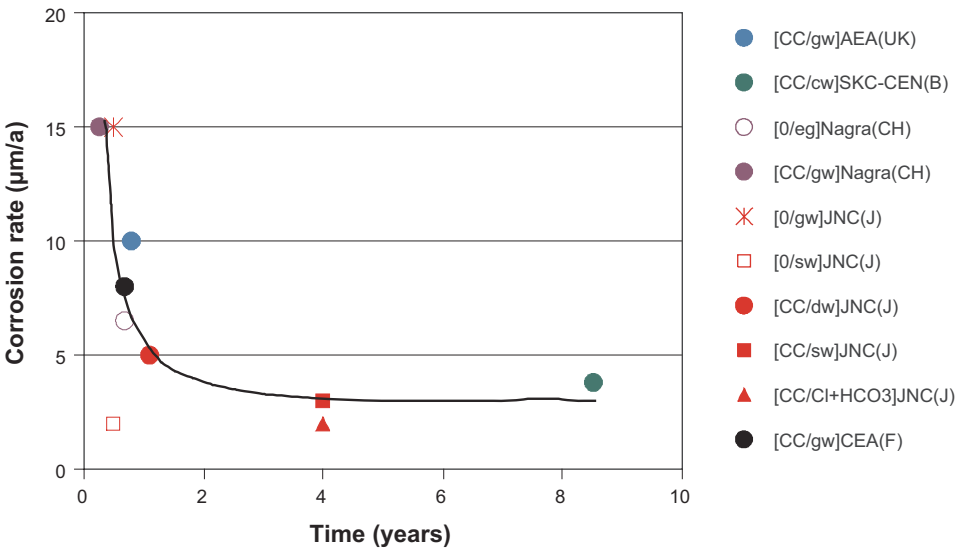

Figure 4-2. *Compilation of experimentally determined anoxic corrosion rates (modified from /Andra 2001/). CC: compacted clay; 0: immersion, gw: granite water; cw: clay water, sw: sea water, dw: distilled water.*

Recent corrosion experiments in different artificial groundwaters performed by /Smart et al. 2001/ within SKB's research program showed that anaerobic corrosion rates declined from the initial values of 10–30 μm a^{-1} to low values of 0.1 μm a^{-1} upon growth of a protective magnetite layer. The long-term rates showed no significant influence of temperature within the range of 30–85°C. Later experiments performed in compacted bentonite /Smart et al. 2004/ revealed higher rates compared to those obtained in water media. The corrosion rates obtained for a period of about 1 year were 1–2 μm a^{-1}. The rate increase was explained by slower build up of the protective magnetite film because of incorporation of released iron in the clay. This aspect is addressed in more detail below.

Since experimental studies can assess only a limited time frame, natural and archaeological analogues data can yield valuable information. A comprehensive review on archaeological analogues and corrosion by /David 2001/ demonstrates that the majority of iron objects experienced corrosion of 0.1–10 μm a^{-1}. This suggests low and relatively uniform long-term corrosion rates in very different geochemical environments.

Pitting

Pitting and crevice corrosion are favoured when the cathodic and anodic reaction are physically separated, which in turn results from heterogeneities within the material or gradients within the solution. For example, attack of the passivating oxide layer by chloride or sulphate leads to localised corrosion under oxic conditions.

The effect of pitting decreases with corrosion depth. This is evident from a compilation of pitting factors taken from laboratory studies and iron samples buried in soils for periods up to 15 years /JNC 2000/. This shows that pitting factors strongly decrease with corrosion depth. At a corrosion depth of 1 mm, the maximum pitting factors drop below 5 /Johnson and King 2003/.

Anaerobic corrosion of steel is much more uniform than that under aerated conditions and pitting factors are very low. Some pitting may occur in the presence of sulphide and/or the presence of microbes (see sections below).

Nature of corrosion products

The dominant anaerobic corrosion product that is experimentally observed under near-neutral and alkaline conditions is magnetite, which is a very stable and insoluble phase. The stability of magnetite increases with increasing temperature /Hermansson 2004/. Results obtained from /Smart et al. 2001/ indicate that magnetite occurs as a thin (< 100 nm) uniform inner layer and a porous outer layer.

Depending on solution conditions other Fe corrosion products may also form. Thus, at high concentrations of sulphide or carbonate, iron sulphide or siderite precipitation is expected:

$$Fe + HS^- + H^+ \rightarrow FeS + H_2 \qquad \text{(Equation 4-2)}$$

$$Fe + HCO_3^- + H^+ \rightarrow FeCO_3 + H_2 \qquad \text{(Equation 4-3)}$$

In addition, green rust type phases (double layer mixed Fe(III)/Fe(II) hydroxides) may form, which are expected to be metastable under conditions of interest with respect to magnetite and siderite /Génin et al. 1998/.

The stability fields of the different possible iron corrosion products under conditions representative of deep groundwater at Olkiluoto are presented in classical Eh-pH diagrams calculated for 25°C (Figure 4-3). This illustrates the stability field of magnetite at pH values higher than 8. FeS (Figure 4-3a) is also thermodynamically stable under conditions of the repository. On the other hand, pyrite (not shown here) has a much larger stability field; its formation however may be limited by slow kinetics. An indication that pyrite formation may not be relevant under repository conditions stems from the observed groundwater composition in the host rock,

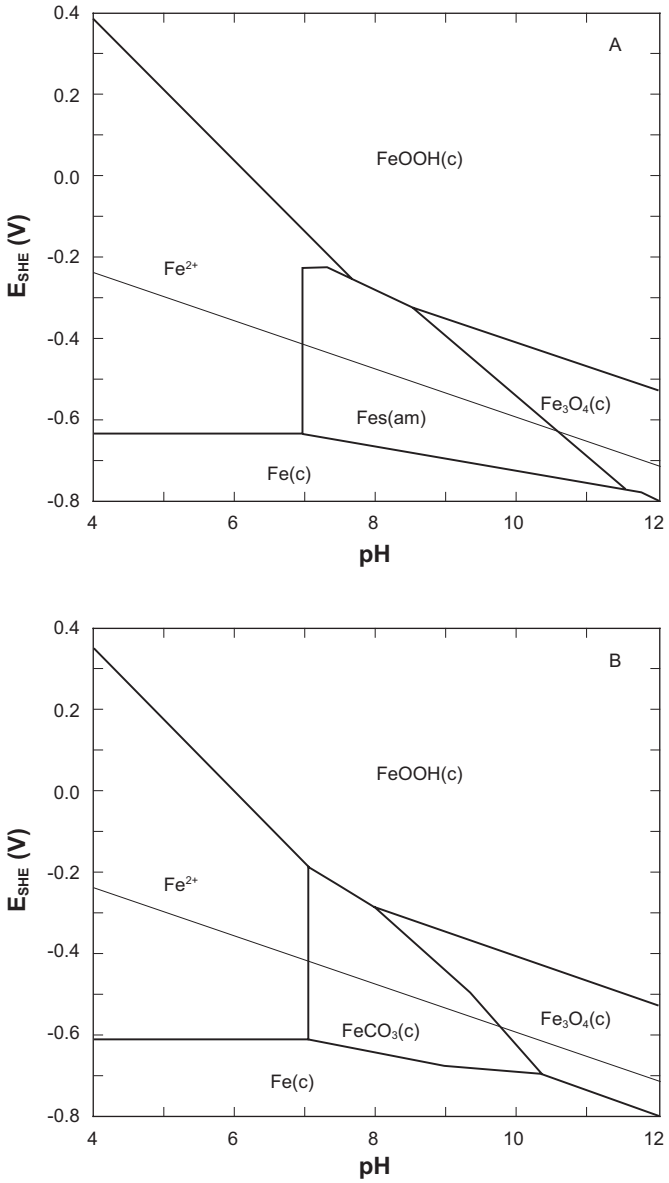

Figure 4-3. *pH-Eh diagram showing stability fields of potential corrosion products. a) Conditions representing sulphate reduction zone (Fe_{tot} = 10^{-5} M, HS_{tot} = 10^{-5} M, DIC = $5 \cdot 10^{-4}$ M, I = 0.1 M); b) Conditions representing iron reduction zone with low sulphide (Fe_{tot} = $5 \cdot 10^{-5}$ M, HS_{tot} = 10^{-6} M, DIC = 5 mM, I = 0.1 M). The dashed line is the H_2/H_2O boundary.*

which indicates equilibrium with FeS rather than with FeS_2 although pyrite is a very abundant fracture mineral at Olkiluoto. Although the temperature conditions in the near field will be somewhat higher than 25°C, the stability relationships of the iron phases are not expected to be significantly different.

Siderite formation is in principle also possible (Figure 4-3b) but requires high carbonate and low sulphide activities in the groundwater.

Observation from archaeological objects buried in sediments /David 2001/ showed the presence of magnetite and iron sulphides and to a lesser extent of siderite, on iron surfaces.

Besides hydroxide, sulphide and carbonate, Fe^{2+} from the corrosion reaction may react with dissolved silicate and the solid clay fraction. This reaction can be schematically written as:

$$Fe + H_4SiO_4 \rightarrow FeSiO_3 + H_2 + H_2O \qquad \text{(Equation 4-4)}$$

Little is known about the details of this process, such as the nature of the iron silicate phases and the thermodynamic and kinetic constraints. This aspect is discussed in detail in Section 4.4.

Effect of microbial activity

Microbial activity is known to influence iron corrosion. For example, the presence of sulphate-reducing bacteria (SRB) on the surface of steel may lead to increased attack by sulphide and thus affect the formation of the protective oxide layer. Moreover, iron-reducing bacteria (IRB) might be active by adhering to the magnetite layer and promoting reductive dissolution of the Fe(III) component /Kostka and Nealson 1995, Dong et al. 2000/. In addition, autotrophic methanogenic bacteria promoting degradation of inorganic carbon by using the hydrogen source could be envisioned to be active.

These three bacterially-mediated processes are probably occurring within the deep groundwaters at Olkiluoto (see Section 4.2.1). Hence, in principle, it is conceivable that these occur also in the supercontainer environment. The distance from the supercontainer to the rock wall is small (≈ 4 cm) and some reduction in swelling of the bentonite separating the supercontainer and host rock is expected from degradation of the swelling fraction (Section 4.4). Thus, microbial activity cannot be excluded, although the clay buffer is certainly not a very favourable environment.

The microbial effects on corrosion rates are not expected to be very large, as suggested from observation from archaeological analogues. If, for example, SRB were active at the supercontainer surface this would favour a sulphide precipitation layer which would also be protective against high corrosion. However, in this case increased pitting may occur /Johnson and King 2003/. Similarly, the build up of Fe^{2+} by IRB on magnetite-coated steel is limited by sulphide and siderite precipitation as well as by the slow dissolution kinetics /Dong et al. 2000/.

The impact of thriving methanogenic bacteria on corrosion is uncertain. Consumption of H_2 would occur and this might slow down the pressure build up of hydrogen gas. Reduction of inorganic carbon would limit siderite precipitation and, in the case of simultaneous sulphate reduction, counteract alkalinity increase.

4.3.3 Significance for the supercontainer environment

From the extensive corrosion data available, corrosion rates under anaerobic conditions are expected to be 1–2 μm a^{-1} in the compacted bentonite environment. The contribution of aerobic corrosion will not be significant. The lifetime of the steel under these conditions will be rather short. For a rate of 1 μm a^{-1} (R), the time for complete corrosion (t_c) can be calculated:

$$t_c = \frac{d}{2R} = \frac{0.008\,m}{2 \cdot 10^{-6}\,m/a} = 4000\,a \qquad \text{(Equation 4-5)}$$

where d is the thickness of the supercontainer.

Due to the attack by sulphide, possibly enhanced by microbial activity, significant pitting cannot be ruled out. Localised corrosion is also favoured by the geometric configuration of the perforated supercontainer (i.e. large number of machined holes). This, however, will not lead to a significant enhancement of the consumption rate of steel. On the other hand, the formation of a protective corrosion layer might also considerably slow down corrosion rates leading to an extended life time of uncorroded steel.

The nature of the corrosion products will depend on the composition of the groundwater. Because of the slightly alkaline conditions expected in all scenarios (pH = 7.5–8.5), an inner magnetite-type oxide layer will build up. The thickness of this layer, however, depends on the concentrations of other anions (sulphide, carbonate), the reactivity of the clay and the impact of microbial action. Under conditions of elevated sulphide concentrations, as expected for the reference water scenario, iron sulphide precipitation will be favoured (Equation 4-2).

In the case of upconing of saline waters (saline water scenario), less sulphide is available for competing for the corroded iron, thus less FeS will form relative to magnetite. In the dilute water scenario (zone of Fe(III) reduction), corroded Fe^{2+} may react to form siderite, although carbonate levels will probably not be very high. In all scenarios the clay may react with iron to form iron-rich clay. However, from a thermodynamic perspective, the extent will probably be less important when significant sulphide concentrations arising from sulphate reduction are available to bind Fe(II).

The thickness of the corroded layer, and thus the increase in supercontainer volume, depends on the molar volume of the corrosion phases. In case of magnetite the increase of volume is about a factor of two. For FeS and $FeCO_3$ the increase is 2.5 and 4.7 respectively. A much higher volume increase for corroded Fe incorporated in a silicate phase is calculated. Thus assuming the formation of berthierine (see next section) the volume increase is a factor of 8. This increase will, however, be largely compensated by the break down of the reacting clay. Under the assumption that all steel is converted to magnetite a decrease in porosity of about 2% would arise. This would lead to a slight increase in swelling pressure from 7 to about 8 MPa.

Because the area between the supercontainer and the drift wall is small (≈ 4 cm thickness) a significant fraction may be filled with iron corrosion products and Fe-altered clay (cf. next section). Due to volume expansion the total porosity in this area is likely to be decreased relative to the unaffected buffer. On the other hand, the corrosion may adversely affect swelling properties. The mechanical and hydraulic properties in the drift periphery are briefly discussed in section 6.2.1.

The effect of radiation on corrosion will be negligible, since the canister will retain its integrity for a very long time. Even in case of early failure of this near field component, no significant effect of radiation on the supercontainer is expected.

4.4 Interaction of Fe with bentonite

As pointed out in the last section, dissolved iron has a high affinity for the clay. This will manifest itself by sorption to the clay surface and/or precipitation of an iron-silicate phase. In the latter case the swelling smectite fraction might be affected. Unfortunately, these processes under repository-relevant conditions have received limited attention to date. This is evident from the recent review on this topic by /Marcos 2003/.

In this section, the main points of the review of /Marcos 2003/ are summarised and some new data are included. Based on this information, limiting cases are defined to estimate the maximum amount of clay adversely affected by Fe. Since the availability of Fe may be transport-limited, a coupled diffusion-reaction model is applied.

4.4.1 Sorption processes

Fe^{2+} derived from steel corrosion will sorb to the clay surface. Under reducing conditions, one can expect that the process of sorption to montmorillonite occurs like other metal cations such as Ni(II) or Zn(II) /e.g. Bradbury and Baeyens 1997/: i.e. by cation exchange in the interlayer and surface complexation to edge sites. This was, in fact, confirmed by a recent PhD study performed at the University of Grenoble /Tournassat 2003/. The sorption data could be adequately modelled with an ion exchange/surface complexation model. In general, sorption of Fe^{2+} was shown to be extremely strong, above pH values of 4. At low pH, Fe^{2+} was shown to sorb via cation exchange with a selectivity coefficient very similar to that of Ca^{2+}. At higher pH, surface complexation to edge sites was the dominant sorption process. At pH values above 7.5 the interaction process became more complex and both oxidation of Fe^{2+} and surface precipitation of a Fe(II) silicate phase were noted.

In a following paper, /Tournassat et al. 2004/ postulated that the oxidation of Fe^{2+} to Fe^{3+} at higher pH was not caused by molecular O_2 because care had been taken to avoid O_2 contamination and because desorption data indicated reversibility. The authors speculated that Fe^{2+} oxidation may have resulted from interaction with structural Fe(III) or by reduction of water. Oxidation of sorbed Fe^{2+} under anoxic conditions has also been reported in earlier work /Gerstl and Banin 1980/.

4.4.2 Formation of non-swelling Fe silicates

Brief introduction to Fe-rich phyllosilicates

Iron, as Fe^{3+} and Fe^{2+}, is one of the principal elements present in the clay lattice. Fe^{3+} generally substitutes for Al in dioctahedral positions, whereas Fe^{2+} replaces Mg^{2+} in trioctahedral positions. The replacement of Al^{3+} by Fe^{3+} in tetrahedral positions is far less frequent. The Fe^{3+}/Fe^{2+} ratio is representative of redox conditions during the formation of the clay.

In the 1:1 clays (kaolinite/serpentine group), there are four iron-rich mineral groups /Lantenois 2003/:

- **Greenalite** $(Fe^{2+},Fe^{3+})_{2-3}Si_2O_5(OH)_4$: Iron occurs mainly as Fe^{2+} in trioctahedral position. Greenalite is found in low grade metamorphic rocks.
- **Berthierine** $(Fe^{2+},Fe^{3+},Al,Mg)_{2-3}(Si, Al)_2O_5(OH)_4$: Iron occurs mainly as Fe^{2+} in trioctahedral position. Substitutions of Fe^{2+} by Fe^{3+} are mainly compensated by the tetrahedral charge deficit related to Al^{3+}–Si^{4+} substitutions. Berthierine is the most common of the iron-rich 1:1 clays. It is formed in un-metamorphosed marine sediments and lateritic and polar soils.
- **Odinite** $(Fe^{3+}, Mg, Al, Fe^{2+})_{2.5}(Si,Al)_2O_5(OH)_4$: Iron occurs mainly as Fe^{3+} in dioctehdral position. The trioctahedral position is occupied mainly by Mg^{2+}. Odinite is formed in marine sediments and is a common precursor for chlorite formation.
- **Cronstedtite** $(Fe^{2+},Fe^{3+})(Si,Fe^{3+})O_5(OH)_4$: This trioctahedral mineral is the most iron-rich of this mineral family. One out of three Fe^{2+} is substituted by Fe^{3+}. It frequently occurs as an alteration product of iron-rich meteorites and in low temperature hydrothermal sulphide rocks.

In 2:1 clays, iron occurs in three mineral families:

- *Smectites:* Iron is far less abundant than in 1:1 structures. Fe^{3+} is the predominant oxidation state; it replaces Al^{3+} mainly in octahedral position in dioctahedral smectites (montmorillonite, beidellite). The iron-rich end member of dioctahedral smectite is **nontronite,** with the formula $(Ca_{0.5},Na)_{0.3}(Fe^{3+})_2(Si,Al)_4O_{10}(OH)_2$, whose negative charge is induced by tetrahedral substitution of Al^{3+} for Si^{4+}. Because of steric hindrance and the larger size of Fe^{3+} relative to Al^{3+} in the octahedral cavity, montmorillonites normally contain little iron. In the trioctahedral smectite series, Fe^{2+}-rich **saponite** $(Ca_{0.5},Na)_x(Fe^{2+},Mg)_3(Si_{4-x},Al_x)O_{10}(OH)_2$ may form in marine sediments and as alteration products from volcanic glass in reducing environments /Güven 1988/.
- **Chlorites** are the most abundant iron-rich phyllosilicates, but they are usually formed at temperatures above 150°C. Iron occurs predominantly as Fe^{2+} in the octahedral position. Chamosite $(Fe^{2+},Mg^{2+},Fe^{3+})_5Al(Si_3Al)O_{10}(OH,O)_8$ is the most iron-rich member.
- *Micas:* The iron-rich member is **glauconite**, $(K,Na)(Fe^{3+},Al,Mg)_2(Si,Al)_4O_{10}(OH)_2$, a dioctahedral mica, in which Fe^{3+} predominates in the octahedral position. Glauconite is found in low temperature environments, such as marine sediments.

Indications from experiments

Relevant experimental data, namely on the interaction of Fe^0 or Fe^{2+} with dioctahedral smectite, are rare. /Müller-Vonmoos et al. 1991/ investigated the interaction of montmorillonite with magnetite and iron powders at 80°C for about half a year. They found no evidence of Fe uptake by the clay or transformation of the expandable fraction.

The effect of an Fe(II) silicate on bentonite properties under oxic and anoxic conditions was examined by /Oscarson and Heimann 1988/. They found a decrease in CEC and an increase in Fe^{2+}/Fe^{3+} for reacted samples under anoxic, but not under oxic conditions. The result was interpreted as precipitation of Fe-hydroxide at clay edges.

There is some early reported work on the formation of hydroxyl interlayers (chloritisation) in smectites at low temperatures /Rich 1968, Carstea 1968, Carstea et al. 1970/. These studies suggest that Al-hydroxy interlayer complexes may be stable, whereas Fe-hydroxy layers are poorly developed and, furthermore, require particular conditions (e.g. low pH). At conditions more representative of the NF, the formation of separate Fe (hydr)oxide phases was reported in the aforementioned studies.

Recently, the topic has received attention within the French radwaste program, which supported various PhD theses, such as /Habert 2000, Guillaume 2002/ and /Lantenois 2003/. /Habert 2000/ investigated the interaction of FoCa clay with iron powders at 25 – 200°C under aerated conditions. He identified berthierine as a newly formed phase exhibiting a slight excess of Fe^{3+} over Fe^{2+}, as well as Fe(III) oxides. The study of /Guillaume 2002/ involved interaction of MX80 bentonite with iron plates and magnetite at 300°C under N_2-degassed conditions for nine months. The results indicated dissolution of montmorillonite and neo-formation of iron-rich chlorite, saponite, quartz, feldspars and zeolite /Guillaume et al. 2003/. The pH after the reaction dropped to rather low values (5–6).

The most relevant data for the purpose of this report were obtained from the study of /Lantenois 2003/, who contacted smectites of variable Fe content with iron powders and degassed distilled water at 80°C for 45 days. The results indicated dissolution of smectite and formation of magnetite, an iron-rich clay phase (Fe^{2+}/Fe^{3+} ratio ≈ 1), and an iron silicate gel (Fe^{2+}/Fe^{3+} ≈ 0.25). The newly formed iron clay was identified to be a 1:1 clay with a composition close to cronstedtite. The conversion reaction was dependent on the initial Fe^{3+} content in the octahedral position, the expandability of the clay and the presence of a tetrahedral charge in the starting smectite. Thus, the reaction with Fe-rich nontronite (which contains a substantial tetrahedral charge deficit) was most extensive, followed by beidellite (less Fe^{3+} than nontronite), and then montmorillonite. Iron-poor saponite did not react within the experimental time period. Smectite samples which had been exchanged with K^+ showed much less reactivity than the Na^+ and Ca^{2+} dominated ones.

The above results are very interesting in the light of KBS-3H, but some care needs to be taken for their interpretation. The experiments were performed at a very low S/L ratio and smectite/Fe ratio in order to maximise the reactivity. Moreover, the author states that some oxygen had entered into the reaction vessels and thus conditions were not anoxic[2]. Finally, the studied system was free of sulphide and carbonate and therefore no competition reactions involving these species occurred.

Information from natural analogues

Useful natural analogue information is very limited /Marcos 2003/. Some insight can be gained from diagenetic smectite-rich systems. To our knowledge, there are no indications from these systems of direct conversion of dioctahedral montmorillonite to non-expandable iron-rich clays. Instead, the formation of chlorite rather involves breakdown of Mg and Fe-rich trioctahedral smectite (saponite), usually via the formation of mixed layer (e.g. corrensite). This transition

[2] This might explain why Fe^{3+}-rich cronstedtite formed instead of more Fe^{2+}-rich berthierine.

occurs in diagenetic systems at temperatures of 150–200°C, which is about 50°C higher than the lower temperature for smectite-to-illite reaction. The formation of berthierine as intermediate phase may be involved in the transition of saponite to chlorite /Mata et al. 2001/.

Interesting natural analogues are altered meteorites rich in metallic iron (chondritic meteorites). A quick literature search, however, did not allow any conclusive statements on this topic. Nonetheless, some reported observations are of interest. The primary material consists of metallic iron containing variable amounts of Ni, which is embedded in a silicate spherulitic matrix. Main alteration products include various iron sulphides. Once sulphur is depleted, iron-rich silicates, such as cronstedtite, berthierine, chlorites and Fe-rich smectites have been reported to form /Zolensky and McSween 1988, Tomeoka et al. 1989/. A thorough literature review on the subject would be useful to obtain more comprehensive information on the interaction between iron and clays under reducing conditions.

4.4.3 Reduction of structural Fe^{3+} in smectites

There is abundant literature on the reduction of structural Fe^{3+} in smectites. Most of the recent experimental work has been performed by Stucki and co-authors, who investigated the reduction of smectite with dithionite /e.g. Stucki et al. 1984ab, 2000/ and with bacteria /Kostka et al. 1996, 1999/. The Fe^{3+} reduction resulted in an increase in layer charge, a decrease in swelling pressure and decrease in particle surface area. The charge deficit resulting from Fe^{3+} reduction has been shown to be compensated by adsorption of an exchangeable cation and/or dehydroxylation of structural OH^-. The detailed mechanism, however, is still controversial /e.g. Heller-Kallai 1997, Drits and Manceau 2000/.

It has been proposed that reduction may lead to lattice destabilisation and migration of Fe^{2+} to vacant sites to form high energy domains, thus further destabilising the crystal structure /Drits and Manceau 2000/.

/Shen et al. 1992/ studied the effect of iron reduction of nontronite and montmorillonite on hydraulic conductivity by using sodium dithionite as reducing agent. The results indicated a significant increase in hydraulic conductivity for both minerals upon reduction of structural Fe^{3+}. However, the results depended on the "consolidation" history. Samples that were reduced in suspension and then consolidated to dry densities of about 0.15 Mg m^{-3} showed a slight decrease in hydraulic conductivity, whereas samples that were reduced under consolidated conditions showed the reverse behaviour. The difference was explained by differences in pore size distribution caused by the different treatments.

4.4.4 Significance for the bentonite buffer

From the above sections it becomes clear that there is a serious lack of data concerning the effect of reduced iron on the bentonite buffer. Both the reduction of structural Fe^{3+} and the conversion of smectite to a non-swelling clay would affect the integrity of the buffer. As suggested by the work of /Lantenois 2003/, structural Fe^{3+} reduction is a necessary step for the conversion reaction to proceed. Based on the scarce experimental data and indications from sedimentary systems, a Fe^{2+}-rich 1:1 clay, such as berthierine is the most likely Fe silicate to form under repository conditions (reducing, low temperature). Considering the lack of evidence at the temperatures of interest (< 85°C), the formation of a chlorite phase appears less likely. Because of the reducing environment in the near field, the formation of an Fe^{3+}-rich smectite (nontronite) also seems unlikely.

The extent of conversion of montmorillonite to a non-swelling silicate phase depends on sulphide and carbonate levels in the system because of competing iron sulphide and siderite formation. This aspect is further addressed in the next section.

The role of corrosion-derived H_2 in the reduction of structural Fe^{3+} is unclear due to the complete lack of data. If H_2 triggered such a process, the swelling pressure may be lowered.

A further point to consider is the effect on surface properties of the buffer from sorption of Fe^{2+} with or without concomitant oxidation and surface precipitation of Fe(III) /Tournassat et al. 2004/. This could affect both sorption of radionuclides (Section 4.5) and swelling properties due to cementation effects /Oscarson and Heimann 1988/.

Due to the large uncertainties involved in the extent of the iron – smectite interaction and the absence of kinetic data, we will assess the problem by quantitative analysis with limiting cases, based on mass balance and transport considerations.

4.4.5 Quantitative considerations

Mass balance considerations

The amount of iron that may potentially react with the buffer is large, as illustrated in Table 4-1. Thus, from the point of view of sorption there is a clear excess of supercontainer-derived Fe with regard to cation exchange capacity and of course even more so with regard to the edge sites (Table 4-1). Owing to its low solubility and moderate selectivity, Fe^{2+} is not expected to occupy a significant proportion of the cation exchange sites. On the other hand, Fe^{2+} has a very strong affinity for the edge sites of the clay. This aspect is evaluated in the section below using a transport model and the data in Table 4-5.

An instructive calculation is the maximum amount of smectite in the buffer that could be converted to a non-swelling Fe(II) silicate. This estimate was done by assuming the conversion of montmorillonite and iron to berthierine via the simplified overall reaction:

$$1.5Fe^0 + 0.5[Al_2Si_4O_{10}(OH)_2] + 3H_2O \Rightarrow Fe_{1.5}AlSi_2O_5(OH)_4 + 1.5H_2 \qquad \text{(Equation 4-6)}$$

The calculation indicates that conversion of all supercontainer-derived Fe to berthierine would result in a decrease of 15% of montmorillonite based on mass balance considerations. The reduction in swelling pressure induced by such a loss of expandable clay can be estimated by the relationship between effective clay density and swelling pressure /e.g. Dixon and Miller 1995/. The effective clay density (ρ_{eff}) for the altered buffer is calculated according to the formula /JNC 2000/:

$$\rho_{eff} = \rho_d\,(1–R)/((1–\rho_d) \times R/\rho_{ns}) \qquad \text{(Equation 4-7)}$$

where ρ_d is the dry density of the clay (1.56 Mg m^{-3}), R is the mixing ratio between the non-swelling and swelling fraction (0.15) and ρ_{ns} is the grain density of the non-swelling clay (2.78 Mg m^{-3}, assumed to be the same as montmorillonite). The calculated ρ_{eff} is 1.45 Mg m^{-3} compared to 1.56 Mg m^{-3} for the non-reacted bentonite. This would produce a loss in swelling pressure from 8 to about 4 MPa according to the density-swelling pressure relationship /e.g. Dixon and Miller 1995/.

In the case of the saline water scenario, swelling pressures may be further reduced somewhat. Taking the saline water (Table 4-3, sampled at Olkiluoto at a depth of 740 m) with a salinity of 50 g l^{-1}, the swelling pressure would be decreased by a factor of about 2 relative to moderately saline conditions /Dixon 2000, Karnland 1998/. There is nonetheless, even in these extreme bounding cases, substantial remaining swelling capacity.

Introducing the transport aspect

The above estimates were based on the assumption of uniform distribution of Fe in the buffer and no transport limitation for Fe^{2+} availability. As is shown subsequently, this assumption is not realistic, because of slow diffusion, strong interaction of Fe^{2+} with the clay and the low concentration gradient between the corroding source and the buffer.

Table 4-5. Sorption and solid phase equilibrium reactions used in the transport modelling.

Reaction	$\log K^0$	Reference/Comments
Cation exchange		*CEC = 2.66 eq l^{-1}*
$NaX + Ca^{2+} \Leftrightarrow CaX_2 + 2Na^+$	0.415	/Bradbury and Baeyens 1997/
$NaX + K^+ \Leftrightarrow KX + Na^+$	0.60	"
$2NaX + Mg^{2+} \Leftrightarrow MgX_2 + 2Na^+$	0.342	"
$NaX + Fe^{2+} \Leftrightarrow FeX_2 + 2Na^+$	0.415	/Tournassat 2003/
Surface complexation		*SOH_{tot} = 0.399 eq l^{-1}*
$S_sOH + H^+ \Leftrightarrow S_sOH_2^+$	4.5	/Bradbury and Baeyens 1997/
$S_sOH \Leftrightarrow S_sO^- + H^+$	–7.9	"
$S_{w1}OH + H^+ \Leftrightarrow S_sOH_2^+$	4.5	"
$S_{w1}OH \Leftrightarrow S_sO^- + H^+$	–7.9	"
$S_{w2}OH + H^+ \Leftrightarrow S_sOH_2^+$	6.0	"
$S_{w2}OH \Leftrightarrow S_sO^- + H^+$	–10.5	"
$S_sOH + Fe^{2+} \Leftrightarrow S_sOFe^+ + H^+$	5.0	/Tournassat 2003/
$S_{w1}OH + Fe^{2+} \Leftrightarrow S_{w1}OFe^+ + H^+$	0.5	"
Solids		
$CaCO_3 \Leftrightarrow Ca^{2+} + CO_3^{2-}$	–8.48	PHREEQC Database
$CaSO_4\,2H_2O \Leftrightarrow 2H_2O + Ca^{2+} + SO_4^{2-}$	–4.58	"
$SiO_2 + 2H_2O \Leftrightarrow H_4SiO_4$	–3.98	"
$FeS(ppt) \Leftrightarrow Fe^{2+} + S^{2-}$	–3.915	", used as input Fe for case A
$FeCO_3 \Leftrightarrow Fe^{2+} + CO_3^{2-}$	–10.89	", used as input Fe for case B
$FeSiO_3(model) + 2H_2O \Leftrightarrow Fe^{2+} + H_4SiO_4$	2.8	Fe^{2+} activity fixed at 10^{-8} M in bentonite, see text

The Fe^{2+} concentration at the source will be constrained by the low solubility of corrosion products, which in the reference and saline water scenarios are expected to be magnetite and iron sulphide. This will limit Fe^{2+} concentration to a few μmoles l^{-1} (cf. Tables 4-3 and 4-4). In the dilute water scenario there might not be enough sulphide to precipitate Fe^{2+}, in this case the maximum Fe^{2+} concentrations would be constrained by siderite solubility. The Fe^{2+} concentrations would then be in the range of 10–50 μmoles l^{-1} (cf. Tables 4-3 and 4-4).

The Fe^{2+} concentration in the buffer porewater, that is not affected by the corroding supercontainer, depends on the presence of Fe(II) impurities. If, for example, there are sufficient FeS impurities, the Fe^{2+} concentrations will be in the same range as released from the source containing iron sulphides. Thus, there will be barely any concentration gradient and diffusion of supercontainer-derived Fe^{2+} will be exceedingly slow. If there are sufficient siderite impurities then the Fe^{2+} concentrations in the buffer porewater will exceed those at the source and there will be a transport of Fe^{2+} towards the supercontainer until all $FeCO_3$ is consumed. The only significantly unfavourable situation arises in the case where there is only insoluble pyrite or no Fe(II) impurities at all to dissolve in the buffer. In the latter case, some Fe^{2+} from the clay fraction would dissolve. The solubility of Fe^{2+} under such conditions is not known, because the controlling phase is not known and, moreover, the thermodynamic database for Fe^{2+}-containing phyllosilicates is of rather poor quality.

Under conditions of a concentration gradient between the supercontainer and the buffer the diffusion of Fe^{2+} will be retarded by sorption and precipitation reactions. From the above sections it is obvious that very little is known about the possible precipitation processes. On the other hand, there are some useful sorption data, which can be applied to a sorption model /Tournassat et al. 2004, Charlet and Tournassat 2004/.

Defining two limiting cases for diffusion-reaction calculations

Diffusion-reaction calculations were performed under the assumption of unfavourable Fe^{2+} concentration gradients outlined above. Two cases were considered. In case A, the iron source at the supercontainer was assumed to be controlled by amorphous FeS solubility (with Fe_{tot} = 4 μmoles l^{-1}) and a porewater composition corresponding to the saline water scenario. In case B, the siderite solubility constraint (Fe_{tot} = 40 μmoles l^{-1}) and porewater composition corresponding to the dilute water scenario was applied.

For both cases, two types of calculations were performed. In the first calculation, only sorption of Fe^{2+} was considered, taking the initial Fe^{2+} concentration in the bentonite porewater equal to zero. In the second calculation, precipitation of Fe^{2+} with SiO_2 was accounted for by assuming precipitation of a hypothetical $FeSiO_3$ compound that fixes the Fe^{2+} activity at 10^{-8} M and the SiO_2 activity at quartz equilibrium. The amount of the SiO_2 component in the bentonite was arbitrarily set at 10% of the montmorillonite content. We emphasise that the assumptions for this precipitation model are speculative because of lack of process knowledge, but it is illustrative to compare the results of the two calculation types (sorption only vs. sorption and precipitation).

The basis for the geochemical modelling was the thermodynamic bentonite model described in /Curti and Wersin 2002/ which was briefly presented in Section 4.2.2. The considered sorption and mineral equilibrium reactions and the corresponding logK values are given in Table 4-5. The sorption reactions of Fe^{2+} to the clay were included by applying the data of /Tournassat 2003/.

Diffusive transport was simulated with aid of a one-dimensional diffusion-reaction model:

$$\varepsilon \frac{\partial C}{\partial t} = D_e \frac{\partial^2 C}{\partial x^2} - \varepsilon \frac{\partial q}{\partial t} \qquad \text{(Equation 4-8)}$$

where C (mol kg^{-1} porewater) is the species concentration, t is the time (s), x is the distance (m), D_e is the effective diffusion coefficient (m^2 s^{-1}) and q is concentration in solid phase (mol kg^{-1} porewater). The modelling was performed with the PHREEQC Version 2 code /Parkhurst and Appelo 1999/, which solves transport by an explicit finite difference scheme. The chemical interaction term $\partial q/\partial t$ is computed separately for each time step and corresponds to the change in concentration in the solid phase.

The buffer is represented by a 40 cm wide column, divided into four cells (Figure 4-4). At the front end, a constant concentration boundary condition $C(0,t)=C_0$ (corresponding to the porewater in equilibrium with the corroded supercontainer) is imposed. In case A the composition corresponding to the reference water scenario (Table 4-4) and the Fe^{2+} concentration is imposed by FeS solubility. The composition of the dilute water is assumed for case B and Fe^{2+} concentration is imposed by $FeCO_3$ solubility.

At the back end, closed boundary conditions ($\partial C(40cm,t)/\partial x = 0$) are assumed. A uniform diffusion coefficient of $2 \cdot 10^{-11}$ m^2 s^{-1} is assumed for all species /Yu and Neretnieks 1997/. At $t = 0$ the Fe^{2+} together with the other species start to diffuse through the cells while reacting with the clay surface sites (that were pre-equilibrated with groundwater in a previous step) and the accessory minerals.

Results from diffusion-reaction calculations: major ions

Calculations were first performed without including the iron component. The results thereof indicate relatively minor changes of the main composition with time for both cases A and B (data not shown). There is some exchange of Ca for Na during the first few thousand years, which is mainly due to dissolution of gypsum. Once this phase is depleted insignificant changes occur. The pH conditions remained constant within 0.1 units for both cases.

Calculations including Fe sorption and precipitation reactions did not lead to significant changes of major ions or pH.

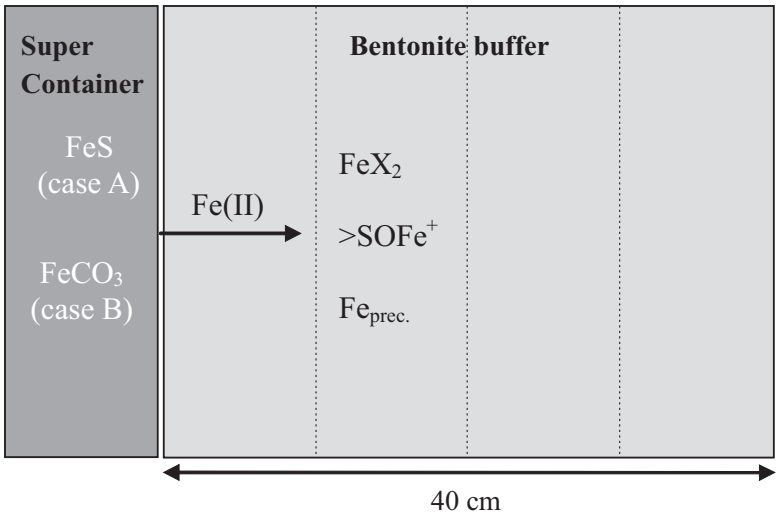

Figure 4-4. *Representation of supercontainer-buffer system in diffusion-reaction model.*

Results from diffusion-reaction calculations: including Fe sorption

The calculated Fe migration behaviour for cases A and B is illustrated in Figures 4-5 and 4-6. For case A (control of Fe(II) source by FeS eq.) the diffusion proceeds at a very slow rate. Thus, the breakthrough of the Fe sorption front at a penetration depth of 15 cm occurs after about 400,000 years. The breakthrough at the centre of the buffer (i.e. the Cu canister) occurs about 200,000 years later. Note that there is a considerable time lag between the sorption and dissolved Fe front because of the very high affinity for the clay surface.

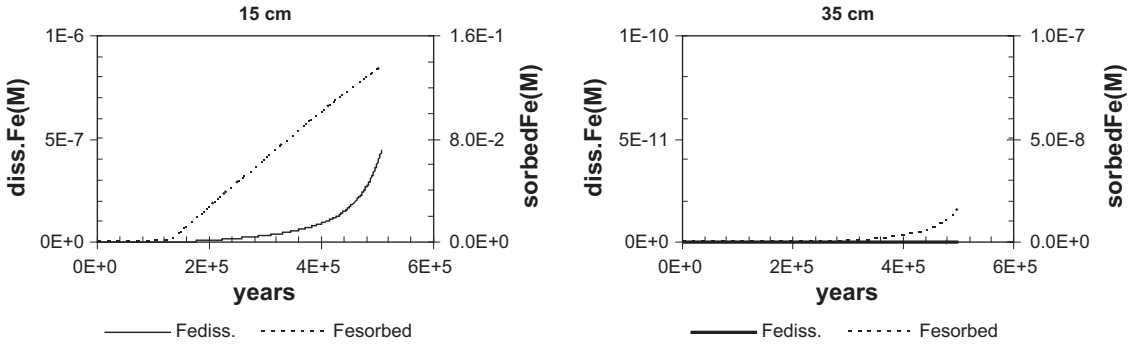

Figure 4-5. *Breakthrough curves of Fe(II). For* ***case A*** *at 15 cm (left) and 35 cm (right) distance from the supercontainer; only sorption considered.*

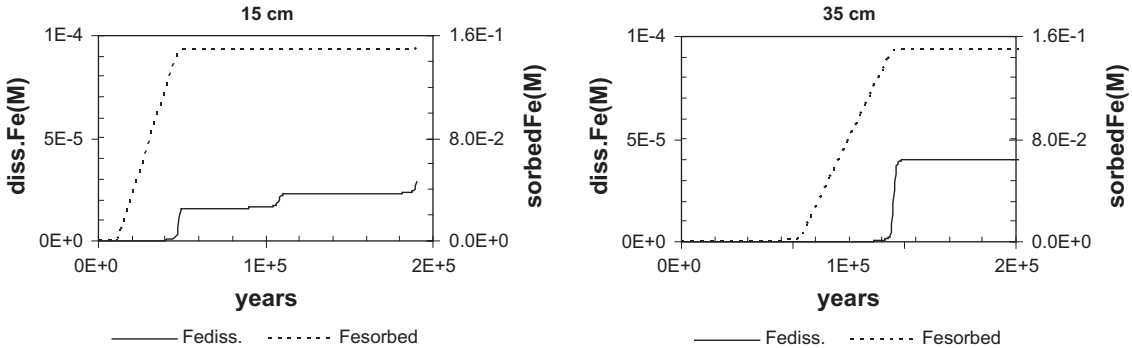

Figure 4-6. *Breakthrough curves of Fe(II). For* ***case B*** *at 15 cm (left) and 35 cm (right) distance from the supercontainer; only sorption considered.*

For case B (control of Fe(II) source by $Fe(CO_3)$ eq, the diffusion is not as slow because of the steeper concentration gradient. Thus, breakthrough of the sorption front is predicted to occur after about 30,000 and 150,000 years for 15 and 30 cm depth respectively. Nevertheless, the results indicate very effective retardation of iron even for this unfavourable case.

The model predicts for both cases that most of the Fe is sorbed to the edge sites and only a small fraction is bound to the ion exchanger.

Results from diffusion-reaction calculations: including Fe sorption and Fe(II) silicate precipitation

The Fe migration is now retarded by both sorption and precipitation. As illustrated in Figures 4-7a and 4-8a for cases A and B, transport of Fe is slowed down even more relative to the previous calculations considering sorption only. Most of the Fe(II) diffusing from the supercontainer is immobilised by the precipitation reaction and only a small fraction by sorption to the clay surface. This is visualised in Figure 4-7b and 4-8b, which shows the Fe fluxes (shown as % of the supercontainer iron) after 100,000 years. For case A only about 3% of the canister-Fe has moved into the buffer, whereas this fraction amounts to 30% for case B. At this time, almost all Fe is tied up in the outer 10 cm of the buffer.

The precipitation of a Fe(II) silicate phase produces acidity which will, however, be compensated by calcite dissolution and proton exchange reactions at the clay surface.

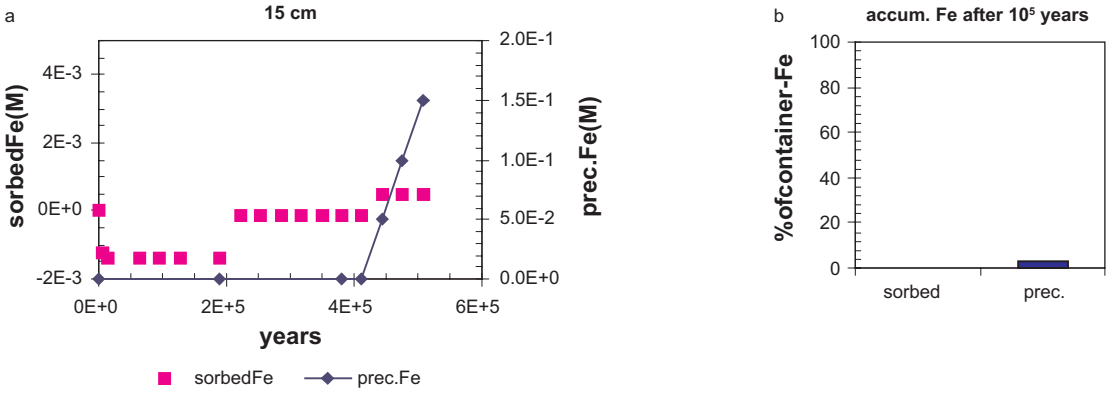

Figure 4-7. *Modelled data considering sorption and precipitation for* ***case A****. a) breakthrough curves at 15 cm distance, b) accumulated Fe in buffer after 10^5 years, shown as % of available supercontainer-derived Fe.*

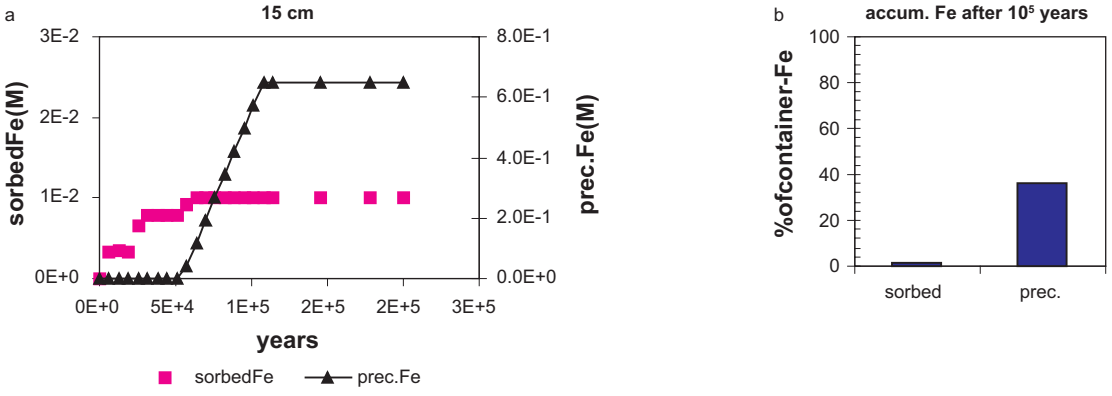

Figure 4-8. *Modelled data considering sorption and precipitation for* ***case B****. a) breakthrough curves at 15 cm distance, b) accumulated Fe in buffer after 10^5 years, shown as % of available supercontainer-derived Fe.*

The discretisation (cell length) was selected to be coarse in order to save computer time. Some test runs were made with increased numbers of cells, which indicated that results were affected, i.e. the retardation of Fe increased by factor of 2–3. Because of this "favourable" result and the large uncertainty related to the Fe-clay interaction processes, we did not repeat all the transport calculations using a finer discretisation.

In summary, the diffusion-reaction calculations indicate very slow migration of Fe^{2+} derived from the supercontainer. In spite of the large uncertainties related to the interaction process between Fe and the clay, the results of these limiting cases illustrate the effective constraint imposed by diffusion and the low concentration gradient. The latter arises from (i) the geochemical properties of the system and (ii) the strong affinity of Fe for the clay.

4.5 Interaction of radionuclides in "corroded" NF

In this section, we discuss potential effects for radionuclides interacting with Fe-affected bentonite. The transport aspect discussed above is not considered here.

The cation exchange properties of the smectite might be affected by the interaction with reduced iron. However, the information in the literature on this issue is ambiguous. The investigations of Stucki and co-workers /e.g. Stucki et al. 1984a/ indicate an increased CEC upon reduction of structural Fe^{3+} in montmorillonite, which was explained by increase in layer charge. On the other hand, a decrease of CEC of bentonite upon interaction with Fe^{2+} was reported by /Oscarson and Heimann 1988/ which was explained by cementation effects induced by Fe hydroxide precipitation. In fact, a decrease of CEC is also likely if significant amounts of montmorillonite react with Fe to form a non-swelling Fe-rich clay.

Regardless of the uncertainties about the development of CEC, sorption properties of the bentonite should not become less favourable. In the case of CEC increasing due to layer charge increase, the general sorption affinity is expected to increase. In case of CEC decrease by formation of Fe hydroxide at clay edges or by conversion of smectite to a non-swelling clay, no adverse effect on sorption properties is expected. In fact, this would increase the number of edge sites or oxide-type sorption sites, which are known to play an important role in metal sorption.

The strong sorption of Fe^{2+} might make sorption of other RN less favourable due to competition effects. In fact, short-term Fe^{2+}-bentonite interaction data of /Tournassat et al. 2004/ indicate weaker sorption of Zn^{2+} in the presence of Fe^{2+} under mildly acidic conditions. However, the data from the same authors indicate enhanced sorption of Zn^{2+} at pH values above 7.5 because of concomitant formation of a reactive iron silicate surface precipitate, which is in line with the data reported by /Oscarson and Heimann 1988/. Based on this limited information, strong competition between Fe^{2+} and other RN for sorption sites under NF conditions appears unlikely.

The generation of the corrosion products magnetite, FeS (and perhaps $FeCO_3$) and Fe(II) silicates will considerably enhance the reducing capacity of the buffer adjacent to the supercontainer. This area can act as sink for redox sensitive RN, such as U, Se and Tc, that may have escaped the canister in oxidised form. The capability of surface-bound Fe^{2+} to reduce and immobilise redox active RN has been shown for U(VI) /e.g. Cui and Spahiu 2002/, Se(IV/VI) /Myneni et al. 1997, Cui et al. 2003/ and Tc(VII) /Lee and Bondietti 1983, Cui and Eriksen 1996/.

4.6 Summary of relevant chemical and biological processes

The corrosion of the supercontainer will be fairly rapid. Complete conversion of Fe^0 to oxidised Fe^{2+}/Fe^{3+} species may occur within a few thousands of years. The main corrosion products will be magnetite and, depending on the groundwater composition, also iron sulphide and perhaps siderite. Furthermore, corrosion-derived Fe(II) may react with the clay to form Fe(II)-rich silicates. The supercontainer environment will thus experience a volume change and some loss of plasticity of the buffer between the supercontainer and the rock wall may occur. This might promote bacterial activity at the supercontainer surface, which would lead to an enhancement of localised corrosion and probably to destabilisation of the magnetite layer.

Previous investigations indicate that there will be no relevant bacterial activity in the main part of the buffer by virtue of its small pore sizes and low water activity.

Fe(II) derived from the corrosion process has a high affinity for the clay which will lead to sorption and precipitation (perhaps with simultaneous oxidation) of Fe(II). This, in turn, may affect the smectite fraction by conversion to an iron-rich non-swelling clay. From the sparse data available, it appears that the most likely Fe silicate to form under repository conditions is berthierine (a non-swelling 1:1 clay). The extent of such a conversion of a swelling clay to a non-swelling one is not known because of lack of reliable experimental and thermodynamic data. A very pessimistic scenario, in which all supercontainer-derived Fe is used for the conversion of smectite to berthierine, leads to an estimated conversion of 15% of the swelling clay fraction. The resulting loss in swelling pressure would be about 50%. Alternatively, a slight increase in swelling pressure in the case that most of the steel is converted to magnetite is also a viable possibility.

There are several factors that will limit the extent of Fe-clay interaction. First, the precipitation of insoluble iron phases (magnetite, FeS_{1-2} and perhaps siderite) will compete for Fe. Second, transport of Fe is limited by diffusion. Third, the diffusive flux into the buffer, which depends on the concentration gradient of Fe^{2+} between the corroded source and the buffer, is expected to be small. Moreover, this gradient will be effectively lowered at the reaction front by the strong interaction of dissolved Fe(II) with the clay. This was shown by coupled diffusion-reaction calculations using two limiting (unfavourable) cases. These modelling results indicate that the flux of Fe into the buffer will be small. The largest flux would arise from a relatively soluble $FeCO_3$ source and concomitant low Fe^{2+} activity in the porewater of the unaffected buffer. However, even in this case no significant effect for the buffer would be expected for at least 10^5 years.

The pH conditions will not be significantly altered by the Fe – clay interaction because of the acid-base buffering capacity of the bentonite. Redox conditions will be changed by the corrosion process and the reducing capacity of the Fe-affected clay will be enhanced by the presence of Fe(II)-rich corrosion products. This will promote reductive precipitation of oxidised species, such as U(VI) or Se(IV/VI), if they have managed to escape from the canister environment.

The sorption properties of the buffer will very probably not be adversely affected by its interaction with supercontainer-derived iron. The formation of non-swelling clays or Fe hydroxide phases produced would increase the fraction of reactive edge sites.

There exists a large uncertainty with regard to process understanding of the Fe-bentonite interactions and their effects on physical properties of the buffer. From the considerations presented in this report we cannot, however, envision any serious effects on the integrity of the buffer. Nevertheless, it appears reasonable to perform well designed experiments in order to gain a better level of process knowledge. Such experiments should focus on the potential effects on swelling pressure and permeability. One aspect that deserves particular attention is the effect of high hydrogen pressures on the physical and chemical properties of the bentonite buffer. In addition, it would be useful to spend more effort on coupled reactive transport modelling, by specifically evaluating Fe silicate precipitation.

5 Analysis of issues related to gas

5.1 General considerations

Gas generation in a deep geological repository may take place by various processes, including anaerobic metal corrosion, microbial degradation, radiolysis and formation of volatile fission products. This chapter provides an overview of all relevant issues on the fate of gas produced in the KBS-3H deposition drift, taking into account the different design options as defined in Chapter 2.

The analysis includes a calculation of the gas production rates (Section 5.2), an estimate on the capacity of the repository system to dissolve and store the produced gases and model calculations on the gas pressure build-up and migration mechanisms, taking the properties of the fracture network into account (Section 5.3).

In this chapter, special attention is paid to the gas-related processes, listed in Table 5-1, that were identified in the FEP analysis as being particularly relevant for KBS-3H design (see Table 3-3). Note that in Chapter 3, these processes are termed ‘additional FEPs for KBS-3H’, because they were not identified or discussed from a different viewpoint in the FEP analysis for KBS-3V.

5.2 Gas production

5.2.1 Quantities of gas-generating materials

In the framework of the KBS-3H design concept, steel corrosion is expected to be the only relevant process for gas generation in the time period before canister breaching. This is because organics and gas-generating metals other than steel are absent and because the intact SF canister provides a complete containment and shields the environment against radiation. Any air initially trapped in the deposition drifts at the time of closure will be either dissolved or compressed in the course of time.

Table 5-1. Additional gas-related FEPs for KBS-3H. These FEPs are taken from Table 3-3. In the first row, the FEP number is given. The last column indicates where a description of the FEPs can be found in the present report.

No.	Additional FEPs for KBS-3H related to gas	Section where FEP is discussed
12.6	Gas generation by anaerobic corrosion of supercontainer	4.3, 5.2.2
6.4	Gas diffusion/advection in bentonite porewater and possibly gas-induced water displacement	5.3.3
6.8/6.9/6.10	Gas diffusion/advection in groundwater	5.3.3
	Gas-induced displacement of groundwater in host rock/EDZ	
13.6	Cut-off of gas pathways along drifts by swelling of distance blocks	5.3.3
6.13/8.13 (8.3/8.5)	Piping and erosion by gas and water at interface to host rock	2.2, 5.3.3, 6.2.1

The masses of steel per SF canister are given in Table 5-2 for the different design options envisaged in the KBS-3H design concept. Included in Table 5-2 are the total mass of steel for the supercontainer, the feet, the ring bolted to the rock (including rock bolts) and the ring attached to the supercontainer. For options 2a/2b, an alternative value for the mass of the ring bolted to the rock is also given, corresponding to a design variant involving a more massive steel structure. The average steel thickness for the steel rings is assumed to be 10 mm, independent of the design variant considered. 10 steel feet (each weighing 3.75 kg) are envisaged for the superconductor and another 10 identical feet for the distance block (design option 1 only). For the average steel thickness of the feet, a value of 6 mm is used. Note that the use of lower bounds for the average steel thickness yields a pessimistic estimate of the gas production rate (see Equation 5-3).

5.2.2 Gas generation by anaerobic steel corrosion

The anaerobic corrosion reaction for pure iron and carbon steel can be written as

$$3Fe + 4H_2O \rightarrow Fe_3O_4 + 4H_2 \qquad \text{(Equation 5-1)}$$

The total amount of H_2 produced per SF canister, n [mol can^{-1}], is calculated as follows:

$$n_{tot} = \frac{4}{3}\frac{m}{M} \qquad \text{(Equation 5-2)}$$

where

m total mass of steel per canister [kg can^{-1}]

M molar mass of steel [kg mol^{-1}]

The rate of H_2 production per SF canister, $\dot{n}$ [mol a^{-1} can^{-1}], is calculated as follows:

$$\dot{n} = \frac{n_{tot}}{t_c} \qquad \text{(Equation 5-3)}$$

where t_c [a] is the corrosion time (time needed for complete corrosion of steel):

$$t_c = \frac{d}{2R} \qquad \text{(Equation 5-4)}$$

d average steel thickness [m]

R steel corrosion rate [m a^{-1}]

The corrosion rate is discussed in Section 4.3.2. In this report, a reference value of 1 μm a^{-1} is used and the impact of a so-called 'pessimistic' rate of gas production (equivalent to a 2 μm a^{-1} corrosion rate) is examined. In the framework of sensitivity analysis, rates of up to 5–10 μm a^{-1} are also considered. These rates are well outside the range of uncertainty in the corrosion rate, but are considered to test the robustness of the system with respect to the gas produced.

Table 5-2. Steel components and masses used in the different design options.

Steel component	Average steel thickness [mm]	Steel mass per canister [kg]		
		Option 1	Option 2a	Option 2b
Supercontainer	8	869	869	869
Feet beneath supercontainer	6 (8.5)	37.5	37.5	37.5
Feet beneath distance blocks	6 (8.5)	37.5	–	–
Ring bolted to rock	10	–	550 (1,500)	550 (1,500)
Ring attached to supercontainer	10	–	100	–
Total mass	–	944	1,557	1,457

5.2.3 Estimated gas generation rates

The total amount of gas generated per canister and the contributions of the various steel components for the three different design options are summarised in Table 5-3.

The estimated gas generation rates are given in Figure 5-1 for the three different design options and for a steel corrosion rate of 1 μm a^{-1}. Clearly, the largest contribution to the gas generation rate stems from the supercontainer. After 4,000 years, the corrosion and the gas production ceases. In design options 2a and 2b, major contributions are due to the ring bolted to the rock, the corrosion time of which is estimated to be about 5,000 years. The feet of the supercontainer and distance block add only marginally to the overall gas production rates.

In Figure 5-2 and Table 5-4, the total gas generation rates per canister are given for the three different design options as a function of the steel corrosion rates, namely 1 μm a^{-1} (base case), 2 μm a^{-1} (pessimistic variant) and 10 μm a^{-1} (hypothetical value for sensitivity analysis). The total gas production rates are proportional to the steel corrosion rates, whereas the duration of the gas production (corrosion time) is inversely proportional to the steel corrosion rate. Independently of the corrosion rate, the total gas production rate is highest for design options 2a/2b due to the additional steel rings used to fix the distance blocks. The estimated gas production rates are about half as high in design option 1 (Table 5-4).

There is the possibility that some hydrogen is consumed by microbially-mediated reduction of carbonate to acetic acid or methane by microbial activity /Rasilainen 2004/. This would lead to a reduction in the total amount of hydrogen in the repository system, but this process is conservatively neglected in the calculations.

Table 5-3. Total amounts of generated gas per canister for the three design options.

Steel component	Total amount of generated gas per canister [mol]		
	Option 1	Option 2a	Option 2b
Supercontainer	2.07×10^4	2.07×10^4	2.07×10^4
Feet beneath supercontainer	8.95×10^2	8.95×10^2	8.95×10^2
Feet beneath distance blocks	8.95×10^2	–	–
Ring bolted to rock	–	1.31×10^4 (3.58×10^4)	1.31×10^4 (3.58×10^4)
Ring attached to supercontainer	–	2.39×10^3	–
Total mass	2.25×10^4	3.72×10^4 (5.98×10^4)	3.48×10^4 (5.75×10^4)

Table 5-4. Maximal total gas production rates per canister for the three design options as a function of the steel corrosion rate.

Steel corrosion rate [μm a^{-1}]	Option 1 [mol a^{-1}]	[m^3 STP a^{-1}]	Option 2a [mol a^{-1}]	[m^3 STP a^{-1}]	Option 2b [mol a^{-1}]	[m^3 STP a^{-1}]
1	5.8	0.15	8.6	0.22	8.1	0.2
2	11.6	0.29	17.2	0.43	16.2	0.4
10	58	1.5	86	2.2	81	2

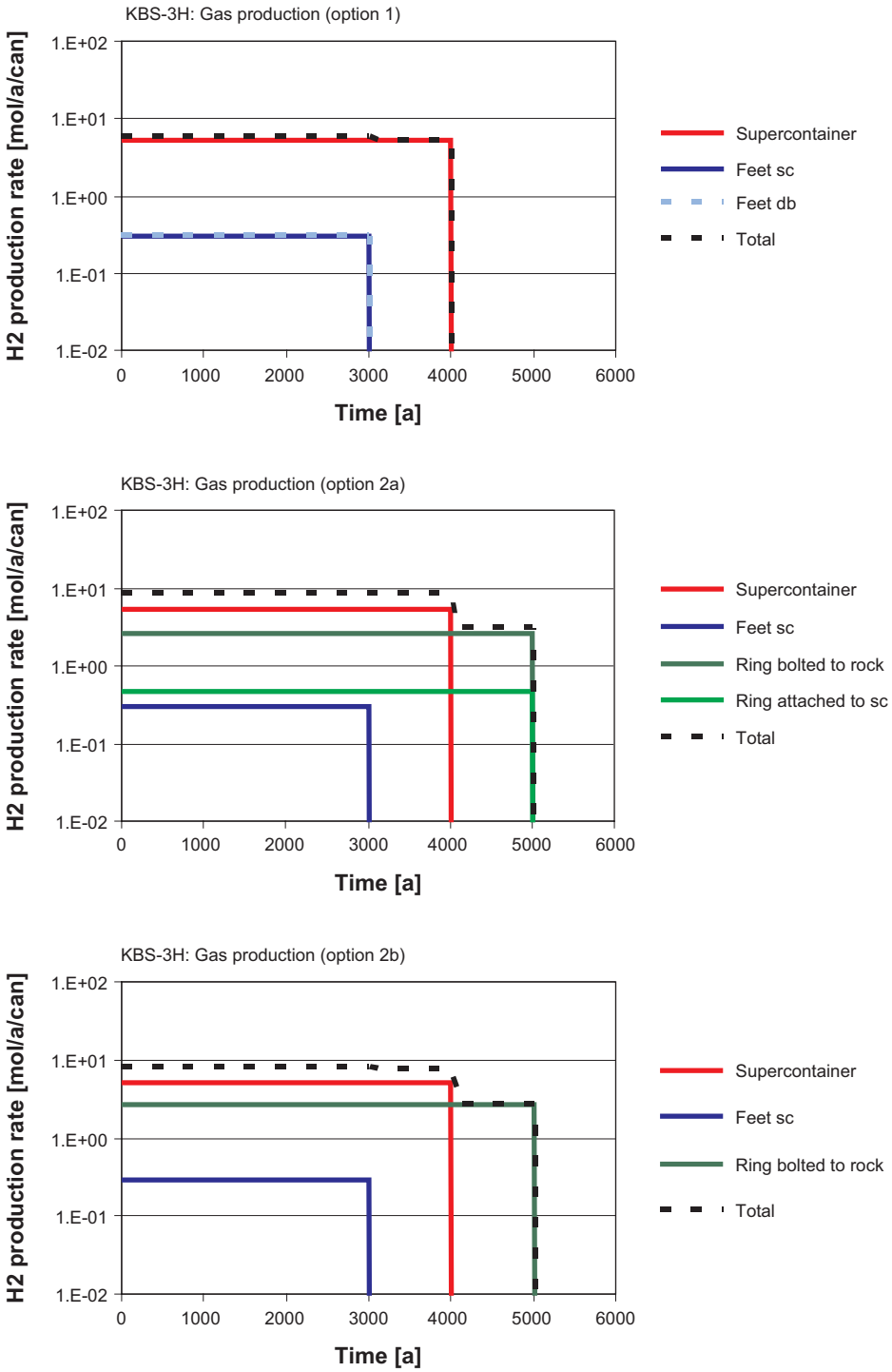

Figure 5-1. *H_2 gas generation rates for the different design options (steel corrosion rate 1 µm a^{-1}).*

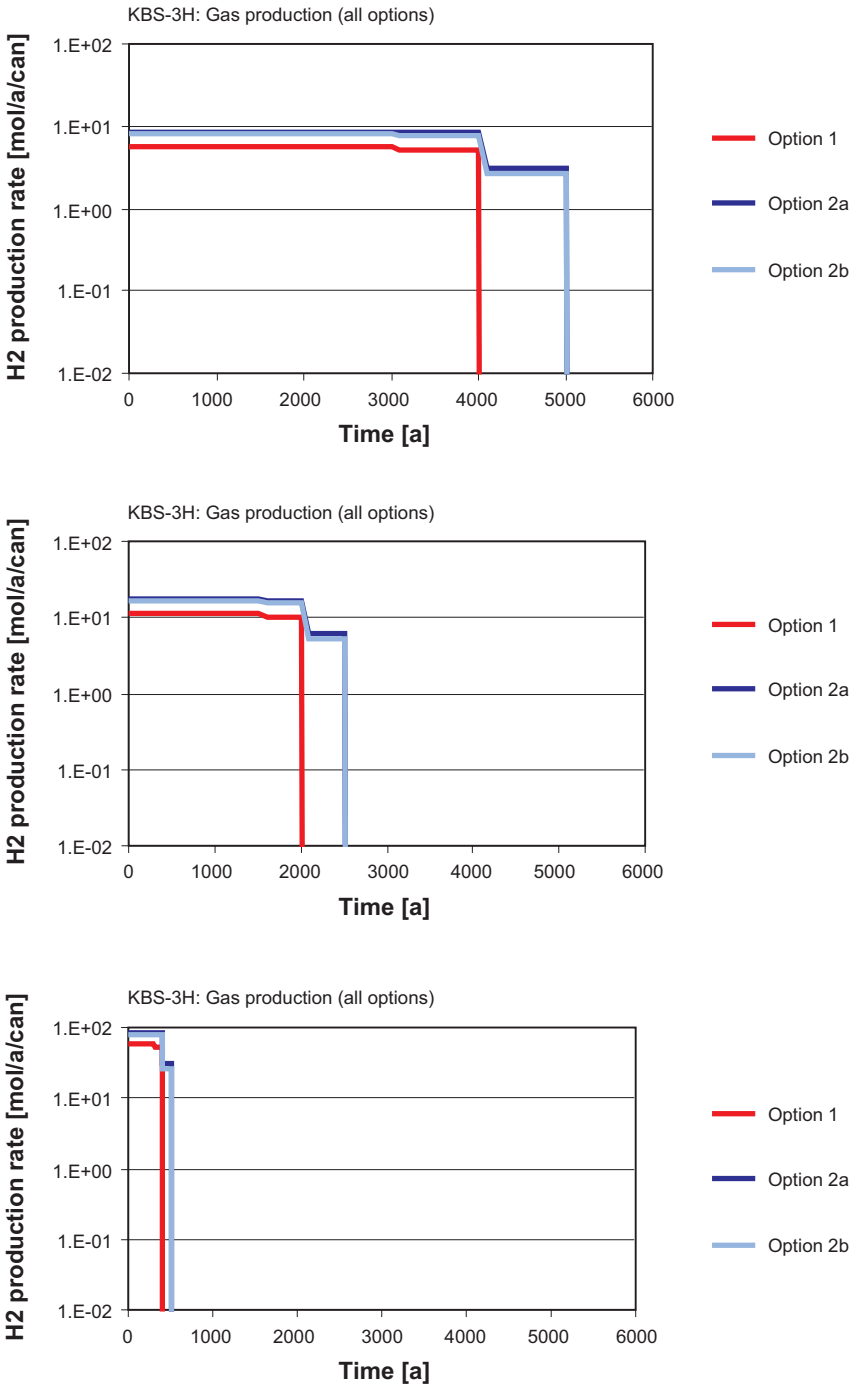

Figure 5-2. *H_2 gas generation rates for the different design options: steel corrosion rate of 1 µm a^{-1} (top figure), 2 µm a^{-1} (middle figure) and 10 µm a^{-1} (bottom figure).*

5.3 Gas pressure build-up

5.3.1 Objectives and scope

The objective of this chapter is to develop a model and perform simplified calculations for the pressure evolution and gas migration in the potential SF repository at the Olkiluoto site. The pressure build-up caused by gas generation in the repository is mitigated by gas dissolution, gas diffusion[3], gas-induced porewater displacement (incl. gas advection[4]) and capillary leakage[5] from the deposition drifts into the host rock (fractures, matrix) or along the EDZ. Gas transported through the fractures in the background host rock will eventually reach higher-permeability geological features, from which gas release takes place into the surface environment (see Figure 5-3). These processes are discussed in more detail in the following sections.

Gas dissolution takes place in various parts of the system (see Table 5-5), but is not shown in the figure.

5.3.2 Motivation for gas pressure build-up calculations

In this section, the need for performing model calculations on gas pressure build-up and gas migration is demonstrated by comparing the total amount of generated gas, n_{tot} [mol] (Table 5-3), with the overall capacity for storing and dissolving gas in the repository system. The objective of this analysis is to show that even for significantly overestimated gas storage and dissolution capacities the generated gas cannot be stored/dissolved in the repository system. In this sense, the upper bound of the amounts of gas that can be dissolved, $n_{diss,I}$ [mol], and stored, $n_{stor,I}$ [mol], in the various parts of the repository system is estimated by:

$$n_{diss,i} = V_i \frac{C(P_0)}{P_0} P_i \qquad \text{(Equation 5-5a)}$$

$$n_{stor,i} = \frac{V_i^* P_i}{R T_0} \qquad \text{(Equation 5-5b)}$$

where

V_i saturated pore volume available for dissolution of gas in repository part i [m^3 can^{-1}]

V^*_i gas accessible pore volume available for storage of gas in repository part i [m^3 can^{-1}]

$C(P_0)$ gas solubility at ambient pressure P_0 [mol m^{-3}]

P_i average pressure in in repository part i [Pa]

R universal gas constant [J K^{-1} mol^{-1}]

T_0 ambient temperature [K]

The volumes available for dissolution and storage of gas and the corresponding estimated capacities are summarised in Table 5-5. These calculations are based on emplacement of BWR spent fuel canisters (Posiva) and do not depend on a particular design option for the distance blocks. The parameter values are taken from Appendix A (Table A-1). For the bentonite outside the shell of the supercontainer (thickness 4 cm) and for the EDZ, it is hypthetically assumed that the entire pore space is available for gas storage, i.e. all porewater would be displaced from these domains by the generated gas. This is considered to set an upper bound to the storage capacity around the supercontainer. For the remaining bentonite including the distance block,

[3] *Gas diffusion* is an abbreviation for diffusive transport of dissolved gas in the aqueous phase.

[4] *Gas advection* is an abbreviation for advective transport of dissolved gas in the aqueous phase.

[5] C*apillary leakage* is an abbreviation for advective transport of gas in the gas phase under two-phase conditions (no structural changes in pore space involved).

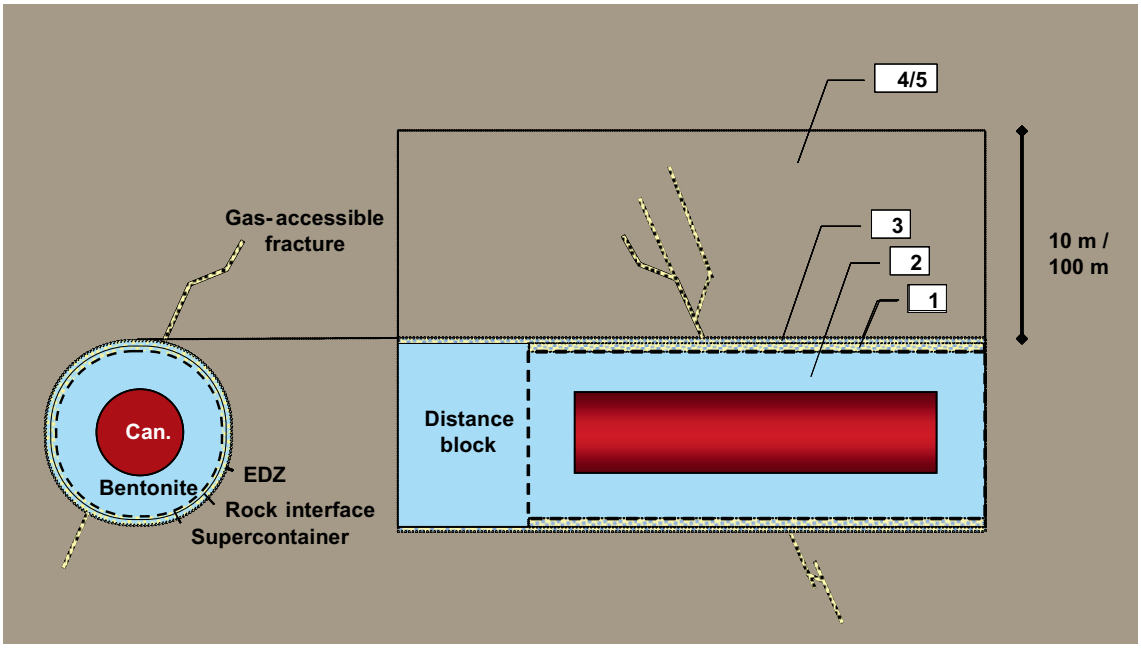

Figure 5-3. *Sketch of the various repository domains (i = 1–5) considered in the estimation of the capacities for gas dissolution and gas storage.*

it is likely that the gas saturation is very low, because of the fine bentonite pore structure and the corresponding high gas entry pressure. Therefore, all pore space is assumed to be available for gas dissolution only. In the host rock, it is assumed that gas can readily be stored in fractures, whereas the matrix pore space is accessible for gas only in dissolved form. The storage volume in fractures is calculated based on a total fracture intensity of P_{32} = 2 m^{-1} (Table 5-6) and on a mean hydraulic aperture of 2 µm. Note that using the mean hydraulic aperture (derived from the cubic law) instead of the mean arithmetic aperture leads to an underestimation of the gas storage volume in fractures. Table 5-5 shows that the largest contribution to gas storage is from the bentonite outside the shell of the supercontainer, whereas the porosity in the remaining bentonite and in the host rock matrix provide significant dissolution capacities.

Table 5-5. Estimated capacities for gas dissolution and gas storage in the various repository domains. The calculations are based on Posiva BWR spent fuel; the parameter values are taken from Table A-1 and the symbols are explained in Section 5.3.4.

Repository domain		Volume for gas dissolution V_i [m^3 can^{-1}]		Volume for gas storage V'_i [m^3 can^{-1}]		Amount of dissolved gas [mol can^{-1}]	Amount of stored gas [mol can^{-1}]
i		Formula		Formula			
1	4 cm of bentonite outside container shell	–	0	$\pi(r_t^2-(r_t-\Delta r_t)^2)\varepsilon_b l_{sc}$	0.56	0	880
2	Remaining bentonite (incl. distance block)	$\pi(r_t^2 p_c - r_c^2 l_c)\varepsilon_b - V_1^*$ (where $V_1^* = V_{i=1}^*$)	10.5	–	0	320	0
3	EDZ	–	0	$\pi(r_{EDZ}^2 - r_t^2)p_c\varepsilon_{EDZ}$	0.005	0	8
4	10 m of host rock	$p_c dh\varepsilon_m$	3.8	$p_c dhP_{32}a$	0.011	120	17
5	100 m of host rock	$p_c dh\varepsilon_m$	38	$p_c dhP_{32}a$	0.11	1,000	150

In Figure 5-4, these estimated capacities for gas dissolution and gas storage are compared with the total amount of generated gas in the repository (Table 5-3). Clearly, neither gas dissolution nor gas storage (nor the sum of the two) is sufficient to accommodate all generated gases in the repository. In fact, the total amounts of generated gases are more than one order of magnitude higher than the (upper bounds of the) capability of the repository system to dissolve and store gases. For this reason, more detailed calculations are needed to show that the generated gases are sufficiently mobile so that excessively high gas pressures in the repository system can be avoided (see Section 5.3.3).

5.3.3 Conceptual model

In the following, the relevant processes governing the pressure evolution and gas migration in the repository for spent fuel at Olkiluoto are summarised and the conceptual assumptions discussed (Figure 5-5).

Saturation of drifts

While gas pressure in the repository is below the formation pore pressure of 4 MPa, slow inflow of water from the host rock occurs and water saturation in the deposition drifts increases. Air in the void space between the supercontainer and rock as well as between the distance block and rock will be trapped. Full saturation is, however, not likely to be reached before the start of gas generation and a residual free gas phase will remain.

Gas generation

As discussed in Section 5.2.1, gas generation is caused by anaerobic corrosion of supercontainers and structural materials. The gas generation rate is determined by the steel corrosion rate, for which different values are considered: 1 μm a^{-1} (base case), 2 μm a^{-1} (pessimistic variant) and 10 μm a^{-1} (hypothetical value for sensitivity analysis). There is the possibility that some hydrogen is consumed by microbially-mediated reduction of carbonate to acetic acid or methane by microbial activity /Rasilainen 2004/. This would lead to a reduction in the total amount of hydrogen in the repository system, but this process is conservatively neglected in the calculations.

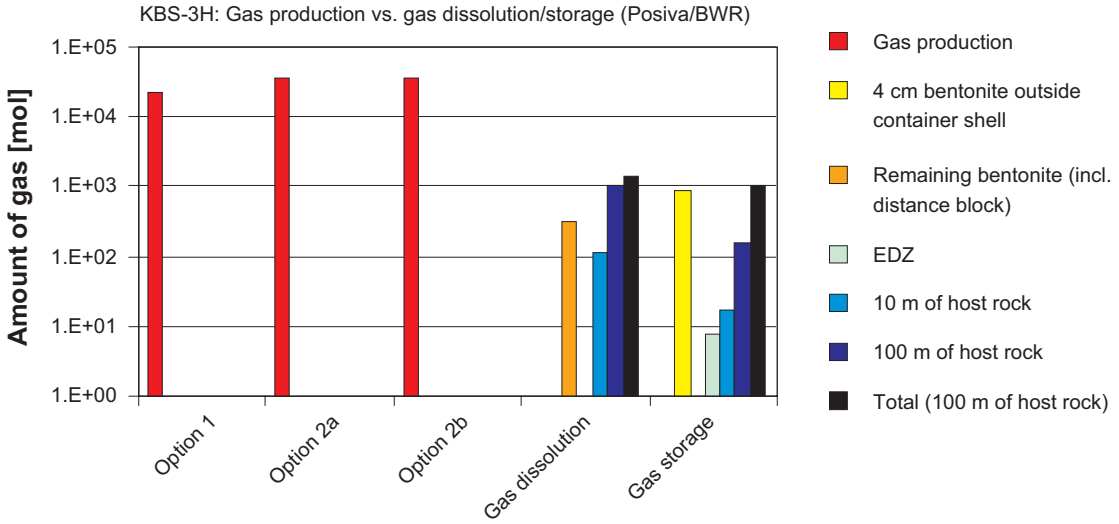

Figure 5-4. *Estimated capacitiy for gas storage and gas dissolution in comparison with the total amount of generated gas in the repository.*

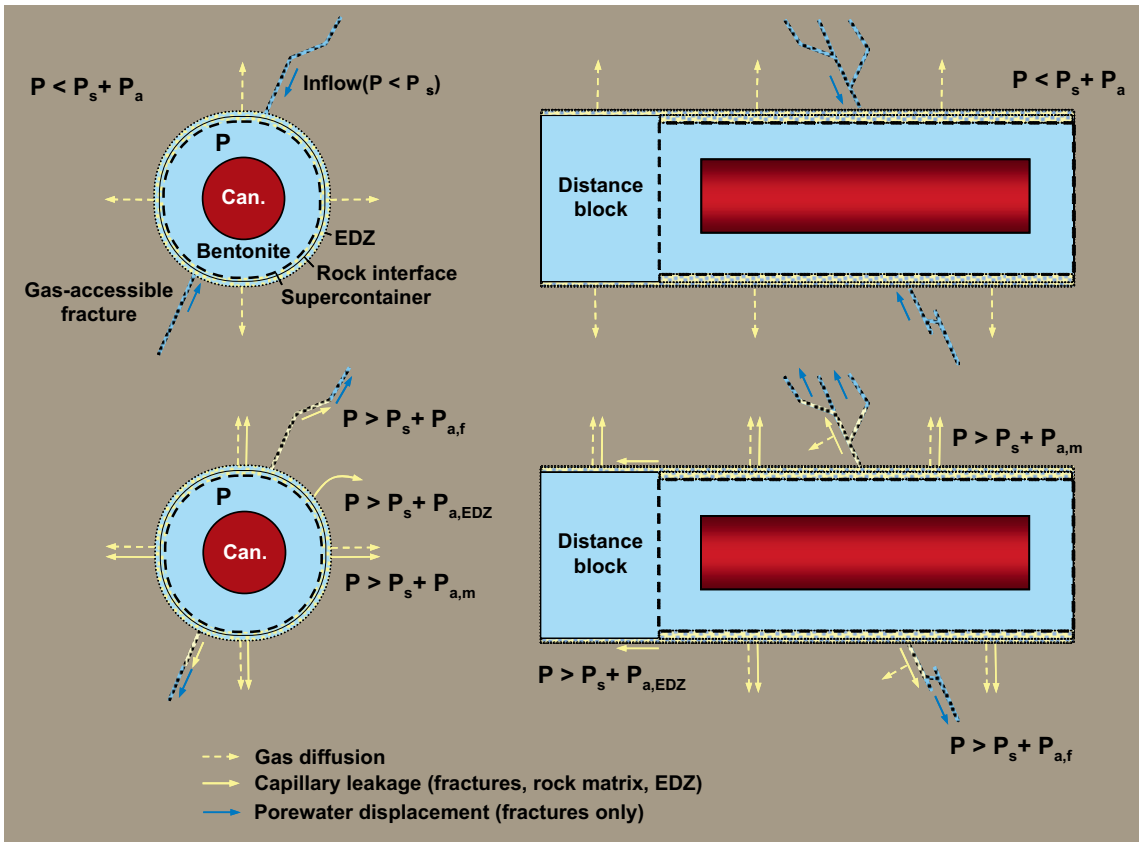

Figure 5-5. *Conceptual model for gas transport in the repository system for spent fuel at the Olkiluoto site.*

Gas dissolution and diffusion

Hydrogen gas generated by anaerobic steel corrosion, as well as gas entrapped at the time of closure, will dissolve in the near field pore water until the solubility limit at repository pressure is reached. Dissolved gas diffuses through the drift walls into the host rock. The natural hydrogen concentration is far from its solubility limit under repository conditions /Rasilainen 2004/ and is not taken into account in the model calculations. Although the natural methane concentration is relatively close to its solubility limitation, it is not taken into account, because there is no significant interaction with hydrogen gas.

Gas dissolution takes place in various parts of the system (see Table 5-5), but is not shown in the figure.

Pressure build-up and porewater displacement in the near field

The pressure of the free gas phase increases as a result of the ongoing generation of gas. In the near field, the pressure increases until gas pathways from the steel surfaces through the bentonite are created. This results in gas-induced displacement of porewater and advection of dissolved gas, although there is evidence that there is little water expulsion from dense saturated bentonite /Harrington and Horseman 2003/. Gas storage volumes are created, mainly within bentonite in the vicinity of the steel surfaces, but also in the EDZ. If the gas generation rate exceeds the rate of gas removal (by dissolution/diffusion) and gas volume increase (porewater displacement), then the gas pressure further rises until capillary leakage into the host rock or along the EDZ occurs (see next two headings).

Capillary leakage and porewater displacement (incl. advection of dissolved gas) into host rock

When the gas pressure exceeds the threshold for capillary leakage (formation pore pressure of 4 MPa plus gas entry pressure of up to a few MPa depending on the fracture transmissivity), leakage of gas into existing fractures takes place. This involves porewater displacement (moving gas front) and advection of dissolved gas within the fractures as well as diffusion of dissolved gas from the fractures into the rock matrix. The latter process quickly leads to partial saturation of the rock matrix with dissolved hydrogen gas. At higher pressures (gas entry pressure of up to 10 MPa depending on the permeability of the matrix), gas leakage also takes place into the host rock matrix. Gas leakage is assumed to be proportional to the product of the fracture transmissivity (case of fractures) or gas permeability (case of matrix) times the hydraulic gradient (Darcy's law).

Formation of gas pathways along the deposition drift

Pressure may further increase until the threshold pressure for the formation of gas pathways through or around the distance blocks (EDZ) is reached (gas piping). This is likely to occur from drift sections with extremely tight rock to the next drift sections where fractures of sufficient transmissivity and connectivity are present, thus allowing gas to migrate through the host rock. In the model calculations, gas leakage is assumed to occur within the fracture network of the EDZ, as soon as the gas pressure exceeds the formation pore pressure (4 MPa) plus the gas entry pressure within the EDZ. Gas migration along the deposition drift may be hindered or completely stopped by swelling of distance blocks. This situation is addressed by considering a separate calculational case with an impermeable EDZ. Bentonite erosion by gas piping in the post-operational phase is not likely to have any significant effect on system performance and is not considered in the model calculations.

Long distance gas escape along the axis of the deposition drift to the access tunnel system, where significant pore volumes are provided for additional gas storage, has pessimistically been neglected in the model calculations.

Gas breakthrough to major geological features of enhanced transmissivity

Gas transported through the host rock will eventually reach major geological features with enhanced transmissivity, through which gas will migrate to the surface. After breakthrough, the gas pressure in the deposition drifts will slowly decrease. Gas breakthrough is taken into account in the model calculations by assuming a maximum travel distance for the moving gas front in fractures, whereas gas breakthrough from the matrix is not accounted for (long-distance transport through the matrix is unlikely to occur). The detailed transport processes after breakthrough are not modelled explicitly, because they have no influence on the maximal pressure in the system.

The possibility of reactivation of fractures in the near-field rock as a consequence of gas pressure buildup is discussed in Section 6.2.2.

5.3.4 Mathematical representation

5.3.4.1 Mass balance for gas

The following mathematical model is a simplified representation of the processes described in Section 5.3.3 and shown in Figure 5-5. It is based on a mass balance consideration for the gas generated within the repository. All input parameters, with the exception of the gas generation rates, are assumed to be constant in time. In particular, the lengths over which the gas-induced hydraulic gradient and the concentration gradient for dissolved gas in the host rock are non-zero are assumed to be time-independent. Furthermore, gas leakage in the representative pathway is assumed to occur when the gas entry pressure is exceeded and is modelled in terms of a moving gas front at a velocity determined by the hydraulic transmissivity in a representative pathway (Figure 5-6). The fracture network in the host rock is represented by a single representative pathway, characterised by its transmissivity, trace length and degree of connectivity. The

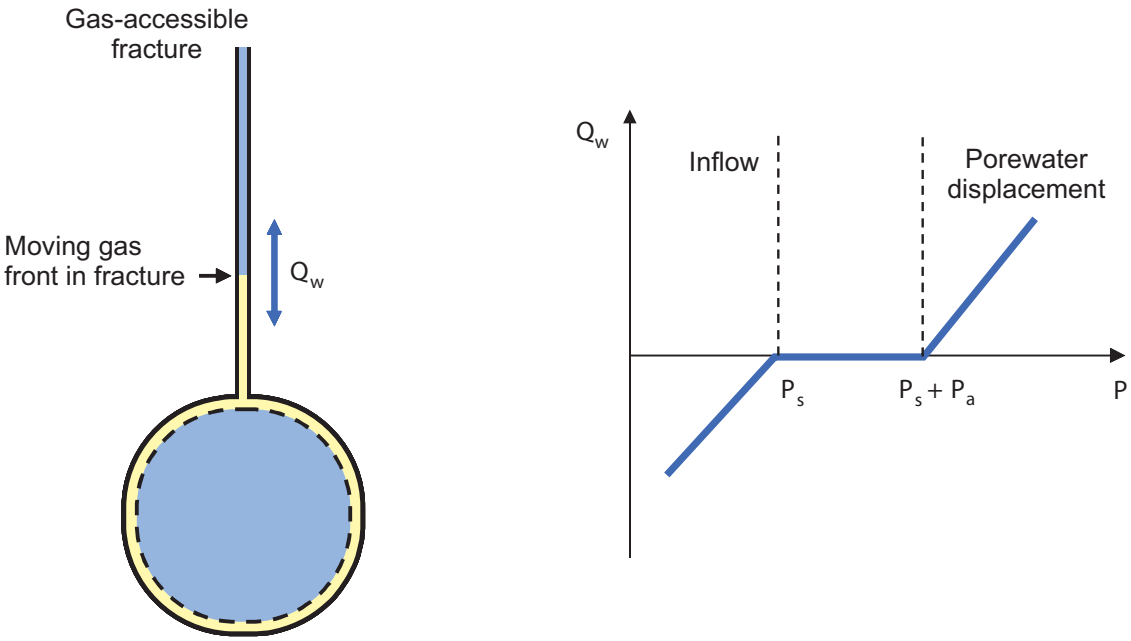

Figure 5-6. *Simplified model for gas-induced water displacement from deposition drift into gas-accessible fracture (gas leakage) and vice-versa (saturation of drift).*

hydraulic aperture and the gas entry pressure of the representative pathway are derived from its transmissivity (see Section 5.3.4.2). The pressure in the gas phase is assumed to be everywhere the same, i.e. the pressure drop within the gas-filled pore space (e.g. within fractures in the host rock) is not considered.

The gas pressure is governed by

$$P(t) = n(t)\frac{RT_0}{V_g(t)} \qquad \text{(Equation 5-6)}$$

where the volume available for gas storage, V_g, is equal to the initial volume within the deposition drift plus any volume change created by water displacement (see Figure 5-6):

$$V_g(t) = \min(V_{g,\max}; V_g + \int_0^t Q_w(t')dt')$$

$$\dot{V}_g(t) = Q_w(t) = \frac{TG}{\rho\, g}\frac{\Delta P(t)}{l_h} = \gamma\, \Delta P(t)$$

$$\Delta P(t) = \begin{cases} P(t) - P_s & P \le P_s \\ 0 & P_s < P \le P_s + P_a \\ P(t) - P_s - P_a & P > P_s + P_a \end{cases} \qquad \text{(Equation 5-7)}$$

$$V_g(0) = V_g$$

Symbols:

$P(t)$ gas pressure in drift at time t [Pa]

P_s formation pore pressure in host rock at repository depth [Pa]

P_a gas entry pressure of fracture [Pa]

$n(t)$ amount of gas in drift per canister [mol can^{-1}]

R universal gas constant [J K^{-1} mol^{-1}]

T_0 ambient temperature [K]

$V_g(t)$ volume available for gas storage per canister [m^3 can^{-1}]

$V_{g,max}$ maximal volume available for gas storage per canister [m^3 can^{-1}]

$Q_w(t)$ water flow rate in fractures [m^3 a^{-1} can^{-1}]

T hydraulic transmissivity of the representative pathway [m^2 s^{-1}]

G trace length of the representative pathway [m]

l_h distance over which hydraulic gradient due to gas generation is non-zero [m]

ρ density of water [kg m^{-3}]

g gravitational acceleration [m s^{-2}]

Note that all extensive quantities correspond to a section of the deposition drift containing a single canister, its supercontainer and one distance block. The initial residual volume available for storage of gas is assumed to be equal to the pore volume of an annulus of bentonite of thickness 4 cm outside the supercontainer shell plus the pore volume in the EDZ (see Equation 5-12). Note that the maximal volume available for gas storage, $V_{g,max}$, is reached when gas breakthrough to some major geological feature with enhanced transmissivity occurs. The breakthrough criterion is met when the vertical position of the moving gas front, $z(t)$, has reached the vertical position of the enhanced transmissivity feature (z_{max}):

$$z(t) = \frac{V_g(t) - V_g}{A\varepsilon_g} = z_{\max} \qquad \text{(Equation 5-8)}$$

A repository area per canister (= pitch × drift separation = $p_c\, d$) [m^2 can^{-1}]

ε_g gas accessible porosity in host rock [–]

The gas accessible porosity in the host rock is assumed to correspond to the cumulated fracture volume per volume of bulk host rock (see Section 5.3.4.2). The contribution of the matrix porosity is pessimistically neglected, because it is accessible to gas only under extreme conditions (excessively high gas pressures).

The mass balance for gas contained in the free gas phase is expressed as (all quantities correspond to a single canister section):

$$\dot{n} = \dot{n}_p - \dot{n}_{sol} - \dot{n}_{diff} - \dot{n}_{leak,m} - \dot{n}_{leak,EDS} \qquad \text{(Equation 5-9)}$$

where

$\dot{n}$ rate of change of gas contained in free gas phase [mol a^{-1}]

$\dot{n}_p$ gas generation rate [mol a^{-1}]

$\dot{n}_{sol}$ gas dissolution rate in near field and far field porewater [mol a^{-1}]

$\dot{n}_{diff}$ gas diffusion rate from drift walls radially into the rock matrix [mol a^{-1}]

$\dot{n}_{leak,EDS}$ gas leakage rate to neighboring canister section through EDZ [mol a^{-1}]

$\dot{n}_{leak,m}$ gas leakage rate from drift walls radially into the rock matrix [mol a^{-1}]

Note that in this chapter, the time derivative of a quantity n is denoted by a dot ($\dot{n}$). In Equation 5-9, loss terms due to gas migration along the drift system are assumed to take place only from one canister section to the neighboring canister section. Long-distance gas transport through the drifts is pessimistically not taken into account, i.e. the sealing zones at the ends of deposition drifts are assumed to be impermeable. Gas advected in the displaced porewater within the fracture is absent in Equation 5-9 because it does not, strictly speaking, provide a loss term for the amount of gas contained in the free gas phase. The loss terms in Equation 5-9 are calculated in a simplified fashion as follows:

$$\dot{n}_{sol} = \frac{\partial}{\partial t}\left(\frac{C(P_0)}{P_0} V_{sol}\ P \right) = \frac{C(P_0)}{P_0}\left(V_{sol}\ \dot{P} + \dot{V}_{sol}\ P \right)$$

$$\dot{n}_{diff} = 2\pi\, r_{EDZ}\, p_c \varepsilon_m D_p \frac{C(P_0)}{P_0}\frac{P}{l_d} = \delta\ P \qquad \text{(Equation 5-10)}$$

$$\dot{n}_{leak,m} = 2\pi\, r_{EDZ}\, p_c \frac{k_{g,m}}{\mu_g RT_0}\frac{P^2 - (P_s + P_{a,m})^2}{2l_h} = \frac{\alpha}{RT_0}\left[P^2 - (P_s + P_{a,m})^2 \right]$$

$$\dot{n}_{leak,EDZ} = \pi\,(r_{EDZ}^2 - r_t^2)\frac{k_{g,EDZ}}{\mu_g RT_0}\frac{P^2 - (P_s + P_{a,EDZ})^2}{2p_c} = \frac{\beta}{RT_0}\left[P^2 - (P_s + P_{a,EDZ})^2 \right]$$

where

$$P_{a,m} = 0.56 \times k_{g,m}^{-0.346}$$

$$P_{a,EDZ} = \frac{4\sigma}{a_{EDZ}} \qquad \text{(Equation 5-11)}$$

P_0 standard pressure [Pa]

$C(P_0)$ solubility of hydrogen gas in water [mol m^{-3}]

r_{EDZ} radius of EDZ [m]

p_c canister pitch (center-to-center distance) [m]

ε_m porosity of rock matrix [–]

D_p pore diffusion constant in rock matrix [m^2 s^{-1}]

$k_{g,m}$ gas permeability of rock matrix [m^2]

$k_{g,EDZ}$ gas permeability of EDZ [m^2]

$P_{a,m}$ gas entry pressure of rock matrix [Pa]

$P_{a,EDZ}$ gas entry pressure of EDZ [Pa]

σ surface tension gas/water (ca. 0.073 N m^{-1} at 20°C), [N m^{-1}]

a_{EDZ} average fracture aperture of the EDZ [m]

μ_g dynamic viscosity of hydrogen gas [Pa s]

l_h distance over which hydraulic gradient due to gas generation is non-zero [m]

l_d distance over which concentration gradient of dissolved gas is non-zero [m]

Note that the gas entry pressure of the rock matrix in Equation (5-11) is calculated from the intrinsic permeability using Davies relationship /Nagra 2004/, whereas the gas entry pressure of the EDZ is derived from the fracture apertures in the crushed zone of the EDZ using Young's equation. According to Appendix D, the largest observed fractures in the EDZ have apertures over 10 µm. These features do not form a continuous network, but are connected by fractures with apertures smaller than 5 µm. In the simplified gas model calculations, the gas entry pressure is calculated based on the average aperture (2 µm). Significant uncertainty remains, however, on the effect of heterogeneity on the gas transport capacity within the EDZ.

The gas permeability of the rock matrix is assumed to be 1% of the intrinsic permeability, to take into account that only the largest matrix pores are readily accessible to gas. Similarly, for the EDZ the gas permeability is set to 10% of the intrinsic permeability, assuming that only the larger connected fractures are readily accessible to gas /Helmig 1997, Rodwell et al. 1999/. These assumed values are only very approximate and a detailed assessment based on characterisation (Appendix D) and measurements would be required in order to evaluate the uncertainties.

Smaller pores and fractures are in principle also accessible to gas, but at significantly higher entry pressures.

By analogy with the formula given in Table 5-5, the volumes available for gas storage and for dissolution are calculated as follows:

$$V_g(t) = \pi\left[(r_t^2 - (r_t - \Delta r_t)^2)\varepsilon_b l_{sc} + (r_{EDZ}^2 - r_t^2)p_c\varepsilon_{EDZ}\right] + p_c d\varepsilon_g z(t)$$
$$V_{sol}(t) = \pi\left[(r_t^2 p_c - r_c^2 l_c)\varepsilon_b - (r_t^2 - (r_t - \Delta r_t)^2)\varepsilon_b l_{sc}\right] f_{sol} + p_c d\varepsilon_m f_{sol,m} z(t) \quad \text{(Equation 5-12)}$$

where

r_t radius of deposition drift [m]

Δr_t thickness of bentonite annulus (4 cm of bentonite outside the supercontainer shell) available for gas storage [m]

d separation between deposition drifts [m]

r_c radius of canister [m]

l_c length of canister [m]

l_{sc} length of supercontainer [m]

f_{sol} volume fraction available for gas dissolution in deposition drift [–]

$f_{sol,m}$ volume fraction available for gas dissolution in rock matrix [–]

ε_b porosity of bentonite [–]

ε_{EDZ} porosity of EDZ [–]

ε_g gas accessible porosity of rock matrix [–]

Combining Equations 5-6 to 5-12, the differential equation for the gas pressure $P(t)$ reads:

$$\dot{P} = \frac{(\dot{n}_p - \delta P)RT_0 - \gamma(1 + \frac{C(P_0)}{P_0}RT_0\frac{\varepsilon_m}{\varepsilon_g}f_{sol,m})P\Delta P - \alpha(P^2 - (P_s + P_{a,m})^2) - \beta(P^2 - (P_s + P_{a,EDZ})^2)}{V_g + \gamma\int_0^t \Delta P(t')dt' + V_{sol}\frac{C(P_0)}{P_0}RT_0} \quad \text{(Equation 5-13)}$$

where

$$\alpha = \pi r_{EDZ} p_c \frac{k_{g,m}}{\mu_g l_h}; \quad \beta = \pi(r_{EDZ}^2 - r_t^2)\frac{k_{g,EDZ}}{2\mu_g p_c}$$
$$\gamma = \frac{TG}{\rho\, g\, l_h}; \quad \delta = 2\pi r_{EDZ} p_c \varepsilon_m D_p \frac{C(P_0)}{P_0 l_d}$$

Equation (5-13) is integrated numerically using a backward time-stepping procedure.
The steady-state gas pressure is obtained by setting $\dot{P} = 0$, $P > P_s + P_a$, $P > P_s + P_{a,EDZ}$ and $\dot{n}_p = \dot{n}_{p,\max} = \max[\dot{n}_p(t)]$. This steady-state gas pressure corresponds to the asymptotic maximal gas pressure in the deposition drift. The analytical expression is:

$$P_{\max} = \frac{\theta(P_s + P_a) - \delta + \sqrt{(\theta(P_s + P_a) - \delta)^2 + 4(\theta + \frac{\beta}{RT_0})(\frac{\beta}{RT_0}(P_s + P_{a,EDZ})^2 + \dot{n}_{p,\max})}}{2(\theta + \frac{\beta}{RT_0})} \quad \text{(Equation 5-14)}$$

where

$$\theta = \frac{\gamma}{RT_0}\left(1 + \frac{C(P_0)}{P_0} RT_0 \frac{\varepsilon_m}{\varepsilon_g} f_{sol,m}\right)$$

Note that gas leakage into the rock matrix is neglected in Equation (5-14), because it takes place under excessively high pressures only. P_{max} depends on the hydraulic transmissivity of the representative pathway via the parameter γ and is used in Section 5.3.4.2 to calculate the expectation value of the maximal gas pressure using the probability density function for the hydraulic transmissivity in the fracture network.

5.3.4.2 Representation of fracture network

In the model calculations, for each canister section the fracture network in the host rock is represented by a single representative pathway. Qualitatively, the representative pathway represents those fracture(s) per canister section that will provide the dominant gas migration pathway. Because the migration of gas generally takes place within the largest pores (lowest gas entry pressures), the representative pathway corresponds to the fracture(s) with the highest hydraulic transmissivities.

As pointed out in Appendix A in /Poteri and Laitinen 1999/, it is sufficient to assume that the total transmissivity of v fractures equals that of the fracture with the highest transmissivity, if the number of fractures is small and the variance of the transmissivity distribution is large. In the case of the Olkiluoto site, the observed density of potentially water-conducting fractures along boreholes below the depth of 200 m is 1–3 m^{-1} (see Table 6-7 in /Poteri and Laitinen 1999/), which results in about 10–30 fractures per canister section, the latter having a length of roughly 10 m. Assuming a log-normal transmissivity distribution, the logarithmic standard deviation of the modelled transmissivity distribution was set to 2.5 in /Poteri and Laitinen 1999/, although it is noted that this value is quite low when compared with the variance in the transmissivity measurements for the Olkiluoto site. In other words, the 95% confidence interval for the fracture transmissivity extends over roughly ten orders of magnitudes (= mean ± two standard deviations). For this reason, the assumption that the representative pathway corresponds to the fracture with the highest hydraulic transmissivity within each canister section is considered to be well justified.

The representative pathway is characterised by its transmissivity, trace length and degree of connectivity. The mean trace length is 2.3 m, showing a relatively narrow variability range of 2–3 m /Poteri 2001/. Given the hydraulic conductivity of the background rock of roughly 10^{-10} m s^{-1}, the degree of hydraulic connectivity is considered to be relatively high, i.e. the individual fractures constituting a flow path are hydraulically well connected /Poteri and Laitinen 1999/. There is, however, significant uncertainty in the degree of connectivity relevant for the migration of gas. In narrow sections of a flow path, the gas entry pressure may be considerably higher than in other sections and gas flow may be hindered or even stopped (bottlenecks), even though the same section may be hydraulically conductive. The connectivity relevant for gas migration could be tested by calculating the percolation threshold for gas migration using a fracture network model based on distributions of fracture transmissivity, trace length, orientation and aperture, along the lines of the DFN model presented by /Poteri and Laitinen 1999/, see Section 2.6. From the aperture distribution, the distribution of gas entry pressure can be calculated using Young's equation (see below). For the purpose of the present simplified model calculations, it is assumed that the fracture network is sufficiently connected, so that gas is able to percolate through the background rock. The validity of this assumption needs, however, further analysis. Such analyses would also provide more reliable information on the hydraulic transmissivity of gas pathways that are to be expected at the Olkiluoto site.

The hydraulic aperture and the gas entry pressure of the representative pathway are derived from its transmissivity (see below). In the framework of these simplified representations, the interaction between gas and water phases is represented by the gas entry pressure (capillary

threshold pressure) only. The detailed constitutive relationships between saturation and capillary pressure/relative permeability are not taken into account in the simplified gas model calculations. The relationship between hydraulic transmissivity and hydraulic aperture of the representative pathway is approximated by the 'cubic law' /De Marsily 1986/:

$$T = \frac{\rho\, g\, a^3}{12\mu} \qquad \text{(Equation 5-15)}$$

where

T hydraulic transmissivity of representative pathway [$m^2\ s^{-1}$]

a hydraulic aperture of representative pathway [m]

ρ density of water [$kg\ m^{-3}$]

g gravitational acceleration [$m\ s^{-2}$]

μ dynamic viscosity of water [Pa s]

The relationship between radius and gas entry pressure (capillary threshold pressure) of a capillary tube is approximated by Youngs's equation /De Marsily 1986/:

$$P_a = \frac{2\sigma}{r} \qquad \text{(Equation 5-16)}$$

where

P_a gas entry pressure (capillary threshold pressure) [Pa]

σ surface tension gas/water (ca. 0.073 N m^{-1} at 20°C), [N m^{-1}]

r pore radius of capillary tube (= a/2) [m]

A similar equation holds for flow between parallel plates when the radius r is substituted by the half aperture a/2.

The gas accessible porosity of the background rock corresponds to the volume of the most transmissive fracture and can be derived from its hydraulic aperture[6]:

$$\varepsilon_g = \frac{P_{32}}{v} a \qquad \text{(Equation 5-17)}$$

P_{32} fracture intensity of background rock (= total surface of fractures per unit volume of bulk rock) [m^{-1}]

v number of potentially water-conducting fractures per canister section (= 10–30) [–]

Because of the expected large heterogeneity of the host rock along a deposition drift, the hydraulic transmissivity of the representative pathway is varied over a broad parameter range, i.e. from 10^{-14} to 10^{-7} $m^2\ s^{-1}$ (see Section 5.3.5). According to /Poteri and Laitinen 1999/, Appendix A, the probability density function $f(T,\mu_T,\sigma_T,v)$ for the maximal transmissivity of v fractures, each being log-normally distributed with logarithmic mean μ_T and logarithmic standard deviation σ_T, can be calculated from:

$$f(T,\mu_T,\sigma_T,v) = \frac{2^{1/2-v}\, v}{\sqrt{\pi}\,\sigma_T T}\left[1 + erf\left(\frac{\ln T - \mu_T}{\sqrt{2}\sigma_T}\right)\right]^{v-1} \exp\left[\frac{(\ln T - \mu_T)^2}{2\sigma_T^2}\right] \qquad \text{(Equation 5-18)}$$

[6] Note that using the hydraulic aperture (derived from the cubic law) instead of the arithmetic aperture leads to an underestimation of the gas storage volume within the fracture.

In Figure 5-7, this probability density (PDF) function is compared to the (log-normal) PDF of a single fracture using two different standard deviations. From Equation (5-18), the expectation of the maximal gas pressure is calculated as follows:

$$\overline{P}_{\max} = \int_0^{\infty} P_{\max}(T) f(T, \mu_T, \sigma_T, v) dT \qquad \text{(Equation 5-19)}$$

Note that the mean μ_T and logarithmic standard deviation σ_T in Equation (5-18) are based on the natural logarithm. To derive these from the values based on $\log_{10}$ as given in /Poteri and Laitinen 1999/, the following expressions must be used:

$$\mu_T = \ln(10)\mu_{T,10}$$
$$\sigma_T = \ln(10)\sigma_{T,10} \qquad \text{(Equation 5-20)}$$

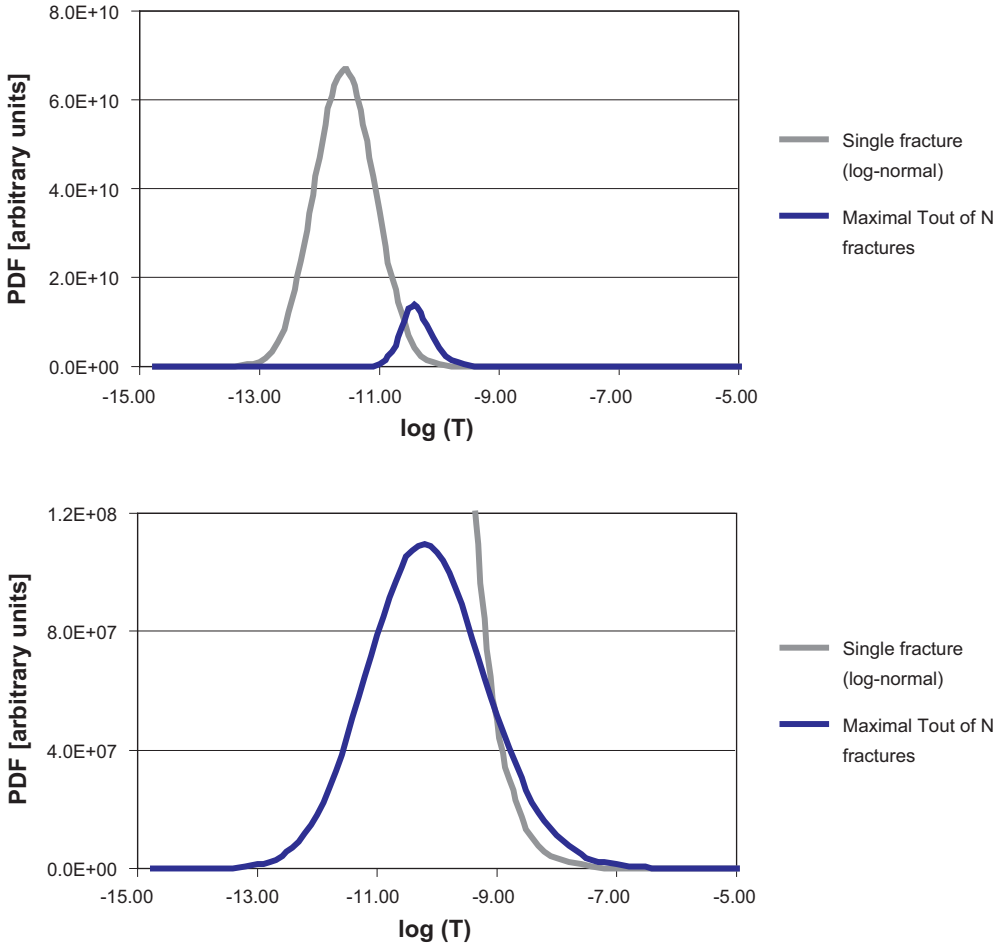

Figure 5-7. *Comparison of the probability density functions (PDF) for the maximal transmissivity of v fractures and for the single fracture (log-normal distribution). Two different standard deviations of log10 for the fracture transmissivity are used: 0.5 (upper figure, for system understanding only) and 2.5 (lower figure, reference value used by /Poteri and Laitinen 1999/. The number of potentially water-conducting fractures per canister section used in these figures is v = 10.*

5.3.5 Input parameters

A summary of input parameters is found in Appendix A (Table A-1). In this section, some additional parameters are listed (Tables 5-6 and 5-7). These parameters are not contained in Table A-1, either because they are

- general parameters to be found in any standard data collection,
- related to special conceptual assumptions in the gas model calculations (examples: hydraulic length l_h, diffusive length l_d),
- identified only in the course of performing the model calculations.

Table 5-6. Special parameter values for the gas analysis.

Parameter	Unit	Symbol	Reference value	Alternative values	Comment/Ref.
Average steel thickness					
Supporting feet	mm		6		Meeting 28.05.04
Ring bolted to rock	mm		10		
Ring attached to supercontainer	mm		10		
Available volume fraction for dissolution					
Bentonite	–	f_{sol}	1		Quickly saturated
Rock matrix	–	$f_{sol,m}$	0.01		See also Table 5-7
Gneiss average matrix properties					
Pore diffusion const.	$m^2\ s^{-1}$	D_p	4×10^{-11}		/SKB 1999c/, p. 126
Gas permeability	m^2	$k_{g,m}$	5×10^{-23}		1% of intrinsic permeability
Gneiss fracture properties					
Total fracture intensity	$m^2\ m^{-3}$	P_{32}	2		/Poteri and Laitinen 1999/, p. 63
Average trace length	m	G	2.3		/Poteri 2001/, p. 12
Number of potentially water-conducting fractures per canister section	m^{-1}	v	11		Derived from linear fracture density ($1\ m^{-1}$) and canister pitch
Fracture distribution type	–	–	log-normal		/Poteri and Laitinen 1999/, p. 64
log10-T mean	–	μ_T	–11		/Poteri and Laitinen 1999/, p. 70
log10-T std	–	σ_T	2.5		/Poteri and Laitinen 1999/, p. 70
Vertical distance to closest major geological feature with enhanced permeability	m	z_{max}	100	large (no gas break-through criterion applied)	
EDZ average properties					
Gas permeability	m^2	$k_{g,EDZ}$	3E–20	0	10% of intrinsic permeability

Parameter	Unit	Symbol	Reference value	Alternative values	Comment/Ref.
Special input parameters					
Hydraulic length (= distance over which hydraulic gradient is non-zero)	m	l_h	100		= z_{max} (vertical distance to closest major geological feature with enhanced permeability), see Table 5-7
Diffusive length (= distance over which hydrogen concentration in rock matrix is non-zero)	m	l_d	1		See Table 5-7
General input parameters					
Hydrodynamic viscosity water	Pa.s	μ	1E–3		
Hydrodynamic viscosity H_2	Pa.s	μg	1E–5		
Surface tension water/gas	N m^{-1}	σ	0.073		
Ambient temperature	K	T_0	303		

Table 5-7. Justification of chosen values for characteristic lengths of hydraulic gradient in fractures and concentration gradient of dissolved hydrogen in the rock matrix. T is the minimal hydraulic transmissivity (10^{-14} m^2 s^{-1}), a is the corresponding fracture aperture ($2 \cdot 10^{-7}$ m, calculated from cubic law), and S_s is the specific storativity (10^{-5} m^{-1}).

Time t [a]	$l_d = \sqrt{\pi D_p t}$ [m]	$l_h = \sqrt{\frac{T}{aS_s} t}$ [m]
	(hydrogen concentration gradient)	**(hydraulic gradient)**
10^2	0.6	> 1,000
10^3	2	> 1,000
10^4	6.0	> 1,000
Choice	**1**	**100** (= vertical distance to closest major geological feature with enhanced permeability)

5.3.6 Results

In this section, the results of the simplified model calculations are presented in a deterministic manner (by considering a range of fixed hydraulic transmissivities of representative pathways) and in a probabilistic manner using the PDF for the maximal fracture transmissivity as a weighting function.

For the deterministic results (Figures 5-8 to 5-13), the gas pressure is plotted against time for several different situations:

1) No gas transport and no gas dissolution (the generated gases are stored in the initial storage volume).
2) Gas dissolution in the deposition drift and EDZ and diffusion from the EDZ into the rock matrix.
3) As in 2) plus gas leakage by 2-phase flow from the EDZ into the rock matrix added

4) As in 3) plus gas leakage by 2-phase from one canister section through the EDZ around the distance block into the next canister section added (this case is relevant only for extremely tight canister sections, where gas is expected to migrate along the EDZ to a neighboring canister section providing sufficient gas migration capacity)

5) As in 4) plus gas leakage by 2-phase flow and porewater displacement in a representative pathway as a function of hydraulic transmissivity added.

Situations 1–4 should be viewed as hypothetical cases, that visualize the individual contributions of various gas storage and transport mechanisms. Note that gas dissolution/diffusion is a considerably less efficient migration mechanism than gas leakage by 2-phase flow into the rock matrix and through the EDZ. Situation 5) presents the most realistic situation, in that all gas storage and transport mechanisms are taken into account. Gas leakage by 2-phase flow and porewater displacement through gas pathways is found to be the most efficient gas transport mechanism for reasonably transmissive pathways (for a more detailed discussion see Section 5.4).

The following calculational cases are presented in this manner:

- Design option 1, with and without application of the gas breakthrough criterion to some higher transmissive geological feature, see Figure 5-8.
- Design options 2a and 2b, see Figure 5-9.
- Increased steel corrosion rates, see Figure 5-10.
- Decreased initial gas storage volume in the bentonite and decreased capacity for gas dissolution in the matrix, see Figure 5-11.
- Increased hydraulic length (distance over which gas-induced pressure gradient in the background rock is non-zero) and increased diffusive length (distance over which concentration gradient for dissolved gas in the background rock is non-zero), see Figure 5-12.
- Impermeable EDZ (no gas transport capacity of EDZ), see Figure 5-13.

The probabilistic results are presented in Figure 5-14 in terms of the expectation value of the maximal gas pressure in the deposition drifts as a function of the number of fractures per canister section and as a function of the steel corrosion rate. In these calculations gas dissolution, gas diffusion, gas leakage into EDZ, rock matrix and fractures and porewater displacement are taken into account.

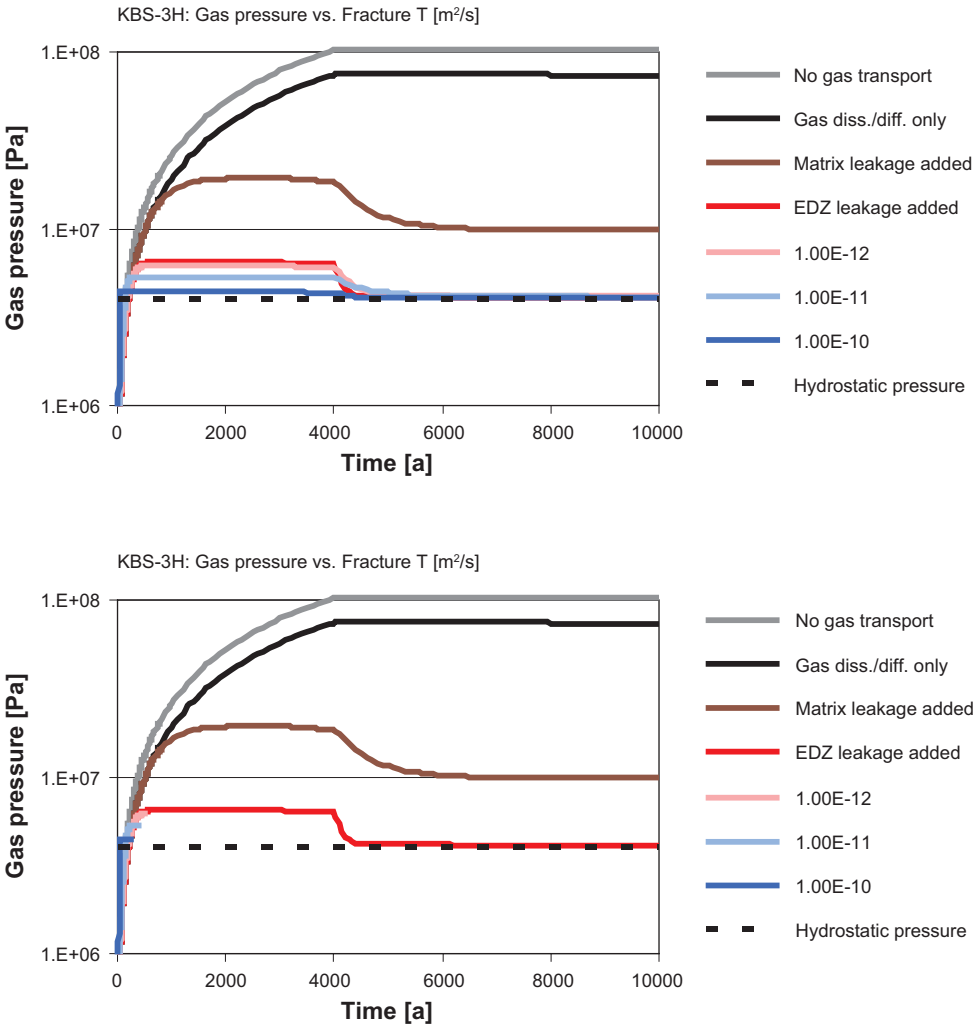

Figure 5-8. *Evolution of gas pressure in the deposition drifts at Olkiluoto for design option 1. Upper figure: no gas breakthrough criterion applied; lower figure: with application of breakthrough criterion to higher transmissive geological feature (z_{max} = 100 m).*
The pressure evolution is shown for several different cases: i) case without gas transport and dissolution, ii) case with gas dissolution and diffusion only, iii) case with gas leakage through matrix added, iv) case with gas leakage through EDZ added and v) cases with gas leakage and porewater displacement added, as a function of the hydraulic transmissivity of the representative pathway.

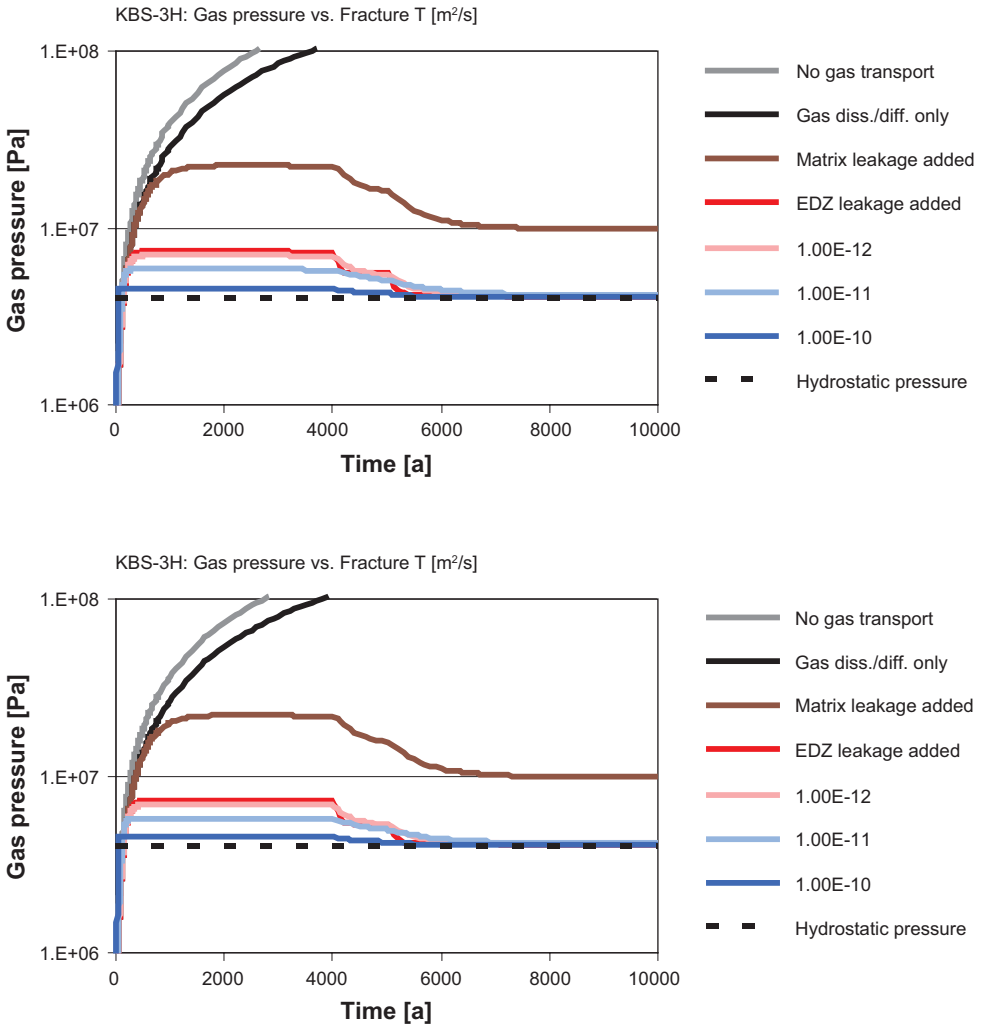

Figure 5-9. *Evolution of gas pressure in the deposition drifts at Olkiluoto.*
Upper figure: design option 2a; lower figure: design option 2b.
The pressure evolution is shown for several different cases: i) case without gas transport and dissolution, ii) case with gas dissolution and diffusion only, iii) case with gas leakage through matrix added, iv) case with gas leakage through EDZ added and v) cases with gas leakage and porewater displacement added, as a function of the hydraulic transmissivity of the representative pathway. No gas breakthrough criterion to higher transmissive geological feature is applied in these figures.

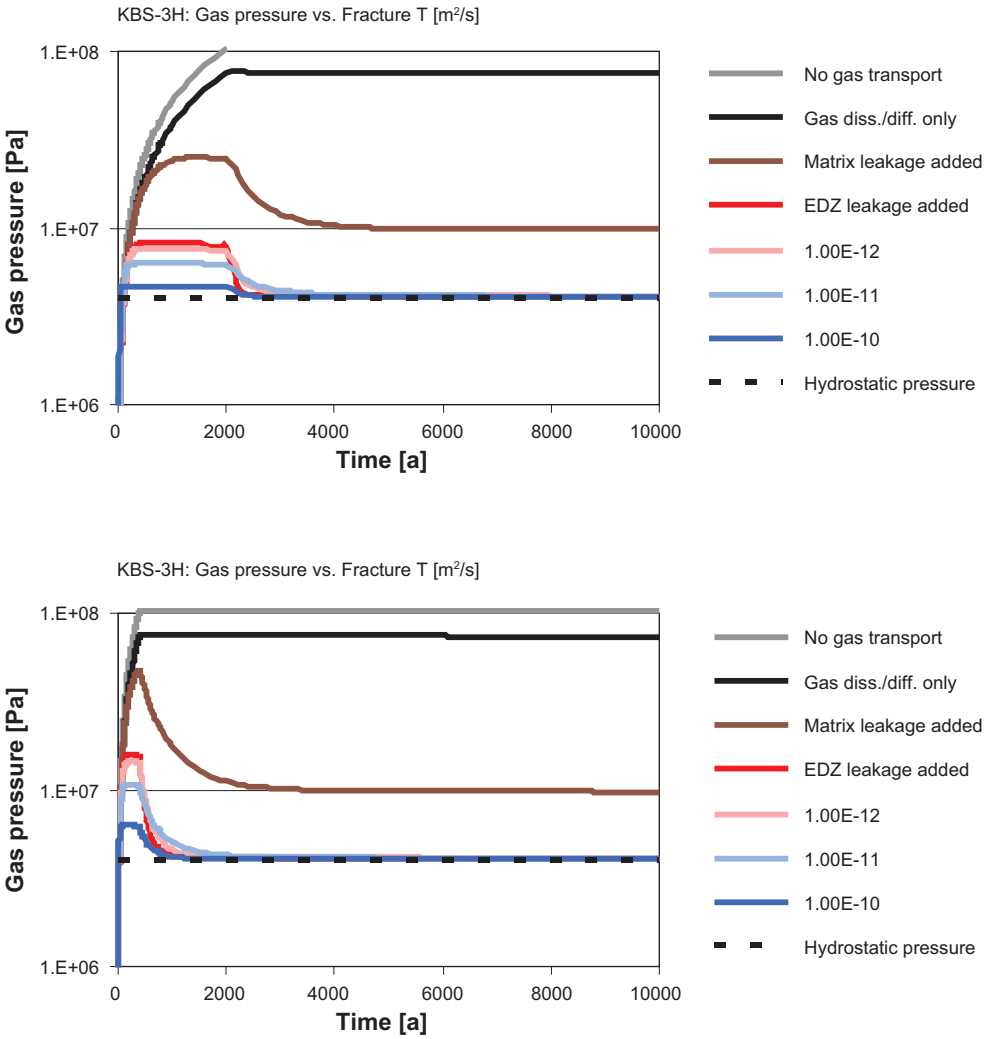

Figure 5-10. *Evolution of gas pressure in the deposition drifts at Olkiluoto (option 1) for increased steel corrosion rates.*
Upper figure: R = 2 µm a^{-1}; lower figure: R = 10 µm a^{-1}.
The pressure evolution is shown for several different cases: i) case without gas transport and dissolution, ii) case with gas dissolution and diffusion only, iii) case with gas leakage through matrix added, iv) case with gas leakage through EDZ added and v) cases with gas leakage and porewater displacement added, as a function of the hydraulic transmissivity of the representative pathway. No gas breakthrough criterion to higher transmissive geological feature is applied in these figures.

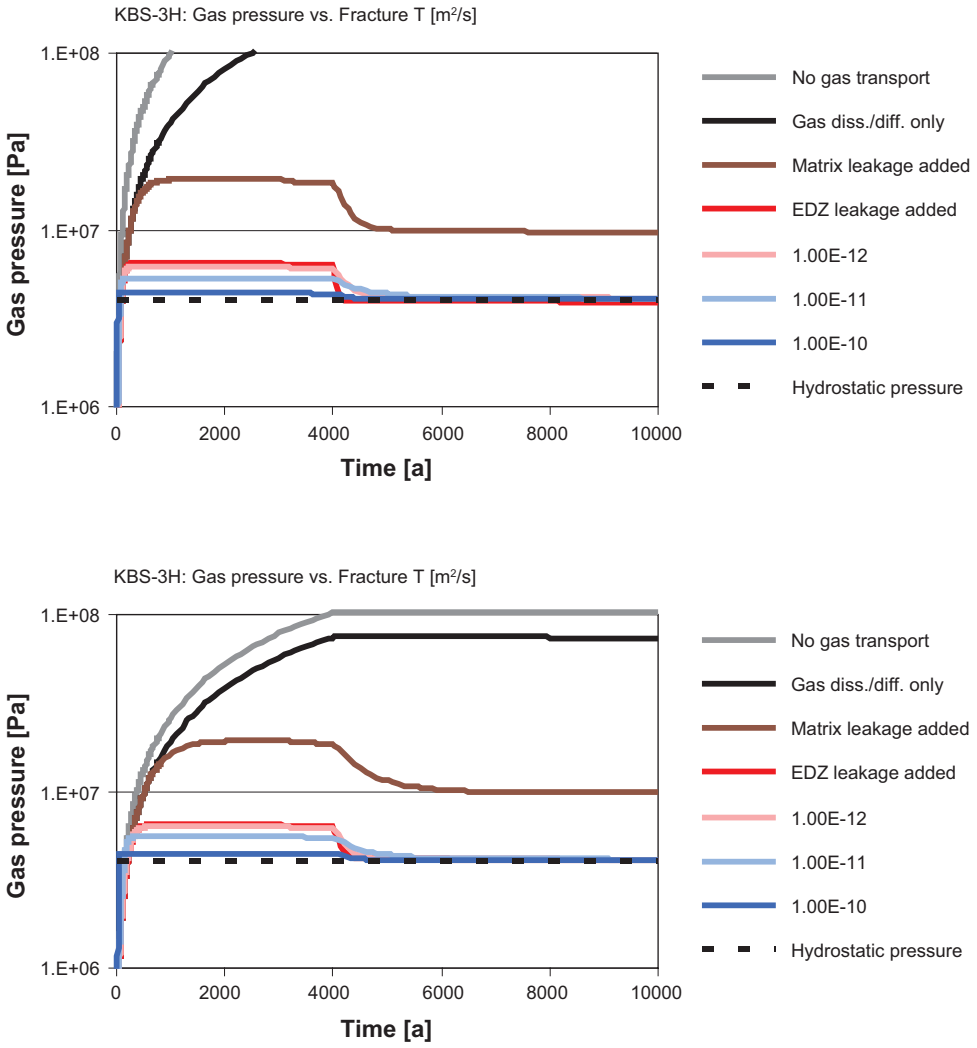

Figure 5-11. *Evolution of gas pressure in the deposition drifts at Olkiluoto (option 1). Upper figure: decreased initial gas storage volume in the bentonite (Δr = 0.01 m instead of 0.04 m); lower figure: decreased gas dissolution volume in host rock ($f_{sol,m}$ = 0.001 instead of 0.01). The pressure evolution is shown for several different cases: i) case without gas transport and dissolution, ii) case with gas dissolution and diffusion only, iii) case with gas leakage through matrix added, iv) case with gas leakage through EDZ added and v) cases with gas leakage and porewater displacement added, as a function of the hydraulic transmissivity of the representative pathway. No gas breakthrough criterion to higher transmissive geological feature is applied in these figures.*

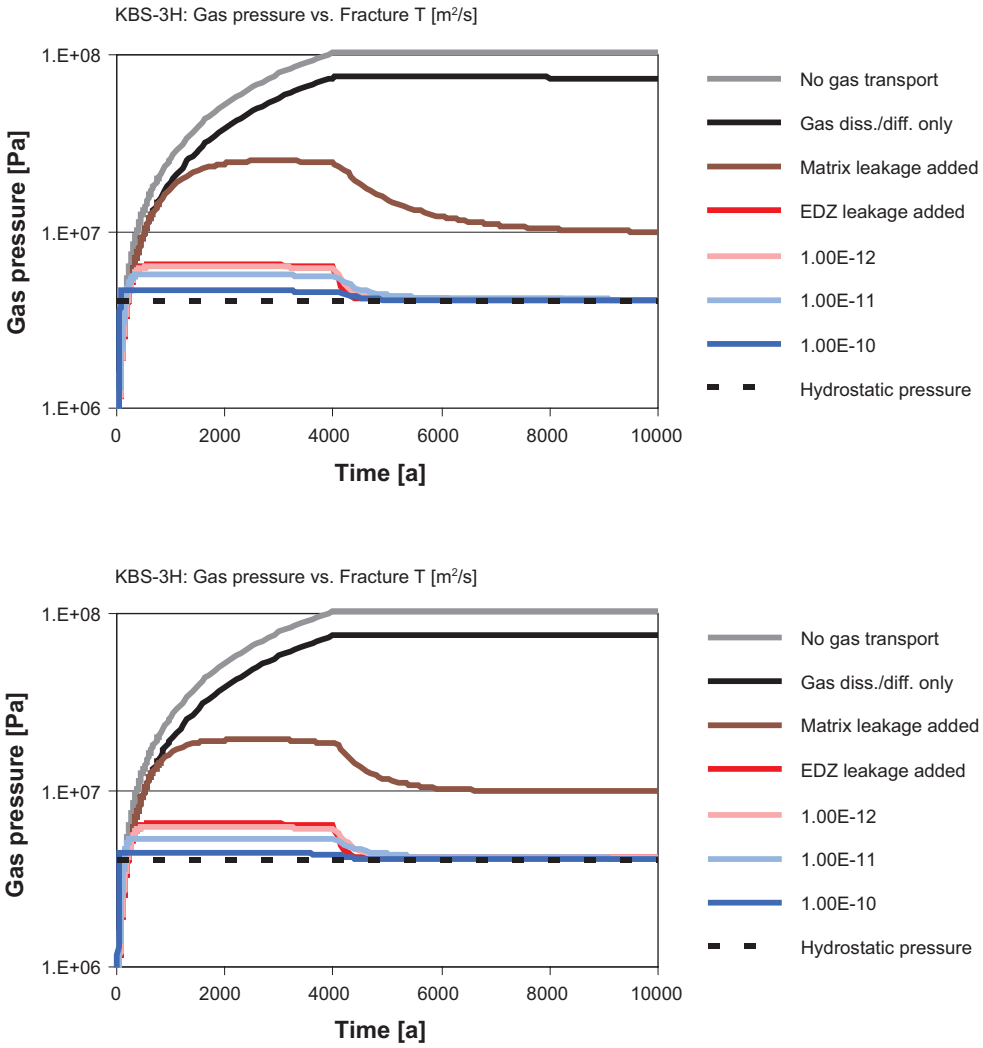

Figure 5-12. *Evolution of gas pressure in the deposition drifts at Olkiluoto (option 1). Upper figure: increased hydraulic length (l_h = 200 m instead of 100 m); lower figure: increased diffusive length (l_d = 10 m instead of 1 m).*
The pressure evolution is shown for several different cases: i) case without gas transport and dissolution, ii) case with gas dissolution and diffusion only, iii) case with gas leakage through matrix added, iv) case with gas leakage through EDZ added and v) cases with gas leakage and porewater displacement added, as a function of the hydraulic transmissivity of the representative pathway. No gas breakthrough criterion to higher transmissive geological feature is applied in these figures.

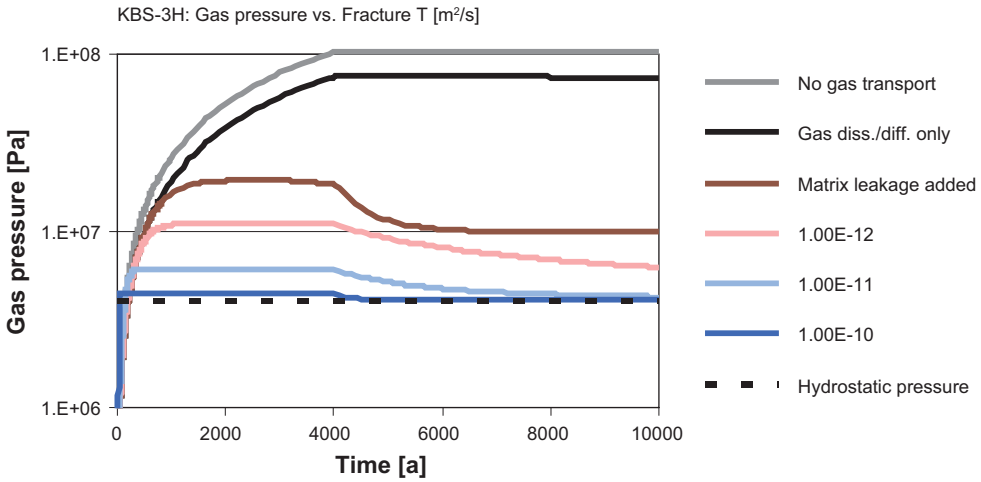

Figure 5-13. *Evolution of gas pressure in the deposition drifts at Olkiluoto (option 1). For an impermeable EDZ (no gas transport capacity for the EDZ assumed, $k_{g,EDZ}$ = 0 m²). The pressure evolution is shown for several different cases: i) case without gas transport and dissolution, ii) case with gas dissolution and diffusion only, iii) case with gas leakage through matrix added, and iv) cases with gas leakage and porewater displacement added, as a function of the hydraulic transmissivity of the representative pathway. No gas breakthrough criterion to higher transmissive geological feature is applied in these figures.*

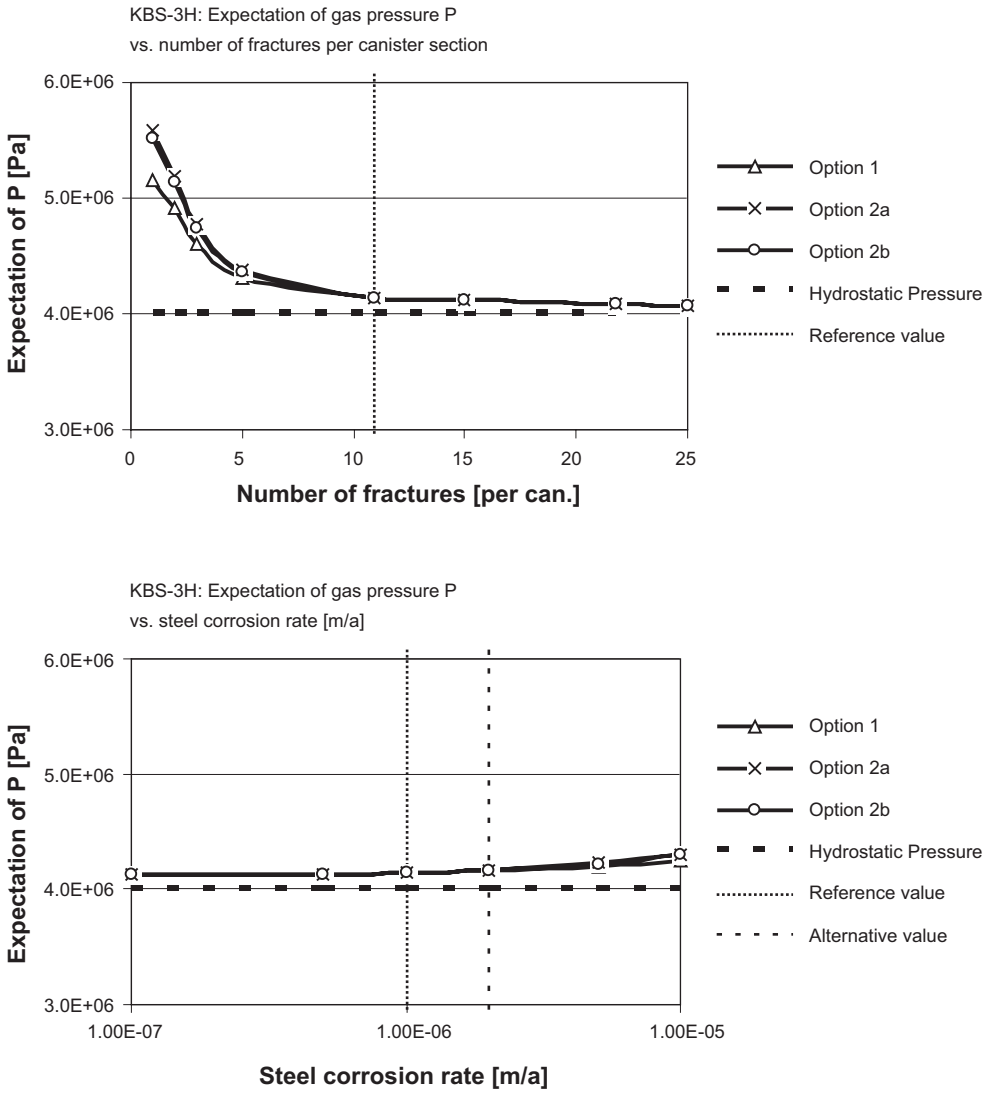

Figure 5-14. *Expectation value of maximal gas pressure in the deposition drifts at Olkiluot taking gas dissolution, gas diffusion, gas leakage into EDZ, rock matrix and fractures and porewater displacement into account.*
Upper figure: Variable number of fractures per canister section (the reference value for the number of fractures per canister corresponds to a linear fracture density along boreholes of 1 fracture per metre); lower figure: Variable steel corrosion rate.
No gas breakthrough criterion to higher transmissive geological feature is applied in these figures.

5.4 Summary and discussion of relevant gas processes

Gas generation in the deposition drifts starts immediately upon contact of water with steel surfaces, where gas is predominantly produced by anaerobic steel corrosion. The quantities of steel present in the deposition drifts are moderate, about 1–2.5 tons per canister, depending on the design option envisaged. Other gas-generating materials are either absent or exist in quantities too small to contribute significantly to gas production.

The overall gas production is in the order 550 to 1,300 m^3 H_2 (STP) per canister. These gas volumes are relatively low, particularly because the intact copper-iron canisters will not contribute to gas generation for the time period of interest for safety.

The gas production *rates* are, however, significant, mainly because the supercontainer and other structural materials provide relatively large surface areas for steel corrosion. The time needed for complete corrosion of the entire steel inventory is comparatively short (about 5,000 years for the reference steel corrosion rate of 10^{-6} m a^{-1}).

The generated hydrogen gas, as well as gas entrapped at the time of closure, will dissolve in the near field pore water until the solubility limit at repository pressure is reached. Dissolved gas diffuses through the drift walls into the host rock. The pressure of the free gas phase increases as a result of the ongoing generation of gas. In the near field, the pressure increases until gas pathways from the steel surfaces through the bentonite are created. This results in gas storage volumes being created, mainly within bentonite in the vicinity of the steel surfaces, but also in the EDZ. If the gas generation rate exceeds the rate of gas removal (by dissolution/diffusion) and gas volume increase (by porewater displacement), then the gas pressure rises further.

When the gas pressure exceeds the threshold for capillary leakage (formation pore pressure of 4 MPa plus gas entry pressure of fractures), leakage of gas into existing fractures takes place. This involves porewater displacement and advection of dissolved gas within the fractures as well as diffusion of dissolved gas from the fractures into the rock matrix. The magnitude of the gas pressures reached in the drifts strongly depends on the gas transport capacity of fractures and may thus vary considerably along a deposition drift. Of particular importance is the hydraulic transmissivity T_{max} of the most conductive gas pathway in each canister section, because this feature is expected to dominate gas transport away from the deposition drifts:

- for $T_{max} \geq 10^{-10}$ m^2 s^{-1}, the maximal gas pressure remains slightly above hydrostatic pressure (about 4 MPa at a depth of 400 m),
- for $T_{max} < 10^{-10}$ m^2 s^{-1}, the maximal gas pressure is in the order of a few MPa above hydrostatic pressure, but still below the minimal principal stress (about 9 MPa at a depth of 400 m).

In extremely tight canister sections, considerable pressures are reached and gas pathways may be formed by reactivation of low-permeability fractures in the host rock or by penetration through or around the distance blocks. This point is further discussed in Chapter 6.

Gas transported through the host rock will eventually reach major geological features with enhanced transmissivity, through which gas will migrate to the surface. After breakthrough, the gas pressure in the deposition drifts will reach an equilibrium. After gas generation ceases, the pressure returns to ambient pressure at repository depth at a rate determined mainly by the fracture transmissivities in each canister section.

The results of the gas analysis illustrate that there is – for the purpose of the present stage of repository development – enough detailed scientific understanding of gas production in and release from a repository sited in fractured host rock at Olkiluoto to make a provisional assessment of the impacts of gas on the KBS-3H disposal system. The envisaged system is considered to be robust with regard to gas buildup and release, i.e. gas pressures increase slowly and various mechanisms of transport are capable of transporting the gas gradually through the host rock or through the tunnel system without significantly disturbing the isolation characteristics of the repository system.

A number of more detailed analyses are needed, however, to adress the characteristics and performance of fracture network systems both in the EDZ and in the background rock. In particular, the EDZ properties at repository depth at Olkiluoto (permeability, porosity and depth of fracturing) remain somewhat uncertain. These properties of the EDZ are subject to a variety of rock-specific and site-specific conditions as well as to the repository layout and engineering techniques applied (rock strength, rock stress at repository level, orientation and size of the drifts, excavation method). If the EDZ were more permeable or would extend to greater depths, as observed in the Grimsel rock laboratory /Marschall et al. 1999/, then transport of gas bypassing the distance blocks would be enhanced, leading to lower gas pressures in very tight canister sections. On the other hand, if self-sealing processes (drift convergence, bentonite swelling, calcite precipitation, bentonite intrusion) would lead to a reduction of the gas transport capacity of the EDZ, the hydraulic separation of individual canister sections would be more pronounced and, as a consequence, increased gas pressures in tight sections would be expected (see Figure 5-13). Thus it seems necessary to further investigate the properties of the EDZ under repository-like conditions and, where possible, to include results from other studies on EDZ properties.

More detailed analysis of the properties of the fracture network in the background rock seems also necessary. The simplified model calculations presented in this report do not map the complex structure of the fracture network. In particular, there remains significant uncertainty, under which conditions the percolation threshold for gas migration is exceeded. Further analyses are needed to clarify this point. In particular, the fracture connectivity relevant for gas migration could be tested by calculating the percolation threshold for gas migration using a fracture network model along the lines of the DFN model presented by /Poteri and Laitinen 1999/. Such an analysis would provide more reliable information on the hydraulic transmissivity of gas pathways that are to be expected at the Olkiluoto site.

6 Analysis of mechanical processes

6.1 General considerations

For the vertical emplacement concept, KBS-3V, a detailed discussion of mechanical processes in the engineered barriers and near-field rock is given in the Process Report for SR 97 /SKB 1999b/. This material was updated by Posiva in a separate Process Report for the spent fuel repository at Olkiluoto /Rasilainen 2004/. In these reports, the discussion is structured as follows:

- mechanical interaction buffer/backfill,
- mechanical interaction buffer/canister,
- mechanical interaction buffer/near field rock,
- mechanical interaction backfill/near-field rock,
- thermal expansion.

In the present analysis of mechanical processes for the horizontal emplacement concept, KBS-3H, it is not intended nor necessary to repeat all the arguments and process descriptions in these two Process Reports. This is because

- no backfill is foreseen in the deposition drifts for KBS-3H,
- the buffer/canister interactions and thermal issues are similar in the horizontal and vertical emplacement concepts,
- the present report is focussed on issues that are specific to KBS-3H.

For these reasons, the focus of the present chapter is on the mechanical processes within the engineered barriers (buffer, supercontainer, distance block) and near-field rock, and particularly on those that are identified in the FEP analysis as being specifically relevant for the KBS-3H design (see Table 3-3). Note that in Chapter 3, these processes are termed ‘additional FEPs for KBS-3H’, because they were either not identified or discussed from a different viewpoint in the FEP analysis for KBS-3V. These FEPs are listed in rearranged form in Table 6-1.

6.2 Mechanical processes within engineered barriers and near-field rock

6.2.1 Mechanical processes within engineered barriers

In KBS-3H, the main elements of the engineered barriers are the canister surrounded by its bentonite buffer, the supercontainer, the distance block and structural materials (steel rings and feet). The role of bentonite in the performance of the near-field is of major importance. In this section, the mechanical issues related to the interaction between bentonite, supercontainer and structural materials are discussed. The issues related to interactions between engineered barriers and near-field rock are addressed in Section 6.2.2.

By absorption of water during resaturation of deposition drifts, the bentonite buffer inside the supercontainer and the distance blocks swell. A detailed discussion of bentonite swelling and development of swelling pressure is given in the Process Report for SR 97 /SKB 1999b/ and in the Process Report for the repository at Olkiluoto /Rasilainen 2004/. Given the dry density of bentonite blocks of 1.56 kg m^{-3} envisaged for KBS-3H, the saturated bentonite densitiy and porosity are expected to be 2,000 kg m^{-3} and 44%, respectively (see Section 4.2 and Table A-1).

Table 6-1. Additional FEPs related to the mechanical behaviour of KBS-3H. These FEPs are taken from Table 3-3. In the first row, the FEP number is given. The last column indicates where a description of the FEPs can be found in the present report.

No.	Additional FEPs for KBS-3H	Section were FEP is discussed
3.12, 4.12, 12.3	Effect of buffer swelling on supercontainer Resistance to swelling of smectite by supercontainer Breaching of supercontainer	6.2.1 4.4.3, 6.2.1 6.2.1
12.8	Effect of supercontainer on water flow paths along the periphery of the drift	4.3.3, 6.2.1
12.3/12.10/12.11	Effect of expansion (magnetite formation) on bentonite, host rock and reinforcements or reduced swelling pressure due to Fe-silicate formation	6.2.1 4.4.2. 6.2.7
4.12/6.12/8.12/10.12	Pressurization of supercontainer by bentonite porewater, gas, groundwater and rock	6.2.1
13.3, 3.13, 13.12	Displacement of supercontainer/buffer by swelling of distance blocks Effects of buffer swelling pressure on distance block, including displacement of distance blocks Breaching of end plates of supercontainer	6.2.1
6.13/8.13 (8.3/8.5)	Piping and erosion by gas and water at interface to host rock	2.2, 5.3.3, 6.2.1
13.6	Cut-off of gas pathways along drifts by swelling of distance blocks	5.3.3, 6.2.2
7.12, 12.7	Thermal effects on supercontainer (expansion/contraction, structural alterations, pressure changes) Heat transport, heat radiation across gaps around supercontainer	6.2.3

This results in a maximal swelling pressure of 7–8 MPa. A number of processes may, however, lead to a reduction of the maximal swelling pressure:

- various geochemical processes,
- swelling of bentonite through perforated supercontainer into void space between supercontainer and rock,
- bentonite intrusion and subsequent bentonite erosion into fractures in the near-field rock,
- bentonite erosion during resaturation of deposition drifts by flowing water along the drifts,
- axial displacement of distance blocks and/or supercontainer due to premature or asymmetric/asynchronous bentonite swelling.

The effects of geochemical processes (Fe-iron interactions, interaction with saline groundwater, etc) on bentonite swelling are discussed in detail in Chapter 4. The analyses of Fe-iron interactions show that the reduction of bentonite swelling pressure may be as high as 50%, under the assumption of complete conversion of the smectite fraction to an Fe-silicate such as berthierine. The interaction of bentonite with saline water from upconing at Olkiluoto may reduce the swelling pressure likewise by up to 50%. It is noted in Chapter 4 that even in these extreme cases there is substantial residual swelling capacity of bentonite.

Swelling of bentonite through the holes of the supercontainer has been analysed during the Basic Design phase in 2003. The analysis showed that the maximal swelling pressure is reduced when bentonite swells through the holes and further when it swells into the void space between supercontainer and rock. The swelling pressure difference within and outside the supercontainer was estimated to be 2–3 MPa. This difference in swelling pressure results in considerable forces acting outwards on the steel shell of the supercontainer. The mechanical resistance of the thin steel shell (thickness 8 mm) is expected to be limited and elasto-plastic deformations will inevitably take place. Rupturing of the steel shell may occur, most likely at or near the circular edges of the supercontainer (end-plates) where the stresses are expected to be highest, and as result of

the ongoing corrosion and weakening of the steel. A quasi-stationary state of stress equilibrium is reached when all forces acting in the system (including the force caused by volume expansion of corrosion products, by gas pressure build-up, formation pore pressure and rock stress) are balanced, resulting in a homogenization of bentonite swelling pressures inside and outside the supercontainer. The time to reach this equilibrium depends on a number of rates and factors, including the steel corrosion rate and the various mechanisms affecting gas pressure build-up and bentonite swelling.

Under repository conditions, the lifetime of steel, i.e. the time needed for its complete corrosion, is estimated to be about 4,000 years (Section 4.3.3). Pitting corrosion is not expected to significantly affect the mechanical performance of the supercontainer. In the majority of corrosion experiments under repository conditions, the dominant steel corrosion product is magnetite, a very stable and insoluble phase (Section 4.3.2). The formation of magnetite involves a volume increase of about a factor of two. In the case of various other possible corrosion phases, the volume increase may be even higher. As pointed out in Section 4.3.2, for the case of complete conversion of the supercontainer steel shell into magnetite, an average decrease in bentonite buffer porosity of about 2% would occur. This would lead to an average increase in swelling pressure of the bentonite buffer by about 1 MPa. The pressure increase due to magnetite formation by corrosion of the supercontainer and other structural materials (steel rings in design options 2a/b, steel feet) also affects the distance blocks and the near-field rock. The effects of the exerted forces diminish, however, with the volume of the affected material and quickly average out with increasing distance to the origin of volume increase (steel).

Forces exerted by the host rock on the engineered barriers may be caused by rock creep, subsequent drift convergence and increase of bentonite density. The largest deformations of rock are expected during the construction and operation phase of the deposition drifts. After sealing of the drifts, rock creep rates are expected to be small and the effects on the engineered barriers are considered to be insignificant.

The question has been raised whether the corroded supercontainer and the mineralogycally changed bentonite outside the supercontainer could – in the long run – lead to increased water flow along the periphery of the deposition drift. Such a situation would lower the concentration of dissolved radionuclides at the outer boundary of the buffer and would thus enhance diffusive radionuclide flux through the buffer. As noted in Chapter 4, there is substantial residual swelling pressure of the buffer even under very pessimistic assumptions on Fe/bentonite interaction. Moreover, when a quasi-stationary stress equilibrium is achieved, significant pressures are exerted on all parts of the engineered barrier system. Under such conditions it is difficult to imagine the presence of larger voids for this rather soft material made of clay and corrosion products. Hence, we do not expect a significantly increased hydraulic conductivity (other than the EDZ) persisting for long periods of time at the drift periphery. It may be useful, however, to evaluate the effect of compressive stress on the porosity (and permeability) of materials with different mechanical strength properties in a further study.

The issue of bentonite intrusion into fractures in the near-field rock has been raised in /SKB 1999b/ in the context of KBS-3V, but is likewise relevant for KBS-3H. Depending on the conditions in the near-field rock, the clay in the fractures could be transported away, allowing new clay to penetrate, which would result in gradual erosion of the buffer. Two types of erosion have been identified: mechanical erosion (particle transport by flowing water), and chemical erosion (dispersion of clay gel by low salinity water). It was concluded in /SKB 1999b/ that the risk of mechanical or chemical erosion of large quantities of bentonite is small and is not of significance for the long-term performance of the repository. Because of the similarity of the processes involved, the same conclusion can also be drawn for KBS-3H.

As pointed out in the context of the description of the design options (Section 2.2), a number of issues related to the mechanical behaviour of the distance blocks are raised:

In the case of design option 1 (open tunnel option), premature swelling of the distance blocks may lead to pressurization of one canister section before the neighboring canister section is

properly emplaced. In such a case, large axial hydostatic forces may be exerted and – in the worst case – a displacement of the distance block may occur. A displacement of the distance block is also conceivable if the buffer swells prior to the distance block. On the other hand, a displacement of the supercontainer is also possible if asymmetric swelling of the confining distance blocks occurs. Also, the effects of air humidity and water dripping from the drift walls on the bentonite blocks may lead to bentonite erosion by flowing water along the drifts (see Section 2.2). It is clear that such situations must be avoided or their effects mitigated by design measures (e.g. by preventing premature or asymmetric/asynchronous water contact), to ensure the safety functions of the bentonitic barriers in KBS-3H.

In the case of design options 2a/b (tight tunnel option), a steel ring bolted to the rock counteracts axial forces onto the distance block exerted by the rise of hydraulic pressure and by swelling of bentonite blocks. It is noted that the effects related to water pressure increase and hydrostatic forces are much more pronounced for design options 2a and 2b than for design option 1. Again the engineered barriers must be designed in such a way that axial displacement of both distance blocks and supercontainer are prevented.

6.2.2 Mechanical interactions between engineered barriers and near-field rock

In situ stresses have been measured at Olkiluoto at a depth of 300–800 m in several boreholes /Johansson et al. 2002, Posiva 2003/. The results show that the maximal principal stress (σ_1) at a depth of 400 m amounts to about 20 MPa. The orientation of σ_1 is dipping by 30° towards SE (120°)[7]. In the design of KBS-3H, it is foreseen to align the axis of the deposition drifts as much as possible with the orientation of σ_1.

In the framework of the analyses of coupled hydro-mechanical processes affected by gas, the relevant mechanical quantity is the minimal principal stress (σ_3). At a depth of 400 m, σ_3 is about 9 MPa, with a dip of about 55° towards NW (320°). Fracture planes oriented perpendicular to σ_3 (i.e. sub-horizontal planes dipping from NW to SE) experience thus the lowest normal effective stress and are prone to be reactivated first.

As discussed in Chapter 5, considerable amounts of hydrogen gas are generated by anaerobic corrosion of steel. Because the generated gas cannot be stored and/or dissolved in sufficient quantities within the near-field and surrounding rock, a free gas phase is sustained and gas pressure rises until the losses of gas into the surrounding rock and along the deposition drifts balances the generation of gas. Depending on the gas transport capacity of the host rock, gas pressures are estimated to rise considerably above the hydrostatic pressure at repository depth. When the gas pressure is near or above σ_3, reactivation of sub-horizontal fractures in the near-field rock may occur. Because these fracture planes are most likely oriented in the same direction as the planned deposition drifts (NW-SE, see above), it is possible that continuous gas pathways are formed along the drifts. These pathways may thus hydraulically connect neighboring canister sections.

Two points are worthwhile noting in this context: i) The role of gas breakthrough through or around the distance blocks, and ii) the role of gas pathways for the subsequent radionuclide transport.

Concerning the first point, the important role of axial gas pathways away from tight canister sections (i.e. where the host rock is basically impermeable) has been demonstrated in Chapter 5. In addition to the reactivation of fractures in the near-field rock (see above), the following situations are conceivable:

- Gas may percolate through the thin EDZ around the distance blocks, either by two-phase flow (displacement of water in existing fractures) or by reactivation/creation of fractures.

[7] The orientations of the principal stress components are indicated with respect to a lower-hemisphere projection.

- Gas pathways may be created through the body of the distance blocks, either by two-phase flow (displacement of water in capillaries) or by microfracturing and pathway dilation[8].
- Gas pathways may form at the distance block/rock interface.

Note that the gas calculations performed in Chapter 5 are based on the assumption that the EDZ around the distance blocks provides some gas transport capacity, as described in the first of the above situations. There is, however, considerable uncertainty on the effect of self-sealing processes (drift convergence, bentonite swelling, calcite prescipitation, bentonite intrusion) on the transport capacity of the EDZ in the post-closure phase. For this reason, a special calculational case assuming an impermeable EDZ was also investigated (see Figure 5-12).

Laboratory studies by /Pusch et al. 1985, Horseman et al. 1999/ and /Tanai et al. 1997/ show that gas breakthrough within bentonite occurs at a pressure approximately equal to the sum of the bentonite swelling pressure (7–8 MPa) and the hydrostatic pressure (4 MPa at a depth of 400 m), i.e. at approximately 11–12 MPa. Similar breakthrough pressures are expected for the bentonite/rock interface and for the thin EDZ considered in this report (see Section 2.4). This is because the swelling pressure of the distance blocks is directly exerted on the EDZ, where it may, by reducing microfracture apertures, contribute to the threshold pressure for gas breakthrough. The above gas breakthrough pressure (11–12 MPa) is significantly higher than the minimal principal stress at repository depth (σ_3 = 9 MPa). This seems to indicate that the reactivation of fracture planes in the near-field rock takes place at lower pressures than gas breakthrough within or around the distance blocks. However, if the swelling pressure of bentonite is significantly reduced for any one of the reasons discussed in Section 6.2.1, the threshold pressures for gas breakthrough within or around the distance blocks and within the near-field rock may be similar. Irrespective of the uncertainty about the detailed mechanisms for gas migration, gas generated within the deposition drifts will be able to create or reactivate pathways through which it can escape from extremely tight drift sections, provided the pressure rises to the required levels.

Concerning the second point stated above: Continuous gas pathways in the near-field rock between neighboring canister sections may form preferential pathways for the subsequent transport of radionuclides, even though gas generation may have stopped long before the onset of radionuclide release from the canisters. Such preferential pathways are expected to be limited to initially extremely tight drift sections. Interestingly enough, this would seem to lead to a leveling-out of the transport capacity (for gas and radionuclides) along the drifts between very tight drift sections (where gas pathways are likely to be formed) and more permeable drift sections (where gas can dissipate through existing fractures).

6.2.3 Thermal effects

Thermal effects in the canister/buffer sub-system are similar in the vertical and horizontal emplacement concept. Moreover, a detailed discussion of thermal effects is outside the scope of the present (HMCBG) report. It is noted, however, that the thermal transient will be essentially over before gas pressures become significant, thus temperature increases can be decoupled from gas transport phenomena. The discussion of thermal effects is thus kept short and concentrated on the issues related to the presence of the supercontainer:

- Thermal effects on supercontainer (expansion/contraction, structural alterations, pressure changes).
- Heat transport, heat radiation across gaps around supercontainer.

Due to the transient temperature increase and subsequent decrease, the supercontainer experiences thermal expansion/contraction and possibly some structural alterations. These effects

[8] It must be noted, however, that the detailed processes involved in gas transport through bentonite are still under debate /Nagra 2002/.

may be enhanced by increased temperatures due to a reduction of the heat transport capacity by gaps initially present around the supercontainer. These gaps are expected to close relatively rapidly due to the swelling of bentonite. Given that the maximal temperatures within bentonite remain below 90°C (10°C below the design basis maximum of 100°C), the effects of the above mentioned processes are expected to be insignificant. Likewise, structural alterations induced by thermal gradients are not significant under the expected thermal conditions in the repository.

Pressure increases within the engineered barriers and the near-field rock may be induced by rising temperatures via a decrease of the density of water in the fully saturated state. However, it has been noted by /Rasilainen 2004/, that this process does not occur until full saturation of the near-field is achieved, because of the high compressibility of the gas phase. The results presented in Chapter 5 indeed show that for a prolonged period of time full saturation is not likely to be reached. Significant thermally-induced pressure increases are therefore not expected to occur.

6.3 Summary of relevant mechanical processes

Bentonite swelling within the buffer and distance blocks leads to maximal swelling pressures in the order of 7–8 MPa. The swelling pressure may, however, be reduced by geochemical processes and by bentonite dilution due to intrusion of bentonite into void space either initially present (around supercontainer, within fractures) or created by relative displacement of distance blocks and supercontainer, and by subsequent mechanical and chemical erosion.

The expected difference of swelling pressure inside and outside the supercontainer may lead to considerable forces acting on the perforated steel shell and to elasto-plastic deformations. Rupturing of the steel shell may occur, most likely at or near the circular edges of the end-plates where the stresses are highest. After a quasi-stationary stress equilibrium is reached, a homogenization of bentonite swelling pressure inside and outside of the supercontainer is expected. The formation of magnetite by anaerobic corrosion of steel involves a volume increase of about a factor of 2, leading to a slight increase in bentonite density and swelling pressure.

Premature or asymmetric swelling of the distance blocks induce axial forces and – in the worst case – lead to the displacement of distance blocks and/or supercontainer. It is noted that these effects are much more pronounced for design options 2a and 2b than for design option 1. Relative displacements and bentonite erosion by flowing water must be avoided or their effects mitigated by design measures.

The most relevant quantity for the mechanical interaction between engineered barrriers and near-field rock is the minimal principal stress (σ_3). At a depth of 400 m at Olkiluoto, σ_3 is about 9 MPa, with a dip of about 55° towards NW. Fracture planes oriented perpendicular to σ_3 (i.e. sub-horizontal planes dipping from NW to SE) experience thus the lowest normal effective stress and may thus be reactivated when gas pressure rises to values near or above σ_3. This may possibly lead to the formation of continous gas pathways that may play the role of preferential pathways in subsequent radionuclide transport. This possibility emphasizes the need to consider also other factors than the alignment of the deposition drifts with the maximal principal stress component.

There is also a possibility that gas pathways are formed through or around the distance block from very tight to more permable drift sections. There is, however, considerable uncertainty on the factors affecting the swelling pressure of bentonite and self-sealing of the EDZ, and thus on the threshold pressure for this transport mechanism. Irrespective of this uncertainty, gas generated within the deposition drifts will be able to create or reactivate pathways through which gas can escape from extremely tight drift sections, provided the pressure rises to the required levels.

Finally, it is noted that thermal effects related to the presence of the supercontainer are considered to be insignificant.

7 Summary of system evolution

The evolution of the repository system involving horizontally emplaced spent fuel canisters (KBS-3H) will, to some extent, depend on the design option envisaged for the distance block. Currently, three different design options are being studied. The open tunnel option, involves free water flow along the bottom of the inclined deposition drift in an initial phase after emplacement, when swelling of the distance blocks has not yet taken place. In the tight distance block option, two design variants are being studied, differing in the details of the distance block design, although both inhibiting free water flow along the drift axis because the distance blocks, in direct contact with the lower boundary of the tunnel, will rapidly saturate. It has been noted that premature or asymmetric swelling of the distance blocks may induce large axial hydrostatic forces that could – in the worst case – lead to a relative displacement of distance blocks and supercontainers. These effects are much more pronounced for the tight distance block option than for the open tunnel option. Relative displacements and bentonite erosion by flowing water must be avoided or their effects mitigated by design measures. The medium to long-term evolution of KBS-3H will, however, not be significantly affected by the details of the chosen design option, provided the distance blocks behave according to design.

During the period when the fluid pressure in the repository is less than the formation pore pressure, slow inflow of water from the host rock occurs and water saturation in the deposition drifts increases. Air in the void space between the supercontainer and rock as well as between the distance block and rock will be trapped. Full saturation is, however, not likely to be reached before the start of gas generation and a residual free gas phase will remain. Due to microbial activity and chemical processes, the system will quickly pass from oxidising to reducing conditions. Hydrogen gas generation by anaerobic corrosion of steel and swelling of bentonite will start almost immediately upon contact with inflowing water. The maximal bentonite swelling pressure is in the order of 7–8 MPa, but may be affected by a number of processes, including volume changes and geochemical processes. Volume changes are caused by formation of corrosion products and by bentonite dilution due to intrusion of bentonite into void spaces either initially present (around the supercontainer and within fractures) or created by relative displacements of distance blocks and supercontainer. This may be followed by mechanical erosion and chemical alteration of bentonite. Any pressure difference between the inside and outside of the supercontainer is expected to be equilibrated due to elasto-plastic deformations or rupturing of the steel shell, most likely at or near the circular edges of the end-plates where the stresses are highest.

The corrosion of the steel components present in the deposition drifts (supercontainer and structural materials such as rings and supporting feet) will be fairly rapid. For the expected steel corrosion rate of 1 μm a^{-1}, complete conversion of Fe^0 to oxidised Fe^{2+}/Fe^{3+} species may occur within a few thousands of years. This signifies that the *rates* of gas production (mainly hydrogen) are quite significant, although the overall amount of produced gas is relatively low. Gas production will not be limited by the availability of water even in very tight drift sections, because water vapour is sufficient to maintain the corrosion process. The main corrosion product will be magnetite. Depending on the groundwater composition, some iron sulphide and siderite may also be formed. Following the start of corrosion and for a prolonged period of time, corrosion-derived Fe(II) may react with the clay to form Fe(II)-rich silicates, which may lead to a reduction in the plasticity of the nearby bentonite (see below). Bacterial activity at or near the supercontainer surface may lead to an enhancement of localised corrosion and probably to destabilisation of the magnetite layer. Previous investigations indicate, however, that there will be no relevant bacterial activity in the inner part of the buffer by virtue of its small pore sizes and low water activity.

The generated hydrogen gas, as well as gas entrapped at the time of closure, will dissolve in the near field pore water until the solubility limit at repository pressure is reached, and will diffuse away from the source of gas production (steel). If the gas generation rate exceeds the rate of gas removal (by dissolution/diffusion) and gas volume increase (by porewater displacement mainly within bentonite in the vicinity of the steel surfaces, but also in the EDZ), then the gas pressure will rise until the threshold pressure for leakage of gas into existing fractures in the near-field rock is exceeded. This involves porewater displacement and advection of dissolved gas within the fractures as well as diffusion of dissolved gas from the fractures into the rock matrix.
The magnitude of the gas pressure reached in the drifts strongly depends on the gas transport capacity of fractures and in particular on the hydraulic transmissivity of the most conductive pathway in each canister section. The maximal gas pressure may thus vary considerably along a deposition drift, but is expected to remain somewhat above the hydrostatic pressure for most parts of the deposition drifts. In extremely tight canister sections, gas pressures may rise up to values near or above the minimal principal stress σ_3 (about 9 MPa at Olkiluoto). This means that fracture planes oriented perpendicular to σ_3, i.e. those that experience the lowest effective stress, may be reactivated by gas pressure build-up. This could lead to the formation of continuous gas pathways from very tight to more permeable canister sections through the near-field rock. Such gas pathways may play the role of preferential pathways in subsequent radionuclide transport. It is also possible that gas pathways are formed through or around the distance blocks. There is, however, considerable uncertainty in the state of stress and fracture network properties at the repository level at Olkiluoto, and in the factors and rates affecting the swelling pressure of bentonite and the self-sealing of the EDZ, and thus in the threshold pressure required for the formation of such gas transport pathways.

Gas migration through the host rock will take place predominantly by two-phase flow within existing fractures. Because the migration of gas generally takes place within the largest pores (lowest gas entry pressures), the gas pathways correspond to connected fractures with the highest overall hydraulic transmissivities. However, as noted in Chapter 5, the simplified analyses presented in this report do not map the complex structure of the fracture network in the host rock at Olkiluoto. In particular, there remains significant uncertainty regarding for which conditions the percolation threshold for gas migration through the host rock is exceeded. Once the gas has migrated some distance within the fracture network in the host rock, it will eventually reach major geological features with enhanced transmissivity, through which it will migrate quickly towards the surface. After breakthrough, the gas pressure in the deposition drifts will reach an equilibrium determined by the rates of gas generation and gas migration. Finally, after gas generaton ceases (after a few thousands of years), full saturation of the near-field will take place and the pressure will return to the ambient value at repository depth. The time needed for the return to normal hydraulic conditions is controlled mainly by the hydraulic transmissivities in each canister section. In extremely tight drift sections, full resaturation may require an additional several thousands of years.

After the period of steel corrosion, bentonite swelling and the subsequent return to normal hydraulic conditions, long-term geochemical interactions between the steel corrosion products and bentonite will take place. The characteristic time period for significant geochemical changes is in the order of tens to hundreds of thousands or even millions of years. As pointed out in Chapter 4, Fe(II) derived from the corrosion process has a high affinity for the clay which will lead to sorption and possibly to precipitation (perhaps with simultaneous oxidation) of Fe(II). This, in turn, may affect the smectite fraction by conversion to an iron-rich non-swelling clay. Based on the scarce available data, the most likely Fe silicate to form under repository conditions appears to be berthierine, which is a non-swelling 1:1 clay.

Several factors will limit the extent of Fe-clay interaction, including the precipitation of insoluble iron phases, the diffusion-limited transport of iron and the presumably low concentration gradient of Fe^{2+} between the corroded source and the inner parts of the buffer. Although the kinetics of neoformation of Fe silicates are not known, transport modelling suggests that only if there is complete transformation of all released Fe to Fe silicates will there be a significant reduction in bentonite swelling pressure and that this could occur only after some hundreds of thousands of years.

The presence of Fe in the bentonite may affect various properties that are relevant for radionuclide transport. The pH conditions are not expected to be significantly altered due to the large acid-base buffering capacity of the bentonite. Redox conditions in the vicinity of the supercontainer will be affected by the corrosion process, which will promote reductive precipitation of oxidised species such as U(VI) and Se(IV/VI), if these species have managed to escape from the canister. Sorption properties are not expected to be adversely affected by Fe-bentonite interaction. There remains, however, large uncertainty with regard to process understanding of the Fe-bentonite interactions and their effects on the physical properties of the buffer. Although the effects of mineralogical changes on the hydraulic properties of bentonite at the outside of the corroded supercontainer are not known, they are not expected to be safety-relevant because of significant radial swelling forces generated by the unaltered inner portions of the bentonite. From the current knowledge presented in this report, no serious effects on the integrity of the buffer have emerged.

Finally, it must be noted that the present study does not include an evaluation of the direct impact of gas on radionuclide transport. The most relevant processes are i) transport of volatile radionuclides in the gas phase and ii) transport of dissolved radionuclides by gas-induced displacement of contaminated porewater, including potential displacement of contaminated porewater from within a defective canister /Nagra 2002/. Given the fact that under normal conditions gas pressure build-up and radionuclide transport take place at very different time scales, direct detrimental effects of gas on radionuclide transport are unlikely. However, in the case of an initial canister defect, such effects cannot be excluded and may play a significant role. Although self-sealing of gas pathways in unaltered bentonite is expected to occur, potential gas pathways created during an early phase of repository evolution within the potentially altered outer region of the bentonite, EDZ and host rock may indirectly affect radionuclide transport at later times. Such effects may occur within very tight tunnel sections, i.e. they are not expected to affect the system on a larger spatial scale.

8 Conclusions

The work presented in this study concerns analyses of the hydro-mechanical-chemical-microbiological processes related to the steel components of the horizontal emplacement concept (KBS-3H) of a repository for spent fuel sited at Olkiluoto. The results of the analyses illustrate that there is a good overall scientific understanding available on gas production in and release from a repository as well as its relationship to hydraulic, mechanical and geochemical issues.

Currently, three different design options for the distance blocks are under investigation. While the details of the design may influence the short to medium term performance, it is found that the medium to long-term evolution of KBS-3H is not significantly affected by the chosen design option, provided the distance blocks behave according to design.

Based on the understanding developed on gas production by anaerobic corrosion of steel components in the deposition drifts and gas transport mechanisms and capacities in the engineered barrier system and host rock, a simplified model of gas pressure evolution and gas migration in the disposal system has been developed. This model suggests that gas is predominantly transported by two-phase flow through the fracture network in the host rock. For the major part of the drift sections, there is sufficient transport capacity for gas to escape through the host rock and the calculated gas pressure increases are found to be moderate. In extremely tight drift sections, however, the maximal gas pressures may rise to values near or above the minimal principal stress. Under such conditions, reactivation of low-permeability fractures in the near-field rock cannot be excluded. It is also noted that currently there is significant uncertainty on the factors and rates that control axial gas pathway formation through or around the distance blocks.

For a prolonged period of time, corrosion-derived iron may react with bentonite to form iron-rich silicates, which may lead to a reduction in the plasticity and swelling pressure of the bentonite in the vicinity of the supercontainer. However, no serious effects on the integrity of the inner part of the buffer have emerged. Uncertainties with regard to process understanding of the iron/bentonite interactions and their effects on the physical properties of the affected part of the buffer remain to be analysed in future project stages.

Although no analyses of radiological consequences have been performed in the framework of this report, the presented information can be used to perform an assessment of the safety-relevant impacts of the steel components in the KBS-3H disposal system. Various mechanisms are capable of transporting the gas gradually through the host rock or through the tunnel system without significantly disturbing the isolation characteristics of the repository system, although reactivation of very low-permeability fractures intersecting the tunnel cannot be ruled out under some conditions. Nonetheless, given the overall large-scale permeability of the fracture network, this is unlikely to significantly alter subsequent hydraulic and radionuclide transport. It should be noted that the generation of large amounts of gas in the repository changes – to some degree – the conditions in the overlying geology. Leakage of large amounts of gas through several hundred metres of rock in the course of thousands of years may be perceived as a perturbation of the natural state of the site.

References

Andra, 2001. Materials Baseline Volume 4. Corrosion of metallic materials. Andra Report C.RP.AMAT.01.060, Paris, France.

Autio, J, 1996. Characterization of the excavation disturbance caused by boring of the experimental full scale deposition holes at TVO-Research Tunnel, Report POSIVA-96-09, Posiva Oy, Helsinki, Finland.

Autio J, Hjerpe T, Siitari-Kauppi M, 2003. Porosity, Diffusivity and Permeability of EDZ in Crystalline Rock and Effect on the Migration in a KBS-3 Type Repository. CLUSTER conference on "Impact of the EDZ on the performance of radioactive waste geological repositories", Luxembourgh 3–5 November 2003.

Baeyens B, Bradbury M H, 1997. A mechanistic description of Ni and Zn sorption on Na-montmorillonite. Part I: Titration and sorption measurements. J. Contam. Hydrology 27, 199–222.

Bradbury M H, Baeyens B, 1997. A mechanistic description of Ni and Zn sorption on Na-montmorillonite. J. Contam. Hydrol. 27, 223–248.

Bruno J, Arcos D, Duro L, 1999. Processes and features affecting the near field chemistry. Groundwater-bentonite interaction. SKB Technical Report TR 99-29, Svensk Kärnbränslehantering AB.

Börgesson L, Sandén T, Fälth B, Åkesson M, Lindgren E, 2005. Behaviour of the buffer in KBS-3H, SKB TR-05-xx (to be published), Svensk Kärnbränslehantering AB.

Carstea D D, 1968. Formation of hydroxy-Al and -Fe interlayers in montmorillonite and vermiculite: Influence of particle size and temperature. Clay Clay Minerals 16, 231–238.

Carstea D D, Harward M E, Knox E G, 1970. Comparison of iron and aluminum hydroxy interlayers in montmorillonite and vermiculite: I. formation. Soil Sci. Soc. Amer. Proc. 34, 517–521.

Chandler N A, Kozak E T, Martin C D, 1996. Connected pathways in the EDZ and potential for flow along tunnels. Proceedings of EDZ Workshop, September 1996 Winnipeg – International Conference on Deep Disposal of Radioactive Waste.

Charlet L, Tournassat C, 2004. Fe(II)-Na(I)-Ca(II) cation exchange on montmorillonite in chloride medium; evidence for preferential clay adsorption of chloride-metal ion pairs in seawater. Geochim. Cosmochim. Acta (accepted).

Cui D, Devoy J, Scheidegger A M, Grolimund D, Spahiu K, 2003. Interaction of selenite with iron and UO2(s) under anoxic groundwater conditions. Environmental Science & Technology (submitted).

Cui D, Eriksen T E, 1996. Reduction of pertechnetate by ferrous iron in solution: infleunce of sorbed and precipitated Fe(II). Environ. Sci. Technol. 30, 2259–2262.

Cui D, Spahiu K, 2002. The reduction of U(VI) on corroded iron under anoxic conditions. Radiochim. Acta 90, 623–628.

Curti E, Wersin P, 2002. Assessment of porewater chemistry in the bentonite backfill for the Swiss SF/HLW repository. Nagra Technical Report NTB 02-09, Nagra, Wettingen, Switzerland.

David D, 2001. Analogues archéologiques et corrosion. Andra Report 2001-192, Chatenay-Malabry, France.

De Marsily G, 1986. Quantitative hydrogeology. Academic Press, New York.

Dixon D A, Miller S H, 1995. Comparison of the mineralogical composition, physical swelling and hydraulic properties of untreated sodium bentonites from Canada, the United States and Japan. AECL Report AECL-11303, Pinawa, Canada.

Dixon D A, 2000. Porewater salinity and the development of swelling pressure and bentonite-based buffer and backfill materials. POSIVA 2000-04, Posiva Oy, Helsinki, Finland.

Dong H, Fredrickson J K, Kennedy D W, Zachara J M, Kukkadapu R K, Onstott T C, 2000. Mineral transformation associated with the microbial reduction of magnetite. Chem. Geol. 169, 299–318.

Drits V A, Manceau A, 2000. A model for the mechanism of Fe3+ to Fe2+ reduction in dioctahedral smectites. Clays Clay Minerals 48, 185–195.

EC, 2001. Treatment of bentonite barriers related FEPs in integrated performance assessment (Granite). EC-Report, Project BENIPA D-3, European community FP5 – EAECTP.

Emsley S, Olsson O, Stenberg L, Alheid J-H, Falls S, 1997. ZEDEX – A study of damage and disturbance from tunnel excavation by blasting and boring. SKB Technical Report 97-30; Svensk Kärnbränslehantering AB.

Génin J-M R, Bourrié G, Trolard F, Abdelmoula M, Jafreciz A, Refait P, Maitre V, Humbert B, Herbillon A, 1998. Thermodynamic equilibria in aqueous suspensions of synthetic and natural Fe(II)-Fe(III) green rusts: Occurences of the mineral in hydromorphic soils. Environ. Sci. Technol. 32, 1058–1068.

Gerstl Z, Banin A, 1980. Fe2+–Fe3+ transformations in clay and resin ion-exchange systems. Clays Clay Minerals 28, 335–345.

Guillaume D, 2002. Etude expérimentale du système fer-smectite en présence de solution à 80°C et 300°C. PhD thesis, University Henri Poincaré, Nancy I, France.

Guillaume D, Neaman A, Cathelineau M, Mosser-Ruck R, Pfeiffert C, Abdeloula M, Dubessy J, Villéras F, Baronnet A, Michau N, 2003. Experimental synthesis of chlorite from smectite at 300°C in the presence of metallic Fe. Clay Minerals 38, 281–302.

Güven N, 1988. Smectites. In Hydrous Phyllosilicates, S.W. Bailey (ed.), Reviews in Mineralogy, Vol. 19, Mineralogical Society of America, pp. 497–559.

Habert B, 2000. Réactivité du fer dans les gels et les smectites. PhD thesis, University of Paris 6, France.

Hakami E, 1989. Water flow in single rock joints. Licentiate Thesis. Division of Rock Mechanics, Luleå University of Technology, Luleå, Sweden.

Harrington J F, Horseman S T, 2003. Gas Migration in KBS-3 Buffer Bentonite: Sensitivity of Test Parameters to Experimental Boundary Conditions, SKB Technical Report TR 03–02, Svensk Kärnbränslehantering AB.

Haveman S A, Pedersen K, Ruotsalainen P, 1998. Geomicrobial investigations of groundwater from Olkiluoto, Hästholmen, Kivetty and Romuvaraa, Finland. POSIVA 98-09, Posiva Oy, Helsinki, Finland.

Haveman S A, Larsdotter Nilsson E, Pedersen K, 2000. Regional distribution of microbes in groundwater from Hästholmen, Kivetty, Olkiluoto and Romuvaara, Finland. POSIVA 2000-16, Posiva Oy, Helsinki, Finland.

Heller-Kallai L, 1997. Reduction and reoxidation of nontronite: the data reassessed. Clays and Clay Minerals 45, 476–479.

Helmig R, 1997. Multiphase Flow and Transport Processes in the Subsurface. Springer Verlag, Berlin.

Hermansson H-P, 2004. The stability of magnetite and its significance as a passivating film in the repository environment. SKI Report 2004:07, SKI, Stockholm, Sweden.

Horseman S, Harrington J F, Sellin P, 1999. Gas migration in clay barriers. Eng. Geol. 54, 139–149.

JNC, 2000. H12: Project to establish the scientific and technical basis for HLW disposal in Japan. Supporting Report 2. Repository design and engineering technology. JNC TN1410 2000-003, Japan Nuclear Cycle Development Institute, Tokai, Japan.

Johansson E, Äikäs K, Autio J, Hagros A, Malmlund H, Rautakorpi J, Sievänen U, Wanne T, Anttila P, Raiko H, 2002. Preliminary KBS-3H layout adaptation for the Olkiluoto site: Analysis of rock factors affecting the orientation of a KBS-3H deposition hole. Posiva Working Report 2002-57, Posiva Oy, Olkiluoto, Finland.

Johnson L H, King F, 2003. Canister options for the disposal of spent fuel. Nagra Technical Report NTB 02-11, Nagra, Wettingen, Switzerland.

Karnland O, 1998. Bentonite swelling pressure in strong NaCl solutions. POSIVA 98-01, Posiva Oy, Helsinki, Finland.

King F, Ahonen L, Taxén C, Vuorinen U, Werme L, 2001. Copper corrosion under expected conditions in a deep geologic repository. SKB Technical Report TR-01-23, Stockholm, Sweden, or POSIVA 2002-01, Posiva Oy, Helsinki, Finland.

Kostka J E, Nealson K H, 1995. Dissolution and reduction of magnetite by bacteria. Environ. Sci. Technol. 29, 2535–2540.

Kostka J E, Nealson K H, Wu J, Stucki J W, 1996. Reduction of structural Fe(III) in smectite by a pure culture of the Fe-reducing bacterium Shewanella putrfaciens strain MR-1. Clays Clay Minerals.

Kostka J E, Wu J, Nealson K H, Stucki J W, 1999. The impact of structural Fe(III) reduction by bacteria on the surface chemistry of smectite clay minerals. Geochim. Cosmochim. Acta 63, 3705–3173.

Lantenois S, 2003. Réactivité fer métal/smectites en milieu hydraté à 80°C. PhD thesis, University of Orléans, France.

Lee S Y, Bondietti E A, 1983. Technetium behavior in sulfide and ferrous iron solutions.Mat. Res. Soc. Symp. Proc. 15, 315–322.

Marcos N, 2003. Bentonite-iron interactions in natural occurrences and in laboratory – the effects of the interaction on the properties of bentonite: a literature survey. Posiva Working Report 2003-55, Posiva Oy, Olkiluoto, Finland.

Marschall P, Fein E, Kull H, Lanyon W, Liedtke L, Müller-Lyda I, Shao H, 1999. Conclusions of the Tunnel Near-Field Programme. Nagra Technical Report NTB 99-07, Nagra, Wettingen, Switzerland.

Mata M P, Giorgetti G, Árkai P, Peacor D R, 2001. Comparison of evolution of trioctahedral chlorite/berthierine/smectite in coeval metabasites and metapelites from diagenetic to epizonal grades. Clays Clay Minerals 49, 318–332.

Montoto M, Rodriguez-Rey A, Matrtinez-Nistal A, Diez-sarriá I, 1999. Fractographic characterization by quantitative microscopy of the excavation disturbance caused by boring of the experimental full scale deposition holes in the Research Tunnel at Olkiluoto, Posiva Working Report 99-69, Posiva Oy, Helsinki, Finland.

Montoto M, Rodriguez-Rey A, Autio J, 2003. Microfractographic characterization of the excavation damage caused by boring of the experimental full scale deposition holes in the Research Tunnel at Olkiluoto. CLUSTER conference on "Impact of the EDZ on the performance of radioactive waste geological repositories", Luxembourgh 3–5 November 2003.

Müller-Vonmoos M, Kahr G, 1983. Mineralogische Untersuchungen von Wyoming Bentonit MX-80 und Montigel. Nagra Technical Report NTB 83-12, Nagra, Wettingen, Switzerland.

Müller-Vonmoos M, Kahr G, Bucher F, Madsen F, Mayor P-A, 1991. Untersuchungen zum Verhalten von Bentonit in Kontakt mit Magnetit und Eisen unter Endlagerbedingungen. Nagra Technical Report NTB 91-14, Nagra, Wettingen, Switzerland.

Muurinen A, Lehikoinen J, 1999. Porewater chemistry in compacted bentonite. POSIVA 99-20, Posiva Oy, Helsinki, Finland.

Myneni S C B, Tokunaga T K, Brown G E, 1997. Abiotic selenium redox transformations in the presence of Fe(II,III) oxides. Science 278, 1106–1109.

Nagra, 2002. Project Opalinus Clay: Safety report. Demonstration of disposal feasibility for spent fuel, vitrified high-level waste and long-lived intermediate-level waste (Entsorgungsnachweis). Nagra Technical Report NTB 02-05, Nagra, Wettingen, Switzerland.

Nagra, 2004. Effects of post-disposal gas generation in a repository for spent fuel, high-level waste and long-lived intermediate level waste sited in Opalinus Clay. Nagra Technical Report 04-06, Nagra, Wettingen, Switzerland.

NEA, 2000. Features, Events and Processes (FEPs) for Geologic Disposal of Radioactive Waste: An International FEP Database, OECD Nuclear Energy Agency, Paris, France.

Oscarson D W, Heimann R B, 1988. The effect of Fe(II)-silicate on selected properties of a montmorillonitic clay. Clay Minerals 23, 81–90.

Parkhurst D L, Appelo C A J, 1999. User›s guide to PHREEQC (Version 2) – A computer program for speciation, batch reaction, one-dimensional transport, and inverse geochemical calculations. U.S. Geological Survey Water-Resources Investigations Report 99-4259.

Pedersen K, 2000. Microbial processes in radioactive waste disposal. SKB Technical Report TR-00-04, Svensk Kärnbränslehantering AB.

Pitkänen P, Partamies S, Luukkonen A, 2004. Hydrogeochemical interpretation of baseline groundwater conditions at the Olkiluoto site. POSIVA 2003-07, Posiva Oy, Olkiluoto, Finland.

Posiva, 2003. Baseline conditions at Olkiluoto. POSIVA 2003-02, Posiva Oy, Olkiluoto, Finland.

Poteri A, Laitinen M, 1999. Site-to-canister scale flow and transport in Hästholmen, Kivetty, Olkiluoto and Romuvaara. POSIVA 99-15. Posiva Oy, Helsinki, Finland.

Poteri A, 2001. Estimation of the orientation for fractures at Hästholmen, Kivetty, Olkiluoto and Romuvaara. POSIVA 2001-10. Posiva Oy, Helsinki, Finland.

Puigdomenech I, Ambrosi J-P, Eisenlohr L, Lartigue J E, Banwart S A, Bateman K, Milodowski A E, West J M, Griffault L, Gustafsson E, Hama K, Yoshida H, Kotelnikova S, Pedersen K, Michaud V, Trotignon L, Rivas Perez J, Tullborg E-L, 2001. O2 depletion in granitic media. The REX project. SKB Technical Report TR-01-05, Svensk Kärnbränslehantering AB.

Pusch R, Ranhagen L, Nilsson K, 1985. Gas migration through MX-80 bentonite. Nagra Technical Report NTB 85-36, Nagra, Wettingen, Switzerland.

Pusch R, Karnland O, 1990. Preliminary report on longevity of montmorillonite clay under repository-related conditions, SKB Technical Report TR 90-44, Svensk Kärnbränslehantering AB.

Pusch, R, 1999. Mobility and survival of sulphate-reducing bacteria in compacted and fully water saturated bentonite-microstructural aspects. SKB Technical Report TR 99-30, Svensk Kärnbränslehantering AB.

Rasilainen K (ed.), 2004. Localisation of the SR-97 process report for Posiva's spent fuel repository at Olkiluoto. POSIVA 2004-05, Posiva Oy, Olkiluoto, Finland.

Rich C I, 1968. Hydroxy interlayers in expansible layer silicates. Clays Clay Minerals 16, 15–30.

Rodwell W R, Harris A W, Horseman S T, Lalieux P, Müller W, Ortiz Amaya L, Pruess K, 1999. Gas migration through Engineered and Geological Barriers for a Deep Repository for Radioactive Waste: Status Report, European Commission/Nuclear Energy Agency (OECD), European Commission Report EUR 19122EN.

Shen S, Stucki J W, Boast C W, 1992. Effects of structural iron reduction on the hydraulic conductivity of Na-smectite. Clays Clay Minerals 40, 381–386.

SKB, 1999a. SR 97 – Identification and structuring or processes. SKB Technical Report TR 99-20, Svensk Kärnbränslehantering AB.

SKB, 1999b. SR 97 – Processes in the repository evolution. SKB Technical Report TR 99-07, Svensk Kärnbränslehantering AB.

SKB, 1999c. SR 97 – Data and data uncertainties: Compilation of data and data uncertainties for radionuclide transport calculations. SKB Technical Report TR 99-09, Svensk Kärnbränslehantering AB.

SKB, 2004. Critical issues related to buffer design option 1, 2a, 2b. SKB PM Report, Svensk Kärnbränslehantering AB.

Smart N R, Blackwood D J, Werme L, 2001. The anaerobic corrosion of carbon steel and cast iron in artificial groundwaters. SKB Technical Report TR 01-22, Svensk Kärnbränslehantering AB.

Smart N R, Rance A P, Werme L O, 2004. Anaerobic corrosion of steel in bentonite. Mat. Res. Soc. Symp. Proc. 807, 441–446.

Stucki J W, Golden D C, Roth C B, 1984a. Effects of reduction and reoxidation of structural iron on the surface charge and dissolution of diochtahedral smectites. Clays Clay Minerals 32, 350–356.

Stucki J W, Low P F, Roth C B, Golden D C, 1984b. Effects of oxidation state of octahedral iron on clay swelling. Clays and Clay Minerals 32, 357–362.

Stucki J W, Wu J, Gan H, Komadel P, Banin A, 2000. Effects of iron oxidation state and organic cations on dioctahedral smectite hydration. Clays Clay Minerals 48, 290–298.

Sugihara K, Matsui H, Ishijima F, Sato T, 1996. Study on Excavation disturbance in the Kamaishi Mine. Proceedings of EDZ Workshop September 1996; Winnipeg – International Conference on Deep Geological Disposal of Radioactive Waste.

Tanai K, Kanno T, Galle C, 1997. Experimental study of gas permeabilities and breakthrough pressures in clays. Mater. Res. Soc. Symp. Proc. 465, 995–1002. Materials Research Society, Pittsburgh, PA.

Thorsager P, Lindgren E, 2004. KBS-3H Summary report of work done during Basic Design. SKB R-04-42, Svensk Kärnbränslehantering AB.

Tomeoka K, Mcsween H Y, Buseck P R, 1989. Mineralogical alteration of CM carboneceous chondrites: a review. In: Hoshiai T, ed.) Proceedings of the NIPR Symposium on Antarctic Meteorites, National Institute of Polar Research, Tokyo, 2, pp. 221–234.

Tournassat C, 2003. Cations-clays interactions: the Fe(II) case. Application to the problematic of the French deep nuclear repository field concept. PhD thesis, University of Grenoble, France, 199 p.

Tournassat C, Charlet L, Greneche J-M, 2004. Interactions of Fe2+, Zn2+ and H4SiO4 at clay/water interfaces: distinguishing competitive sorption, coadsorption and surface oxidation phenomena. Geochim. Cosmochim Acta (subm.).

Vieno T, 2000. Groundwater salinity at Olkiluoto and its effects on a spent fuel repository. POSIVA 2000-11, Posiva Oy, Helsinki, Finland.

Vieno T, Lehikoinen J, Löfman J, Nordman H, Mészáros F, 2003. Assessment of disturbances caused by construction and operation of ONKALO. POSIVA 2003-06, Posiva Oy, Olkiluoto, Finland.

Vogt K, Köster H M, 1978. Zur Mineralogie, Kristallchemie und Geochemie einiger Montmorillonite aus Bentoniten. Clay Minerals 13, 25–43.

Wanner H, Albinsson Y, Karnland O, Wieland E, Wersin P, Charlet L, 1994. The acid/base chemistry of montmorillonite. Radiochim. Acta 66/67, 157–162.

Wanner H, Wersin P, Sierro N, 1992. Thermodynamic modelling of bentonite-groundwater interaction and implications for near field chemistry in a repository for spent fuel. SKB Technical Report TR 92-37, Svensk Kärnbränslehantering AB.

Wersin P, Spahiu K, Bruno J, 1994. Time evolution of dissolved oxygen and repository conditions in a HLW repository. SKB Technical Report TR 94-02, Svensk Kärnbränslehantering AB.

Wersin P, 2003. Geochemical modelling of bentonite porewater in high-level waste repositories. J. Contam. Hydrol. 61, 405–422.

Wersin P, Johnson L H, Schwyn B, Berner U, Curti E, 2003. Redox conditions in the near field of a repository for SF/HLW and ILW in Opalinus Clay. Nagra Technical Report NTB 02-13, Nagra, Wettingen, Switzerland.

Yu J-W, Neretnieks I, 1997. Diffusion and sorption proerties of radionuclides in compacted bentonite. SKB Technical Report TR 97-12, Svensk Kärnbränslehantering AB.

Zolensky M H Y, McSween JR, 1988. Aqueous alteration. In Meteorites and the Early Solar System (eds. J.F. Kerridge and M.S. Matthews), University of Arizona Press,Tucson, pp. 114–143.

Appendix A

List of input parameters

Table A-1. Input parameter values for the HMCBG analyses presented in this report. Note that these parameter values have been approved by SROY on the 29.06.2004. Special input parameters not contained in this table can be found in the relevant chapters.

Parameter	Unit	Symbol	Reference value	Alternative values	Comment/Ref.
System description					
Repository depth					
One-storey	m		400		Appendix E
Two-storeys	m			400 and 500	Appendix E
Deposition drift					
Diameter	mm	$2\,r_t$	1,850	1,840	/Börgesson et al. 2005/
Length	mm		300		Appendix E
Separation between drifts	m	d	25	40	Appendix E
Total void space per canister	m^3		11.0 (Posiva) 10.2 (Posiva)	8.32 (SKB) 7.75 (SKB)	BWR, calculated PWR, calculated
Drift dip	°		2 ±1		Meeting 28.05.04
Drift orientation	–		Parallel to max. stress		Appendix E
Canister					
Outer diameter	m	$2\,r_c$	1.05		/Börgesson et al. 2005/
Length	m	l_c	4.83		/Börgesson et al. 2005/
Pitch (center-to-center distance)	m m	p_c	10.9 (Posiva) 10.2 (Posiva)	8.6 (SKB) 8.1 (SKB)	BWR PWR
Supercontainer (perforated)					
Total mass	kg		869		PM 28.05.04
Length	mm	l_{sc}	5,546		/Börgesson et al. 2005/
Outer diameter	mm	$2\,r_{sc}$	1,765		/Börgesson et al. 2005/
Inner diameter	mm		1,749		/Börgesson et al. 2005/
Thickness (of end plates)	mm		8		/Börgesson et al. 2005/
Radius of holes	mm		50		/Börgesson et al. 2005/
Degree of perforation	%		60		/Börgesson et al. 2005/
Distance blocks					
Diameter	mm		1,765		/Börgesson et al. 2005/
Length (depending on drift sep.)	mm		5,350 (25 m)	3,050 (40 m)	BWR (Appendix E)
			4,650 (25 m)	2,550 (40 m)	PWR (Appendix E)
Void slot (option 1)	mm		37.5–42.5		/Börgesson et al. 2005/
Pellet-filled slot (option 2a)	mm		37.5–42.5		/Börgesson et al. 2005/
Void slot (option 2b)	mm		0–5		/Börgesson et al. 2005/
Bentonite blocks					
Initial water content	w-%		10		/Börgesson et al. 2005/
Saturated density	kg m^{-3}		2,000		/Börgesson et al. 2005/
Saturated porosity	%	ε_b	44		SKB TR 99-07
Swelling pressure	MPa		7–8	8.7 in SKB TR 99-07	Meeting 28.05.04
Gap to canister (radial)	mm		5		/Börgesson et al. 2005/
Gap to super container (radial)	mm		5		/Börgesson et al. 2005/
Diameter end blocks	mm		1,735		/Börgesson et al. 2005/

Parameter	Unit	Symbol	Reference value	Alternative values	Comment/Ref.
Diameter ring blocks	mm		1,735		/Börgesson et al. 2005/
Length end blocks	mm		350		/Börgesson et al. 2005/
Length ring blocks	mm		4,830 (4*1,207.5)		Alt1-container.pdf file
Bentonite pellets					
Initial water content	w-%		10		/Börgesson et al. 2005/
Initial density	kg m^{-3}		1,000		/Börgesson et al. 2005/
Dry density	kg m^{-3}		909		/Börgesson et al. 2005/
Supporting feet (supercontainer)					
Material type	–		Steel		
Total mass (per canister)	kg		37.5		10 feet per supercontainer
Supporting feet (distance block, option 1)					
Material type	–		Steel		
Total mass (per canister)	kg		37.5		10 feet per distance block
Ring bolted to the rock (option 2a/2b)					
Material type	–		Steel		
Total mass	kg		550	1,500	Rengas1.jpg, e-mail 16.6.04/MS, e-mail 30.6.04/MS
Ring attached to container (option 2a)					
Material type	–		Steel		
Total mass	kg		100		PM 28.05.04
Geochemical and biological conditions					
Host rock chemistry					
Salinity	g l^{-1}		10–25	25–45	/Posiva 2003/; Appendix E
Alkalinity	meq l^{-1}		0.4	0.1–1	/Posiva 2003/
pH			7.5–8.2		/Posiva 2003/
Redox potential	mV		–300..–250	≈ –200	/Posiva 2003, Pitkänen et al. 2004/
Redox conditions			Methanogenic	Sulphidic	/Posiva 2003/
Degradable organic matter (n.a)	% rock		0		Meeting 28.05.04
Dissolved Fe(II)	mg l^{-1}		0.07	0–0.5	/Pitkänen et al. 2004/
Dissolved gases					
H_2	ml l^{-1}		< 0.1 generally	7–268 (a max. value below 800 m)	Not near saturation /Gascoyne 2000, Pitkänen et al. 2004/
CH_4	ml l^{-1}		< 400 generally at depths down to 500 m	770–990 (max.values below 800 m)	Near sat.in saline water < 800 m, /Gascoyne 2000, Pitkänen et al. 2004/
Solubilities at 30°C (after. approx. 2000a TR 99-07 p. 100) and 0.1 MPa					
H_2	mol m^{-3} ml l^{-1}		0.77 19		/Himmelblau 1960/
CH_4	mol m^{-3} ml l^{-1}		1.3 33		/Himmelblau 1960/

Parameter	Unit	Symbol	Reference value	Alternative values	Comment/Ref.
Bentonite					
Bentonite type			MX-80		TILA-99
Porewater composition					e.g. /Vuorinen et al. 1998/ see Table 2-2 , saline water reducing conditions.
Fe(II) mineral content (pyrite, siderite)	%		1	0	/Müller-Vonmoos 1983/
Steel corrosion rate	μm a^{-1}	*R*	1	2	/Smart et al. 2004/
				5–10	Sensitivity anal.
Rock properties					
Gneiss: fracture properties					Sparsely fractured rock and occasional "vein-like sections" (Appendix E); see also /Posiva 2003/ and note at the end of this paper.
Fracture type	–		Fractures	Vein-like	
Orientation	–		Several sets		
Density	m^{-1}	*N*	1–3	3–10	
Aperture	mm	*a*	Calc. from T-distribution		
Transmissivity	m^2 s^{-1}	*T*	10^{-14} to 10^{-7}		
Hydraulic conductivity	m s^{-1}		10^{-8} to 10^{-15}		/Börgesson et al. 2005/
Gneiss: average matrix properties					
Porosity	%	ε_m	0.14	0.1–0.2	Appendix D *
Hydraulic conductivity	m s^{-1}		1E–14	≈ < 1E–15	/Hautojärvi 2004/
Gas effective diffusion constant	m^2 s^{-1}		2.63E–10		Appendix D
Intrinsic gas permeability	m^2		5.16E–21		Appendix D
EDZ: properties of crushed zone (0–4 mm)					
Thickness (radial extent)	mm		4		Appendix D
Porosity	%		0.64	2–4	Appendix D
Fracture type	–		Open cracks		Appendix D
Mean fracture aperture	μm		2		Appendix D
Small fractures (< 5.4 μm)	%		90		Appendix D
Larger fractures (> 5.4 μm)	%		10		Appendix D
EDZ: properties of microfractured zone (4–9 mm)					
Thickness (radial extent)	mm		5		Appendix D
Porosity	%		0.34		Appendix D
Fracture type	–		Open cracks		Appendix D
Mean crack specific surface	μm^{-1}		0.004		Appendix D
Small fractures (< 2.16 μm)	%		60 %		Appendix D
EDZ: properties of zone of minor damage (9–23 mm)					
Thickness (radial extent)	mm		14		Appendix D
Fracturation	–		Similar as in undisturbed rock		Appendix D

Parameter	Unit	Symbol	Reference value	Alternative values	Comment/Ref.
EDZ: average properties (0–23 mm)					
Porosity	%	ε_{EDZ}	0.34		Appendix D
Gas effective diffusion constant	$m^2\ s^{-1}$		3.97E–9		Appendix D **
Intrinsic gas permeability	m^2		2.96E–19		Appendix D ***
Hydraulic properties					
Leakage rates for 300 m drift (operational phase)	min^{-1}				Appendix E
Long dry sections			"dry"		Suitable
Several point leakages			0.1 (each)		Suitable
A few fractures or fracture zones			1 (each)		Suitable?
Occasional fracture zone				10 (each)	Unsuitable
Total leakage			10 (total)		
Saturation time	a		10	12,000	Meeting 28.05.04
Hydraulic gradient (post-closure phase)	$m\ m^{-1}$		0.01		Appendix E
Thermal properties					
Ambient temperature	°C	T_0	+10.5°C (400 m)		/Ikonen 2003/, gradient 1.5°C/100 m
Heat output	W				Appendix E
BWR canister			1,700		
PWR canister			1,370		
Thermal conductivity (gneiss)	$Wm^{-1}\ K^{-1}$		2.7		/Posiva 2003/, p. 114
Heat capacity (gneiss)	$J\ kg^{-1}\ K^{-1}$		797		/Posiva 2003/, p. 114
Thermal diffusivity (gneiss)	$m^2\ s^{-1}$		1.23E–06		/Posiva 2003/, p. 114
Thermal conductivity (bentonite)	$Wm^{-1}\ K^{-1}$		1.0		Appendix E
Maximum temperature at canister surface (for thermal dimensioning)	°C		90		10° below the design basis max. of 100° (Appendix E)

* These values represent Gneissic tonalite in the Research Tunnel at Olkiluoto.

** Scaling factor to convert to diffusivity of heavier molecules in water saturated samples by 1/35,000 /Autio et al. 1999/.

*** Hydraulic conductivity can be calculated using permeability /e.g. Autio et al. 1999/.

References for Table A-1:

Appendix D

Autio J, 2004. Description of excavation damaged zone (EDZ) around a KBS-3H deposition drift, PM KBS-3H Safety case 10/2004, Saanio & Riekkola Oy, Helsinki, Finland.

Autio J, Kirkkomäki T, Siitari-Kauppi M, Timonen J, Laajalahti M, Aaltonen T, Maaranen J, 1999. Use of 14C-PMMA method and He-gas methods to characterize excavation disturbance in crystalline rock. Posiva report 99-22, Posiva Oy, Helsinki, Finland.

Börgesson L, Sandén T, Fälth B, Åkesson M, Lindgren E, 2005. Behaviour of the buffer in KBS-3H, SKB TR-05-xx (to be published); Svensk Kärnbränslehantering AB.

Gascoyne, M, 2000. Dissolved gases in groundwaters at Olkiluoto, Posiva Working report 2000-49, Posiva Oy, Helsinki, Finland.

Hautojärvi, 2004. interview by Ari Ikonen, June 15, 2004.

Himmelblau D M, 1960. Solubilities of inert gases in water. J. Chem. Eng., Vol. 5/1, January 1960.

Ikonen K, 2003. Thermal Analyses of KBS-3H Type repository, Posiva 2003-11, Posiva Oy, Eurajoki, Finland.

Müller-Vonmoos M, 1983. Nagra Technical Report NTB 83-12.

Pitkänen P, Partamies S, Luukkonen A, 2004. Hydrogeochemical interpretation of baseline groundwater conditions at the Olkiluoto site. Posiva 2003-07, Posiva Oy, Eurajoki, Finland.

Posiva, 2003. Baseline conditions at Olkiluoto. Posiva Report 2003-02, Posiva Oy, Eurajoki, Finland.

Poteri A, Laitinen M, 1999. Site-to-canister scale flow and transport in Hästholmen, Kivetty, Olkiluoto and Romuvaara. Posiva 99-15. Posiva, Helsinki Finland.

Poteri A, 2001. Estimation of the orientation for fractures at Hästholmen, Kivetty, Olkiluoto and Romuvaara. Posiva 2001-10. Posiva Oy, Helsinki, Finland.

Smart N R, Rance A P, Werme L O, 2004. Anaerobic corrosion of steel in bentonite. Mat. Res. Soc. Symp. Proc. 807, 441–446.

Appendix E

Vieno T, 2004. Olkiluoto site data for KBS-3H design and analysis. PM KBS-3H Safety case 9/2004, Saanio & Riekkola Oy, Helsinki, Finland.

Vuorinen U, Kulmala S, Hakanen M, Ahonen L, Carlsson T, 1998. Solubility database for TILA –99. Posiva report 98-14, Posiva Oy, Helsinki, Finland.

Appendix B

Description of diagonal elements and list of identified interactions for KBS-3H

In this appendix, a full description of the diagonal elements presented in Table 3-1 and a list of identified interactions is given. The basis for this description is Appendix A in /SKB 1999/, with the following modifications:

- the diagonal element 'Backfill' (tunnel backfill in KBS-3V concept) is eliminated, because it is not relevant for KBS-3H concept,
- two diagonal elements are added at the end, namely 'Supercontainer' and 'Distance block'.

In addition, the list of identified interactions has been changed in comparison with Appendix A in /SKB 1999/ for a number of reasons, including design changes and the focus on gas-related issues. The updated list of interactions is given in Table B-1, with an indication which interactions are specific to the KBS-3H design or which ones have been changed in comparison with /SKB 1999/.

Diagonal elements of interaction matrix for KBS-3H

1.1 Fuel

Spent fuel and metal components of the fuel, such as zircaloy cladding, fuel boxes, spacers, springs, grids etc of stainless steel and inconel in the canister.

The constituents are enclosed in the canister and assumed to be retained in it. Hence, no direct interaction with other repository components are considered, but radiation and gas emanating from the fuel are taken into account.

Interaction is primarily through radiation, which affects mainly the canister (1.2), buffer smectite and non-smectite minerals/impurities (1.3, 1.5), buffer porewater (1.4) and groundwater chemistry (1.9). A second type of interaction is through heat production affecting the temperature conditions in the entire system (1.7).

2.2 Canister

Copper-iron canister with an inner steel supercontainer in which the fuel is located. Both canister components are assumed to be intact except when gas generation is considered. Gamma radiation penetrating the canister is taken into account.

Interaction is with fuel (2.1), buffer (smectite and non-smectite/impurities, 2.3 and 2.5), buffer porewater (2.4), gas (contribution by corrosion, 2.6), temperature (heat transfer to surroundings, 2.7), and groundwater hydrology (geometrical restraint, 2.8).

3.3 Smectite/buffer

Composition

The buffer consists of smectite-rich clay (bentonite) and accessory minerals and impurities, like non-smectite clay minerals (kaolinite, illite, chlorite) and rock-forming minerals (silicates, oxides, carbonates, sulphates and sulphides).

Conditions

The buffer is prepared in block form by compressing clay powder that may be purely natural (MX-80 Na smectite-rich bentonite) or soda-treated to Na form. The dry density of the buffer is in the interval 1,500–2,000 kg m^{-3}. The initial degree of water saturation is 45–85 % depending on the processing.

Properties

Buffer emplaced in the supercontainer absorbs water from the surroundings and ultimately becomes fully water saturated. In the saturation phase a number of processes take place that influence the performance both in early stages and long afterwards. After complete water saturation the buffer is characterized by a very low hydraulic conductivity and an ability to expand through the holes in the supercontainer and exert a pressure on the surroundings that depends on the density and porewater chemistry and that can be several MPa. The transport properties, like the hydraulic and gas conductivities, ion diffusivity and colloid filtration, are largely controlled by the microstructure, which is affected by the density of the buffer and the chemical composition of the porewater. Malfunctions may occur, for example, in emplacing of bentonite blocks within the supercontainer.

Buffer in present context

In referring to physical and mechanical interactions the buffer material (3.3) is regarded as a whole, i.e. including porewater (4.4) and non-smectite minerals/impurities (5.5), but when chemical processes are referred to, only the smectite component is taken into account. Interaction is primarily with canister through pressurization (3.2) and chemical interaction (3.4) and through temperature effects (3.7). The buffer provides some gas storage and transport capacity (3.6). By its swelling capacity, the buffer may breach the supercontainer (3.12), displace the distance block (3.13) and self-seal the EDZ (3.8, 3.10). The buffer acts as a colloid filter (3.5) and coupled transport phenomena may occur (3.4).

4.4 Buffer porewater

Water in the buffer that is in contact with the canister, smectite minerals, other clay minerals, non-clay minerals and impurities (colloids and organics). It contains ions and occupies three sorts of voids: The interlamellar space within the stacks of smectite flakes (“pseudo-crystalline”, organized water), water in the double-layer zone surrounding the stacks, and free water in voids larger than about 20 Å. The latter is termed “external”, while the first mentioned type of porewater is called “internal”.

Interaction is primarily with buffer minerals through chemical effects (4.2, 4.3, 4.5) and with the buffer as a whole through setting up pressures (swelling pressure and water/gas pressure, 4.2, 4.6, 4.8, 4.10, 4.12, 4.13) in it and by percolating it (4.3, 4.9). Temperature is interacting both with respect to chemical and physical effects (4.7).

5.5 Non-smectite minerals/impurities

Non-smectite clay minerals, such as illite, chlorite and kaolinite, non-clay silicate mineral such as quartz, feldspars, micas and heavy minerals, and non-silicate rock-forming minerals like carbonates, primarily calcite, oxides, hydroxides, phosphates, sulphates and sulphides. Also, stray materials, potential contaminations, colloids and organics belong to this group.

Interaction is primarily with the buffer porewater through chemical effects like dissolution/precipitation (5.4), corrosion/degradation (5.2, 5.3, 5.12, 5.13), aided by temperature (5.7).

6.6 Gas

All gaseous phases in the buffer (not inside the canister), distance block and near-field rock, such as trapped air and gases produced by corrosion (like hydrogen) and radiolysis (like oxygen), but excluding dissolved gas. The main gas source is the steel contained in the deposition tunnels (supercontainer, rings, feet). Some of the interactions identified are only relevant for a corroding canister, i.e. assuming that water can penetrate the copper shield of the canister. Type, composition and amount of gas (at NPT), actual gas volume, gas pressure, critical gas pressure, gas flow, thermal properties of gas.

Interaction is primarily with the buffer and distance block through gas piping and erosion effects (6.3, 6.13). At early times, gas is dissolved in the porewater and gas diffusion/advection takes place (6.4, 6.9), followed by the creation of a gas phase, gas pressure build-up and gas-induced water displacement, affecting all system components in the near field (6.2, 6.4, 6.8, 6.10-13). Indirect interaction is with the near-field by storage of gas in the near-field rock and thereby affecting the groundwater hydrology (6.8) and the properties of the near field rock (6.10).

7.7 Temperature

Absolute temperature (Celcius or Kelvin), temperature evolution, temperature gradient, all expressed as functions of time after deposition of canisters in the drift. Temperature data for canisters, buffer, supercontainer and near-field rock.

Interaction is primarily with the buffer through heating it, creating a temperature gradient across it and changing the kinetics of chemical reactions. This affects chemical processes like alteration of smectite (7.3, 7.13) and other minerals (7.5) and physical properties like the hydraulic conductivity (7.3), thermal expansion (7.2, 7.6, 7.8, 7.10-12).

Other interactions of importance are with the groundwater hydrology (7.8) and the structure and performance of the near-field rock and supercontainer (7.10,12).

8.8 Groundwater hydrology

Pressure, flow and properties of water contained in the near-field rock. Density, viscosity, thermal properties and compressibility.

Interaction is of physical character, primarily with the buffer and distance block by affecting their saturation with water and exposure to piping/erosion (8.3, 8.5, 8.13) and by affecting its transport properties (8.4, 8.6, 8.7), and with the near-field rock through erosion (8.10).

9.9 Groundwater chemistry

Composition and properties of groundwater in the near-field rock in terms of the content and composition of dissolved species, colloids and microbes. The water in the rock ranges from strongly held capillary water in very fine voids and fissures to free water that moves under very low hydraulic gradients in channels in fractures. The chemical composition of the latter is controlled by the source while that in small voids is determined by its interaction with the confining minerals.

Interaction is primarily with the porewater in the buffer and in the distance block through (9.4, 9.13) and with the near-field rock through (9.10), reinforcements (9.11) and supercontainer (9.12). Other relevant effects are gas dissolution (9.6) and viscosity/density changes (9.7. 9.8).

10.10 Near-field rock

Structure, stress conditions, geometry and properties of the rock surrounding the deposition tunnels to a distance influenced by excavation. A most important feature of the rock as concerns interaction with buffer is the hydrology, which depends on the rock structure, and piezometric conditions. Also, its stability is of significance since it determines the behavior of the rock around deposition tunnels in the waste application phase as well as in a long-term perspective, i.e. when tectonics and glaciation are expected to play a role.

Physical interaction is primarily with the buffer, the distance block and supercontainer through establishment of pressures (10.3, 10.12, 10.13) and groundwater hydrology by being exposed to water pressure (10.8) and erosion (8.10). The major chemical interaction takes place indirectly with the buffer through groundwater chemistry (10.9) and buffer porewater (10.3, 10.13). The near-field rock provides storage and transport capacity for gas (10.6) and heat (10.7).

11.11 Reinforcements

Construction materials, like concrete, cement and bentonite pellets, cement paste, steel reinforcement (rings, bars, bolts, supports), and asphalt. They are in contact with water contained in the near-field rock.

With the exception of steel rings, the reinforcements are not planned to be in operation for more than the construction and waste application and backfilling phases. Their longevity is not a major factor with the possible exception of grouts injected in fractures intersecting deposition holes.

Physical interaction is primarily with the distance block (11.13) and near-field rock through establishment of contact pressures (11.10). Chemical interaction takes place indirectly through the groundwater with the near-field rock (11.8, 11.9) and with bentonite (11.4, 11.13). Gas is produced by steel corrosion (11.6).

12.12 Supercontainer

A steel supercontainer is used that surrounds the canister and the buffer to facilitate emplacement. The supercontainer is perforated (60% holes), allowing for swelling of bentonite through the holes into the voids outside the supercontainer. The mechanical strength of the supercontainer is designed to withstand stresses during transport and emplacement. After closure, no safety function related to isolation or mechanical stability is attributed to the supercontainer.

Physical interactions are primarily with the buffer and the distance block through hindrance to swelling (12.3, 12.13). Chemical reactions are related to volume expansion (12.3, 12.5, 12.10–11, 12.13) and gas production during corrosion (12.6), iron/smectite interaction (12.3, 12.13) and iron-silicate formation (12.5). Heat transport is hindered by radiation through gap between supercontainer and near-field rock (12.7)

13.13 Distance block

Distance block (bentonite blocks) are emplaced between supercontainers to seal off individual canisters and to prevent preferential transport pathways along the axis of the deposition drift. The voids between distance block and granite rock may be filled with bentonite pellets, held in position by steel rings. During resaturation, water inflow from the granite rock and gas flow may cause piping and erosion of the distance block. This may affect the swelling capacity and thus long-term performance. Malfunctions may occur, for example, in poorly emplacing the distance block.

Note that the FEPs for the bentonite buffer and the distance are similar (same material). In contrast to the bentonite buffer, however, only one diagonal element is foreseen for the distance block. For this element, only those FEPs specific to the distance block are listed, bearing in mind that all other FEPs relevant for the bentonite buffer (elements 3.3, 4.4 and 5.5) also apply.

Of primordial importance is the swelling capacity of distance block, affecting the supercontainer/buffer (13.3, 13.12), near-field rock (13.10), reinforcements (13.11), groundwater flow (13.8) and gas flow (13.6). Chemical interaction may take place with the buffer (13.3, 13.4, 13.5). Preferential water/gas piping and erosion at the interface to the granite rock may occur (3.13, 6.13).

List of identified interactions for KBS-3H

Table B-1. List of identified interactions with priorities: Comparison between /SKB 1999/ and KBS-3H concept.

No.	Element name and priority /SKB 1999/		Element name for KBS-3H (this report)
1.2	Fuel on canister (by radiation)	2 = Yellow	id.
1.3	Fuel on buffer smectite (by radiation)	1 = Green	id.
1.4	Fuel on buffer porewater (by radiolysis)	1 = Green	id.
1.5	Fuel on buffer non-smectite minerals/ impurities in buffer (by radiation)	1 = Green	id.
1.6	Fuel on near-field gas (by radiation)	4 = Pink	id., 2 = Yellow
1.7	Fuel on near-field temperature (by radioactive decay)	3 = Red	id.
1.9	Fuel on groundwater chemistry in near-field	1 = Green	id.
1.10	Fuel on near-field rock (by radiation)	1 = Green	id.
1.11	Fuel on reinforcements (by radiation)	1 = Green	id.
1.12			Fuel on supercontainer (by radiation), 1 = Green
1.13			Fuel on distance block (id. to 1.3/1.4/1.5), 1 = Green
2.1	Canister on fuel (by affecting confinement through changes in physical state)	3 = Red	id.
2.3a	Canister on buffer (by affecting the density through pressurizing)	1 = Green	id.
2.3b	Canister on buffer (by affecting the density through thermally induced geometrical changes)	1 = Green	id.
2.4	Canister on buffer porewater (by ion release)	2 = Yellow	id.
2.6	Canister on near-field gas (by corrosion)	3 = Red	Canister on near-field gas (gas production by corrosion), 3 = Red
2.7	Canister on near-field temperature (by transfer of heat from fuel)	1 = Green	id.
2.8	Canister on groundwater hydrology (geo-metrical restraint)	1 = Green	id.
3.2a	Buffer on canister (by affecting its position through swelling pressure anomalies)	3 = Red	id.
3.2b	Buffer on canister (by affecting its shape through swelling pressure)	3 = Red	id.
3.2c	Buffer on canister (by affecting position and shape through shearing)	3 = Red	id.
3.4a	Buffer on buffer porewater (by ion diffusion)	3 = Red	id.
3.4b	Buffer on buffer porewater (by affecting its physical state)	3 = Red	id.
3.4c	Buffer on buffer porewater (by dissolution of smectite)	3 = Red	id.
3.4d	Buffer on buffer porewater (by ion exchange)	1 = Green	id.
3.4e	Buffer on buffer porewater (by producing colloids)	3 = Red	id.
3.4f	Buffer on buffer porewater (by sorption)	1 = Green	id.
3.4g	Buffer on buffer porewater (by flow)	1 = Green	Buffer on buffer porewater (by coupled transport processes), 1 = Green

No.	Element name and priority /SKB 1999/		Element name for KBS-3H (this report)
3.4h	Buffer on buffer porewater (by affecting the pressure state)	4 = Pink	id.
3.5	Buffer on buffer non-smectite minerals/ impurities (by affecting their positions)	1 = Green	id.
3.6a	Buffer on buffer gas (by capacity of storing gas)	3 = Red	id.
3.6b	Buffer on buffer gas pressure (by release of gas)	3 = Red	id.
3.6c	Buffer on buffer gas (by gas conductivity)	3 = Red	id.
3.7a	Buffer on buffer temperature (by heat flow)	3 = Red	id.
3.7b	Buffer on buffer temperature (by heat of wetting)	1 = Green	id.
3.8	Buffer on groundwater hydrology (by affecting flow in near-field rock)	3 = Red	id.
3.10a	Buffer on near-field rock (by affecting the stability through swelling pressure)	3 = Red	id.
3.10b	Buffer on near-field rock (by affecting fracture aperture through swelling pressure)	3 = Red	id.
3.10c	Buffer on near-field rock (by self-sealing)	3 = Red	id.
3.11a	Buffer on reinforcements (by destruction of cement grout in fractures in deposition holes)	1 = Green	id. (deposition drifts, not holes)
3.11b	Buffer on reinforcements (by consolidation of bentonite grout in fractures in depostion holes)	1 = Green	id. (deposition drifts, not holes)
3.12a			Buffer on supercontainer (by swelling pressure), 3 = Red
3.12b			Buffer on supercontainer (by breaching), 3 = Red
3.13			Buffer on distance block (as in 3.4/3.5 + by swelling pressure + by displacement of distance block), 3 = Red
4.2a	Buffer porewater on canister (by corrosion)	3 = Red	id.
4.2b	Buffer porewater on canister (by pressurizing canister)	3 = Red	id.
4.3a	Buffer porewater on buffer (by producing swelling pressure and expandability)	3 = Red	id.
4.3b	Buffer porewater on buffer (by dissolution of the smectite content)	3 = Red	id.
4.3c	Buffer porewater on buffer smectite (by formation of smectite)	1 = Green	id.
4.3d	Buffer porewater on buffer smectite (by ion-exchange)	3 = Red	id.
4.3e	Buffer porewater on buffer smectite (by degrading and alterating it)	3 = Red	id.
4.3f	uffer porewater on buffer (by affecting the microstructural homogeneity)	3 = Red	id.
4.5a	Buffer porewater on buffer non-smectite minerals/impurities (by dissolution)	3 = Red	id.
4.5b	Buffer porewater on buffer non-smectite minerals/impurities (by precipitation)	3 = Red	id.
4.6a	Buffer porewater on buffer gas (by vapor pressure)	4 = Pink	id., 2 = Yellow

No.	Element name and priority /SKB 1999/		Element name for KBS-3H (this report)
4.6b	Buffer porewater on buffer gas (by dissolution of gas in porewater)	3 = Red	id.
4.6c	Buffer porewater on buffer gas (by affecting the mobility of gas)	4 = Pink	id., 3 = Red
4.6d	Buffer porewater on buffer gas (by affecting the pressure for release of gas)	4 = Pink	id., 3 = Red
4.6e	Buffer porewater on buffer gas (by microbial activity)	1 = Green	id.
4.7a	Buffer porewater on buffer temperature (by heat conductivity)	1 = Green	id.
4.7b	Buffer porewater on buffer temperature (by heat of wetting)	1 = Green	id.
4.8	Buffer porewater on groundwater hydrology (by exerting pressure)	4 = Pink	id.
4.9	Buffer porewater on groundwater chemistry (by supplying or extracting dissolved species)	3 = Red	id.
4.10	Buffer porewater on near-field rock (by exerting pressure on the rock)	1 = Green	id.
4.12a			Buffer porewater on supercontainer (by corrosion), 3 = Red
4.12b			Buffer porewater on supercontainer (by pressurizing supercontainer), 1 = Green
4.13			Buffer porewater on distance block (id. to 4.3/4.5), 1 = Green
5.2	Buffer non-smectite minerals/impurities on canister (by corroding contacting canister)	1 = Green	id.
5.3	Buffer non-smectite mineral/impurities on buffer smectite (by degrading contacting smectite)	1 = Green	id.
5.4a	Buffer non-smectite minerals/impurities on buffer porewater (by being dissolved)	3 = Red	id.
5.4b	Buffer non-smectite minerals/impurities on buffer porewater (by being precipitated)	3 = Red	id.
5.4c	Buffer non/smectite minerals/impurities on buffer porewater (by forming colloids)	1 = Green	id.
5.7	Buffer non-smect. min./impurities on buffer/canister temperature (by affect. heat conductivity)	1 = Green	id.
5.12			Buffer non-smectite minerals/impurities on supercontainer (by corroding contacting supercontainer), 1 = Green
5.13			Buffer non-smectite minerals/impurities on distance block (id. to 5.4), 1 = Green
6.2a	Buffer gas on canister (by pressurization)	1 = Green	id.
6.2b	Buffer gas on canister (by corrosion)	2 = Yellow	id.
6.3a	Buffer gas on buffer (by piping)	3 = Red	id.
6.3b	Buffer gas on buffer (by affecting its homogeneity, i.e. through forming flow paths)	2 = Yellow	id.
6.3c	Buffer gas on buffer (by affecting the hydration state)	2 = Yellow	id.
6.4a	Buffer gas on buffer porewater (by being dissolved)	1 = Green	id.
6.4b	Buffer gas on buffer porewater (by pressurizing)	1 = Green	id.

No.	Element name and priority /SKB 1999/		Element name for KBS-3H (this report)
6.4c			Buffer gas on buffer porewater (by displacement of porewater), 1 = Green
6.4d			Buffer gas on buffer porewater (by being diffused/advected in porewater), 1 = Green
6.5	Buffer gas on buffer non-smectite minerals/impurities (by chemical reactions)	1 = Green	0 = White
6.7	Buffer gas on buffer/canister temperature (by thermal isolation)	4 = Pink	id.
6.8a	Gas in near-field rock on groundwater hydrology (by affecting the flow paths)	2 = Yellow	id.
6.8b			Gas in near-field rock on groundwater hydrology (by displacing porewater), 2 = Yellow
6.9a	Gas in near-field rock on groundwater chemistry (by being dissolved)	3 = Red	id.
6.9b			Buffer gas on groundwater chemistry (by being diffused/advected in groundwater), 3 = Red
6.10a	Gas in near-field rock on near-field rock (by affecting the degree of water saturation)	3 = Red	id.
6.10b	Gas in near-field rock on near-field rock (by reaction with fracture minerals)	2 = Yellow	id.
6.10c			Gas in near-field rock on near-field rock (by displacing porewater), 3 = Red
6.11	Gas in near-field rock and backfill on reinforcements (by pressurizing)	1 = Green	id. (but no backfill)
6.12			Gas in near field on supercontainer (by pressurizing), 1 = Green
6.13			Gas in near field on distance block (as in 6.3/6.4/6.5 + Piping and erosion at interface to near-field rock), 3 = Red
7.1	Temperature of fuel on fuel (by causing structural alteration)	1 = Green	id.
7.2a	Temperature of canister on canister (by changing its size and shape)	1 = Green	id.
7.2b	Temperature of canister on canister (by affecting its material structure)	1 = Green	id.
7.2c	Temperature of canister on canister (by internal pressurizing)	1 = Green	id.
7.3a	Temperature of buffer on buffer (by affecting the hydraulic conductivity)	1 = Green	id.
7.3b	Temperature of buffer on buffer (by affecting its thermal properties)	1 = Green	id.
7.3c	Temperature of buffer on buffer (by affecting its swelling pressure)	2 = Yellow	id.
7.3d	Buffer temperature on buffer (by affecting its total pressure)	2 = Yellow	id.
7.3e	Temperature of buffer on buffer (by affecting its shear strength)	2 = Yellow	id.
7.3f	Temperature of buffer on buffer smectite (by affecting chemical equilibria)	3 = Red	id.
7.3g	Temperature of buffer on buffer (by affecting the rate of alteration of the smectite)	3 = Red	id.
7.4a	Temperature of buffer on buffer porewater (by redistribution)	4 = Pink	id.

No.	Element name and priority /SKB 1999/		Element name for KBS-3H (this report)
7.4b	Temperature of buffer on buffer porewater (by affecting the viscosity)	3 = Red	id.
7.4c	Temperature of buffer on buffer porewater (by affecting the rate of chemical reactions)	3 = Red	id.
7.4d	Temperature of buffer on buffer porewater (by determining the state of chemical equilibrium)	1 = Green	id.
7.4e	Temperature of buffer temperature on buffer porewater (by affecting ion mobility)	1 = Green	id.
7.4f	Temperature of buffer on buffer porewater (by affecting its pressure)	3 = Red	id.
7.5a	Temperature of buffer on buffer non-smectite minerals/impurities (by affect. chemical equilibria)	3 = Red	id.
7.5b	Temperature of buffer on buffer non-smectite miner./impurities (by affecting the rate of change)	1 = Green	id.
7.6a	Temperature of buffer on buffer gas (by affecting its pressure)	2 = Yellow	id.
7.6b	Temperature on buffer gas (by vapor transport)	4 = Pink	id.
7.6c	Temperature of buffer on buffer gas (by affecting gas solubility)	4 = Pink	id., 2 = Yellow
7.8a	Temperature of near-field on groundwater hydrology (by groundwater convection)	2 = Yellow	id.
7.8b	Temperature of near-field on groundwater hydrology (by affecting the viscosity)	1 = Green	id.
7.9a	Temperature of near-field on groundwater chemistry (by affecting chemical equilibria)	1 = Green	id.
7.9b	Temperature of near-field on groundwater chemistry (by affecting the rate of chem. changes)	1 = Green	id.
7.10a	Temperature of near-field on near-field rock (by affecting the structure)	2 = Yellow	id.
7.10b	Temperature of near-field on near-field rock (by affecting the mechanical stability)	2 = Yellow	id.
7.10c	Temperature of near-field on near-field rock (by affecting the rate of chemical changes)	2 = Yellow	id.
7.10d	Temperature of near-field on near-field rock (by affecting chemical equlibria)	2 = Yellow	id.
7.11a	Temperature of near-field on reinforcements (by affecting their physical performance)	1 = Green	id.
7.11b	Temperature of near-field on reinforcements (by affecting chemical equilibria)	1 = Green	id.
7.11c	Temperature of near-field on reinforcements (by affecting the rate of chemical changes)	1 = Green	id.
7.12a			Temperature of near-field on supercontainer (by changing its size and shape), 1 = Green
7.12b			Temperature of near-field on supercontainer (by affecting its material structure), 1 = Green
7.12c			Temperature of near-field on supercontainer (by pressurizing), 1 = Green

No.	Element name and priority /SKB 1999/		Element name for KBS-3H (this report)
7.13			Temperature of near-field on distance block (id. to 7.3/7.4/7.5), 3 = Red
8.3a	Groundwater hydrology on buffer smectite (by eroding smectite that has entered fractures)	2 = Yellow	Groundwater hydrology on buffer smectite (by piping and eroding smectite at the bentonite/near-field rock interface), 3 = Red
8.3b	Groundwater hydrology on buffer (by providing water for saturation)	4 = Pink	id.
8.3c	Groundwater hydrology on buffer (by affecting pressure heads and hence conditions for saturat.)	4 = Pink	id.
8.4	Groundwater hydrology on buffer porewater (by affecting its chemical composition)	1 = Green	id.
8.5a	Groundwater hydrology on buffer non-smectite minerals/impurities (by erosion of buffer)	1 = Green	Groundwater hydrology on buffer non-smectite minerals/impurities (by piping and eroding smectite at the bentonite/near-field rock interface), 3 = Red
8.5b			Groundwater hydrology on buffer non-smectite minerals/impurities (by providing water for saturation), 4 = Pink
8.5c			Groundwater hydrology on buffer non-smectite minerals/impurities (by affecting pressure heads and hence conditions for saturation), 4 = Pink
8.6a	Groundwater hydrology on near-field gas (by aff. water pressure in the near-field rock and backfill)	4 = Pink	id. (no backfill), 2 = Yellow
8.6b	Groundwater hydrology on near-field gas (by affect. gas migration in near-field rock and backfill)	2 = Yellow	id. (no backfill)
8.7	Groundwater hydrology on near-field temperature (by heat transport through convection)	1 = Green	id.
8.9a	Groundwater hydrology on groundwater chemistry (by introducing water with diff. composition)	4 = Pink	id.
8.9b	Groundwater hydrology on groundwater chemistry (by mixing and dilution)	3 = Red	id.
8.10a	Groundwater hydrology on near-field rock (by erosion)	1 = Green	id.
8.10b	Groundwater hydrology on near-field rock (by particle transport)	2 = Yellow	id.
8.11a	Groundwater hydrology on reinforcements (by erosion)	1 = Green	id.
8.11b	Groundwater hydrology on reinforcements (by pressurizing)	1 = Green	id.
8.12			Groundwater hydrology on supercontainer (by pressurizing supercontainer), 1 = Green
8.13			Groundwater hydrology on distance block (as in 8.3/8.4/8.5 + piping and erosion at the interface to the near-field rock), 3 = Red
9.4	Groundwater chemistry on buffer porewater (by affecting its chemical composition)	3 = Red	id.
9.6	Groundwater chemistry on near-field gas (by affecting its solubility)	3 = Red	id.
9.7	Groundwater chemistry on near-field temp. (by affecting the heat conductivity of near-field water)	1 = Green	id.

No.	Element name and priority /SKB 1999/		Element name for KBS-3H (this report)
9.8a	Groundwater chemistry on groundwater hydrology (by buoyancy effects)	1 = Green	id.
9.8b	Groundwater chemistry on groundwater hydrology (by affecting water viscosity)	1 = Green	id.
9.10	Groundwater chemistry on near-field rock (by affecting chemical equilibria)	3 = Red	id.
9.11a	Groundwater chemistry on reinforcements (by affecting chemical equilibria)	2 = Yellow	id.
9.11b	Groundwater chemistry on reinforcements (by cement maturation and gain in strength)	2 = Yellow	id.
9.12			Groundwater chemistry on supercontainer (by corrosion), 3 = Red
9.13			Groundwater chemistry on distance block (id. to 9.4), 3 = Red
10.3a	Near-field rock on buffer (by affecting confining function)	3 = Red	id.
10.3b	Near-field rock on buffer (by imposing shear strain)	3 = Red	id.
10.3c	Near-field rock on buffer (by reducing its density through loss of buffer into fractures)	1 = Green	id.
10.3d	Near-field rock on buffer (by aff. its homogeneity through changes of the depos. hole geometry)	3 = Red	id. (deposition drift, not hole)
10.3e	Near-field rock on buffer (by aff. its density through time-dep. convergence of the dep. holes)	2 = Yellow	id. (deposition drift, not hole)
10.4	Near-field rock on buffer porewater (by influence of earth currents)	1 = Green	id.
10.6a	Near-field rock on near-field gas (by controlling the release of gas)	3 = Red	id.
10.6b	Near-field rock on near-field gas (by storing gas)	2 = Yellow	id.
10.7	Near-field rock on near-field temperature (by aff. heat transport through its thermal conductivity)	4 = Pink	id.
10.8	Near-field rock on groundwater hydrology (by its structural constitution)	3 = Red	id.
10.9a	Near-field rock on groundwater chemistry (by affecting chemical equilibria)	3 = Red	id.
10.9b	Near-field rock on groundwater chemistry (by influence of earth currents)	1 = Green	id.
10.9c	Near-field rock on groundwater chemistry (by colloid transport)	4 = Pink	id.
10.9d	Near-field rock on groundwater chemistry (by sorption of ions)	1 = Green	id.
10.9e	Near-field rock on groundwater chemistry (by matrix diffusion)	1 = Green	id.
10.11	Neafield rock on reinforcements (by imposing stress/strain)	2 = Yellow	id.
10.12			Near-field rock on supercontainer (by imposing stress/strain), 2 = Yellow
10.13			Near-field rock on distance block (id. to 10.3/10.4), 3 = Red
11.2	Reinforcements on canister (by being lost in deposition holes)	1 = Green	0 = White

No.	Element name and priority /SKB 1999/		Element name for KBS-3H (this report)
11.3	Reinforcements on buffer (by providing confinement)	1 = Green	id.
11.4			Reinforcements on buffer porewater (by alteration by cement), 1 = Green
11.6a	Reinforcements on near-field gas (by producing gas)	1 = Green	id., 2 = Yellow
11.6b	Reinforcement on near-field gas (by storing gas)	1 = Green	id., 2 = Yellow
11.7	Reinforcements on near-field temperature (by heat transport)	1 = Green	id.
11.8	Reinforcements on groundwater hydrology (by being permeable and affect. flow in near-field rock)	3 = Red	id.
11.9	Reinforcements on groundwater chemistry (by dissol. and influence on chemical equilibria)	3 = Red	id.
11.10	Reinforcements on near-field rock (by affecting its stability)	1 = Green	id.
11.13			Reinforcements on distance block (id. to 11.3/11.4), 1 = Green
12.3a			Supercontainer on smectite buffer (by hindrance to swelling through holes), 3 = Red
12.3b			Supercontainer on smectite buffer (by mechanical expansion due to corrosion), 3 = Red
12.3c			Supercontainer on smectite buffer (by Fe/ smectite interaction), 3 = Red
12.4			Supercontainer on buffer porewater (by ion release, including iron), 1 = Green
12.5a			Supercontainer on buffer non-smectite minerals/impurities (by mechanical expansion due to corrosion), 1 = Green
12.5b			Supercontainer on buffer non-smectite minerals/impurities (by Fe-silicate formation), 1 = Green
12.6			Supercontainer on near-field gas (by gas generation), 3 = Red
12.7a			Supercontainer on near-field temperature (by heat transport), 1 = Green
12.7b			Supercontainer on near-field temperature (by radiation across gaps), 1 = Green
12.8			Supercontainer on groundwater hydrology (by affecting flow paths around periphery of the drift), 1 = Green
12.10			Supercontainer on near-field rock (by mechanical expansion due to corrosion), 1 = Green
12.11			Supercontainer on reinforcements (by mechanical expansion due to corrosion), 1 = Green
12.13			Supercontainer on distance block (id. to 12.3/12.4/12.5), 3 = Red
13.3			Distance block on smectite buffer (as in 4.3/5.3 + by displacement of distance block), 3 = Red
13.4			Distance block on buffer porewater (id. to 3.4/5.4), 1 = Green

No.	Element name and priority /SKB 1999/	Element name for KBS-3H (this report)
13.5		Distance block on buffer non-smectite minerals/impurities (id. to 3.5/4.5), 1 = Green
13.6		Distance block on near-field gas (as in 3.6/4.6 + cut-off of gas pathways along drift by distance block), 3 = Red
13.7		Distance block on temperature (id. to 3.7/4.7/5.7), 3 = Red
13.8		Distance block on groundwater hydrology (id. to 3.8/4.8), 3 = Red
13.9		Distance block on groundwater chemistry (id. to 4.9), 3 = Red
13.10		Distance block on near-field rock (id. to 3.10/4.10), 3 = Red
13.11		Distance block on reinforcements (id. to 3.11), 1 = Green
13.12		Distance block on supercontainer (as in 3.12/4.12/5.12 + breaching of end plates of supercontainer), 3 = Red

Reference

SKB, 1999. SR 97 – Identification and structuring or processes. SKB Technical Report TR 99-20, Svensk Kärnbränslehantering AB.

Appendix C

Audit of the KBS-3H interaction matrix against the BENIPA FEP list (granite)

As described in Section 3.4, an audit of the interaction matrix for KBS-3H is performed against the independently-derived BENIPA FEP List /EC 2001/, which provides a comprehensive list of bentonite barriers related FEPs in integrated performance assessment. The total number of BENIPA FEPs is 49. They aim to cover all those FEPs in the NEA International FEP database /NEA 2000/ which are considered to be relevant for bentonic materials in a deep repository in crystalline rock in the context of the BENIPA project. The BENIPA FEPs are classified in six categories (Table C-1):

- Generic (G, 3 FEPs).
- Features and properties (F, 4 FEPs).
- Processes: alteration and evolution of buffer and backfill (PA, 10 FEPs).
- Processes: thermo-mechanical and radiation (PT, 6 FEPs).
- Processes: chemical, biological and transport (PC, 17 FEPs).
- Events (E, 9 FEPs).

The procedure for the performed audit is based on the mapping of the BENIPA FEPs (columns 1 and 2 in Table C-1) onto the elements of interaction matrix for KBS-3H (column 3 in Table C-1). In case no explicit map was possible, a comment is given to explain any differences related to the scope of the analysis, the naming/grouping of FEPs, or the level of detail involved. The results of the audit can be summarised as follows:

- For the majority of the BENIPA FEPs (33), one or several direct counterparts can be found in the interaction matrix for KBS-3H.
- For 9 BENIPA FEPs, only an implicit map to one or several elements in the interaction matrix for KBS-3H can be established.
- 6 BENIPA FEPs were found to be outside the scope of the present study (e.g. intrusion of buffer into failed canister, water turnover in canister, radionuclide transport, etc).
- 1 BENIPA FEP, related to the settlement or sinking of backfill (e.g. crushed rock and bentonite), was found not to be relevant for the KBS-3H concept.

Table C-1. List of BENIPA FEPs (for a granitic medium) and mapping to the interaction matrix for KBS-3H.

BENIPA FEP list (granite)		KBS-3H FEP list
Generic		
G1	Boundary conditions	2.2, 10.10 [1]
G2	Evolution of buffer and backfill	3.3, 4.4, 5.5
G3	THMCB processes	numerous FEPs
Features and properties		
F1	Properties of buffer and backfill	3.3, 5.5
F1.2	Impurities and minor components in buffer and backfill materials	3.3, 5.5
F1.3	Stray materials and contamination of buffer and backfill	5.5
F2	Groundwater chemistry	9.9
Processes: alteration and evolution of buffer and backfill		
PA1	Resaturation	8.3, 8.4, 8.5

BENIPA FEP list (granite)		KBS-3H FEP list
PA2	Swelling	3.10, 3.12, 3.13, 4.3, 13.3, 13.10, 13.12
PA3	Dilution of buffer or backfill	12.3 [1]
PA4	Chemical alteration	4.3, 4.13
PA4.2	Interaction with cementitious materials	11.4
PA5	Thermal degradation	7.3, 7.13
PA5.2	Cementation due to interaction with water vapour	implicitly addressed in 7.3, 7.13 [1]
PA6	Erosion	6.3, 6.13, 8.3, 8.5, 8.13
PA7	Settlement (sinking of backfill)	not relevant [1]
PA8	Piping	6.3, 6.13, 8.3, 8.5, 8.13
Processes: thermo-mechanical and radiation		
PT1	Heat generation and temperature	7.3, 7.4, 7.5, 7.7
PT2	Radiation effects and radiolysis	1.2–1.13
PT3	Thermo-hydro-mechanical evolution of near-field rock	3.10, 4.10, 6.10, 7.10, 8.10, 13.10, 7.8, 8.7
PT4	Movement of canister	3.2
PT5	Intrusion of buffer into failed canister	outside scope of present study [1]
PT6	Mechanical interaction with corrosion products	2.3, 2.5, 12.3, 12.5
Processes: chemical, biological and transport		
PC1	Chemical evolution and water chemistry	4.4, 4.9, 9.4, 9.13, 13.9
PC2	Radionuclide transport	outside scope of present study [1]
PC3	Solubility and speciation	4.5, 5.4, 13.5, 5.13
PC4	Sorption	3.4
PC5	Diffusion	3.4
PC5.2	Anionic exclusion	implicitly included in 3.4 [1]
PC5.3	Surface diffusion	
PC5.4	Matrix diffusion	
PC6	Coupled transport phenomena	3.4
PC7	Chemical interaction with corrosion products	12.3, 12.5
PC8	Flow through buffer or backfill	3.4, 6.4, 12.8
PC9	Water turnover in canister	outside scope of present study [1]
PC10	Redox front	implicitly included in 1.4, 4.9, 9.4
PC11	Gas generation and transport	3.6, 4.6, 6.3, 6.4, 13.6, 6.13, 11.6, 12.6
PC12	Colloid generation and transport	3.4, 3.5, 5.4, 13.4, 13.5, 5.13
PC13	Microbial activity	implicitly included in 4.2, 4.6, 4.12, 9.12 [1]
PC14	Methylation	implicitly included in 9.4 [1]
Events		
E1	Poor emplacement of buffer or backfill	3.3, 13.13
E2	Uneven saturation or swelling of buffer or backfill	3.2
E3	Cave in	3.10, 4.10
E4	Earthquakes and faulting	outside scope of study [1]
E4.2	Liquefaction	
E5	Preferential pathways in buffer or backfill	3.6, 13.6, 6.3, 6.13, 8.3, 8.13
E6	Intrusion of groundwater with very low or high ionic strength	implicitly included in 9.4 [1]
E7	Intrusion of oxidising groundwater	implicitly included in 9.4 [1]
E8	Permafrost	outside scope of study [1]

[1] Special comments to Table C-1 see next page.

[1] Special comments to Table C-1:

- The diagonal elements 2.2 (‘Canister’) and 10.10 (‘Near-field rock’) of the interaction matrix for KBS-3H can be considered as boundary conditions for the system envisaged.
- The BENIPA FEP No. PA3 (‘Dilution of buffer and backfill’) refers to swelling of bentonite into surrounding cavities and associated lowering of the density of the buffer. In the interaction matrix for KBS-3H, this process is addressed by matrix element No. 12.3, describing (hindrance to) swelling of bentonite into the voids between the perforated supercontainer and the tunnel walls.
- The BENIPA FEP No. PA5.2 (‘Cementation due to interaction with water vapour’) is implicitly addressed in the KBS-3H matrix elements No. 7.3 and 7.13 by considering the effects of temperature on the swelling pressure of bentonite.
- The BENIPA FEP No. PA7 refers to the settlement or sinking of the backfill (e.g. crushed rock and bentonite). This is of no relevance for the bentonite buffer.
- The present study is focused on the time period prior to canister breaching. The issues addressed in the BENIPA FEP No. PT5 (‘Intrusion of buffer into failed canister’), PC2 (‘Radionuclide transport’) and PC9 (‘Water turnover in canister’) are, therefore, outside the scope of the present study.
- None of the BENIPA sub-FEPs No. PC5.2 (‘Anionic exclusion’), PC5.3 (‘Surface diffusion’) and PC5.4 (‘Matrix diffusion’) are explicitly included in the interaction matrix for KBS-3H. These phenomena must, however, be taken into account in the analysis of ion diffusion in bentonite, i.e. they are considered to be implicitly included the KBS-3H matrix element No. 3.4.
- BENIPA FEP No. PC13 (‘Microbial activity’) is implicitly taken into account in a number of KBS-3H matrix elements, for example gas generation by microbial degradation of organics (4.6) and microbially-mediated corrosion (4.2, 4.12, 9.12).
- Specific issues related to the geochemical interaction between groundwater and bentonite porewater (BENIPA FEP No. PC14 ‘Methylation’, E6 ‘Intrusion of groundwater with very low or high ionic strength’ and E7 ‘Intrusion of oxidising groundwater’) are considered to be implicitly addressed in the KBS-3H matrix element No. 9.4 ‘Exchange of species’.
- Issues related to geodynamics (BENIPA FEP No. E4, ‘Earthquakes and faulting’ and associated FEP No. E4.2 ‘Liquefaction’) or climate changes (BENIPA FEP No. E8, ‘Permafrost’) are outside the scope of the present study.

Appendix D

Description of excavation damaged zone (EDZ) around a KBS-3H deposition DRIFT

PM KBS-3H Safety Case
10/2004

Author	Checked by	Approved by
Jorma Autio	Margit Snellman	Reijo Riekkola
date	date	date
4.11.2004	4.11.2004	4.11.2004

1 Background

Excavation damaged zone EDZ adjacent to the surface of KBS-3H deposition drifts may have an impact on the transport of radionuclides and gas flow. It has been estimated that EDZ is not likely to be a significant advective transport route of radionuclides, however it may have a significant role in flow of gases, e.g. corrosion products, along the EDZ.

This document is focused on the description of damaged zone EDZ adjacent to surface of deposition drifts. The damage is a result of several rock tool impacts and stress relaxation. In addition to this type of damage the rock around the deposition drifts undergoes deformation caused by the stress relaxation, which includes elastic deformation of rock and displacements of fractures intersecting the holes. These types of deformations are regarded as disturbances and are mainly irreversible.

The extent and properties of excavation damage zone depend on bedrock properties and boring technique, especially cutter head design. The cutter heads used in deposition hole boring can be modified in several ways to produce different type of damage if desired. The results used in this evaluation are based on deposition hole boring in the Research Tunnel at Olkiluoto and Äspö Hard Rock Laboratory where rotary crushing type boring was used. If other boring techniques or cutter head designs are used, the damage may differ from that seen at Äspö and Olkiluoto. The same applies to boring in different type of bedrock although the differences might not be significant. Cluster boring based on using water hydraulic hammers was tested in Oslo and the damage was studied in laboratory. The study indicated that the porosity of the damaged rock was similar to that caused by rotary crushing at Äspö although there were some qualitative differences in larger aperture microfracturing. The results were considered merely indicative because of large heterogeneity of samples and low state of stress at site.

The micro fracturing of samples taken from the experimental deposition holes in the Research Tunnel at Olkiluoto and in the underground Hard Rock Laboratory at Äspö were investigated by using the ^{14}C-polymethylmethacrylate (^{14}C-PMMA) method and scanning electron microscopy (SEM). The porosity, diffusivity and permeability of samples taken from the experimental deposition holes in the Research Tunnel at Olkiluoto were also measured by using He-gas method.

The boring techniques used at Olkiluoto and Äspö have been described in /Autio and Kirkkomäki 1996/ and /Andersson and Johansson 2002/, respectively. The results of previous studies on the properties of EDZ have been presented in /Autio et al. 2003/, and /Autio 1996/. The properties of the most damaged thin zone close to the surface of deposition holes at Olkiluoto has been studied in more detail by /Montoto et al. 2003/.

2 Porosity, microfracturing, fracture apertures

2.1 General

A total of 12 samples were taken from the experimental deposition holes in Prototype Repository Tunnel in Äspö HRL. The samples representing Äspö diorite were taken from different depths and orientations with respect to the stress field. The extent and structure of the EDZ was also very similar to that found in the experimental deposition holes in the Research Tunnel at Olkiluoto. For reference the porosity of the undamaged rock at Äspö determined by using ^{14}C-PMMA method was 0.2–0.3% and in The Research Tunnel 0.1–0.2%.

The porosity was determined from autoradiographs (Figures D-1, D-2 and D-3.) by using the ^{14}C-PMMA method. The depth of the damaged zone was determined by using porosity profiles (Figure D-4). According to the results the EDZ adjacent to the walls of the experimental deposition holes can be divided into three different zones, starting from the excavated surface as follows:

1. Crushed zone (adjacent to the excavated surface, thickness 4 mm).
2. Microfractured zone (beneath the crushed zone, thickness 5 mm).
3. Zone of minor damage (beneath the microfractured zone, thickness 14 mm).

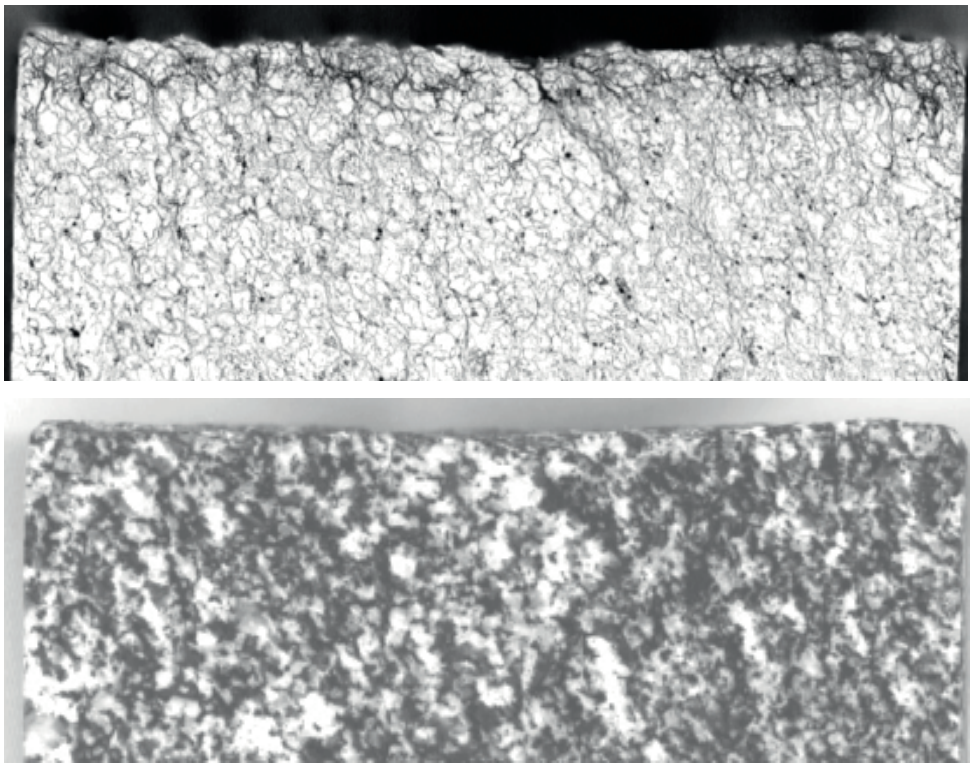

Figure D-1. *Photo image of rock sample from the Research Tunnel at Olkiluoto (above) and corresponding autoradiograph (on top). The section is perpendicular to the axis of experimental deposition hole the excavated surface being on top. The width of sample is 94 mm. Different shades of gray on the autoradiograph correspond to different porosities, the darker the shade, the higher the porosity.*

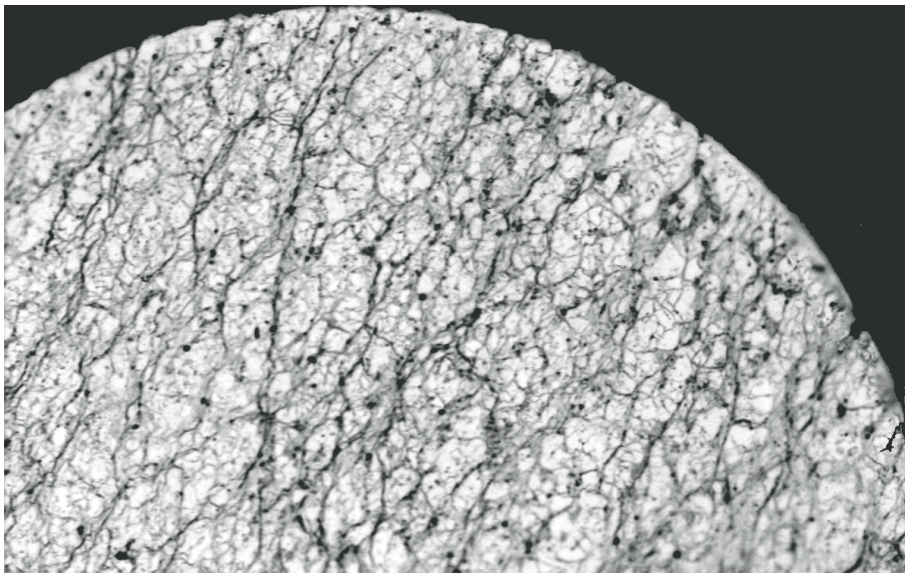

Figure D-2. *Autoradiograph of rock sample from the Research Tunnel at Olkiluoto. The section is parallel to the surface of deposition at depth of 7 mm from the surface. The height of the sample is 47 mm.*

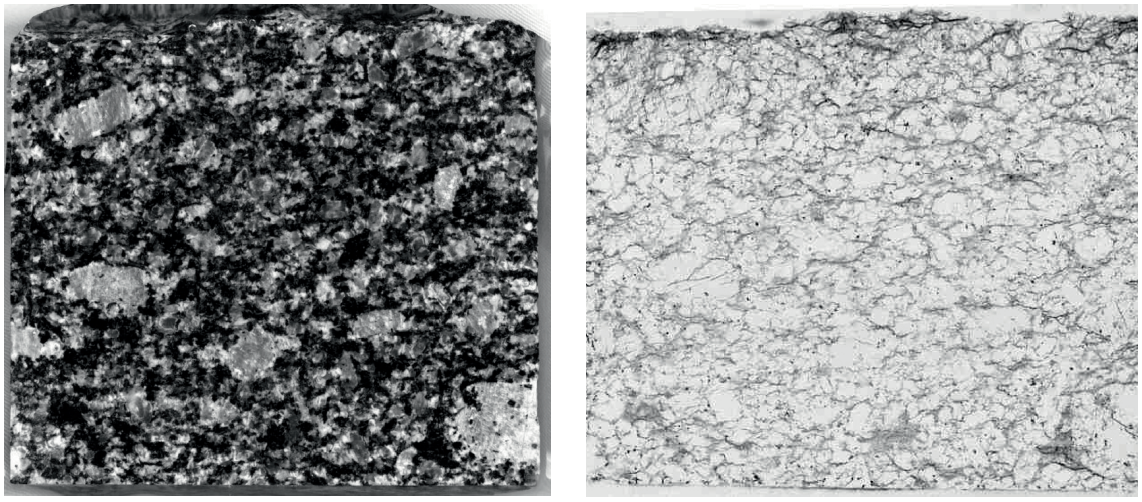

Figure D-3. *Photo image of rock surface (left) and corresponding autoradiograph (right) from Äspö HRL. The section is perpendicular to the axis of experimental deposition hole the excavated surface being on top. The width of sample is 94 mm.*

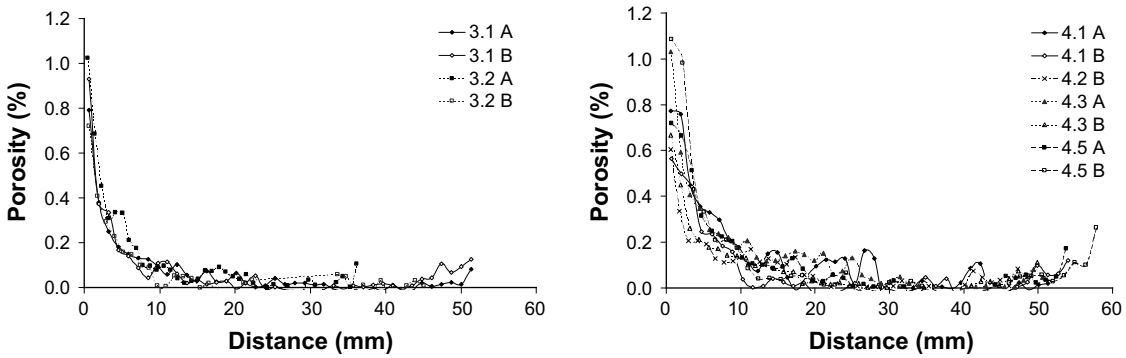

Figure D-4. *Additional porosity in rock determined by using ^{14}C-PMMA-method with respect to the distance from the surface of the experimental deposition holes 3 and 4 in the Prototype Repository tunnel at Äspö Hard Rock Laboratory. The porosity of undamaged rock was 0.26%.*

2.2 Crushed zone

The thickness of the crushed rock zone is 4 mm and the mean *additional* porosity in the crushed zone is 0.5 % (0.55% ± 0.17). The porosity of the crushed zone immediately adjacent to the surface of deposition holes cannot be determined accurately by using ^{14}C-PMMA method and porosities shown in profiles (e.g. in Figure D-4) in the first few millimetres of the crushed zone are lower than true porosities. Therefore complementary characterization of this zone was carried out fractographically by using image analysis /Montoto et al. 1999, 2003/. According to fractographic characterization of five samples from the Research Tunnel, the porosity of the first two millimetres is in order of 2–4%.

According to fractographic characterization of five samples from the Research Tunnel /Montoto et al. 1999, 2003/ the aperture of 90% of the fracture population is less than 5.4 µm. The over 5.4 µm aperture microfractures, which form 10% of the fracture population in the crushed zone, are located randomly in the crushed zone. Fractures with apertures larger than 10 µm are mainly parallel to the excavated surface. These over 10 µm aperture fractures are not directly connected to each other and don't form a continuous network of microfractures. *However, these larger aperture fractures are connected by under 5 µm aperture fractures* as seen in Figures D-6 and D-7. Microfractures with apertures larger than 5.4 µm are mainly located from the excavated surface to a depth of 2 millimetres.

The mean fracture aperture in the crushed zone is approx. 2 µm and the quantity of microfractures with aperture from 2.17 to 5.4 µm is about 35% of the fracture population, whereas the quantity of microfractures with aperture from 5.5 to 10.8 µm is only few percent of the population (see Figure D-8 for example). Over 90% of the microfracturing appears as intragranular fracturing in felsic minerals.

The mean crack specific surface S_v /Montoto et al. 2003/ ranges from 0.06 adjacent to the surface of the deposition hole to 0.02 μm^{-1} at the depth of few millimetres from the surface**.**

In the crushed zone from hole wall to a depth of 4 mm all the mineral grains were fractured according to qualitative evaluation /Autio et al. 2003/ and both intra- and intergranular fracturing was abundant. The most prominent fracturing in the crushed zone was oriented parallel to the hole surface at depth from 1 to 5 mm as seen in Figures D-5, D-6 and D-7. However the parallel orientation was not quantified with confidence by using in the fractographic characterization, although some results implied it as shown in Figures D-8 and D-9. The apertures of these fractures varied between 10 and 30 micrometres. Brittle quartz grains were crushed in the vicinity of the hole wall and lamellaes of biotites were opened and bended.

The difference between the structure of minerals in the crushed zone and undisturbed rock is clear. The apertures of a few intrafissures of potassium feldspar grains were from 5 to 20 µm in size also in the undisturbed rock, but the apertures of grain boundaries and pores and fissures were not detectable in the undisturbed zone because the apertures were less than a micrometre.

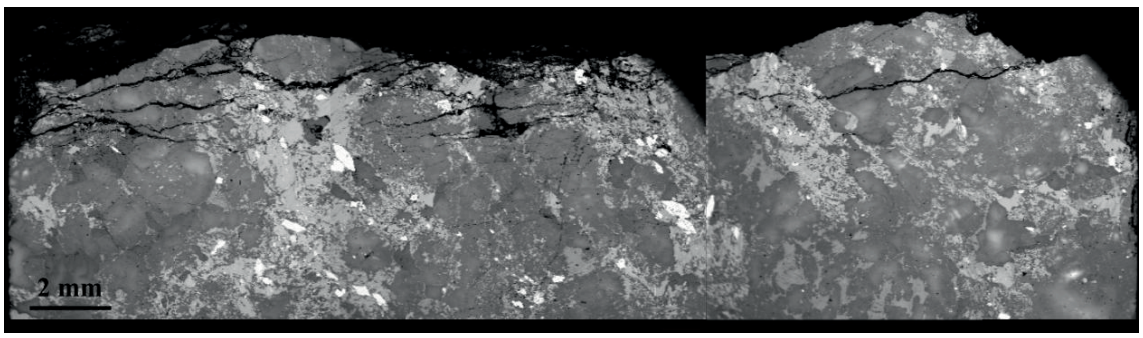

Figure D-5. *BSE images of Sample 4.3A showing fractures extending parallel to hole wall surface. Overview of crushed area. The fracture apertures were detected to be tens of micrometres. Magnification is 10x.*

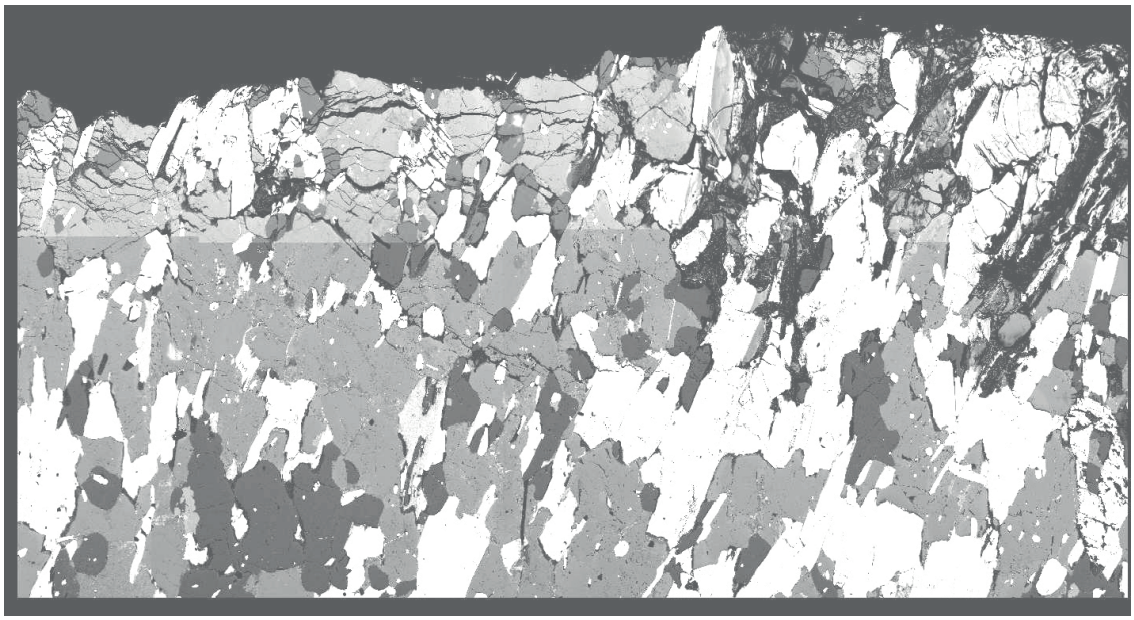

Figure D-6. *Scanning electron microscopical image of a section taken perpendicular to the disturbed surface (disturbed surface at top). The width of the image is approx. 7 mm.*

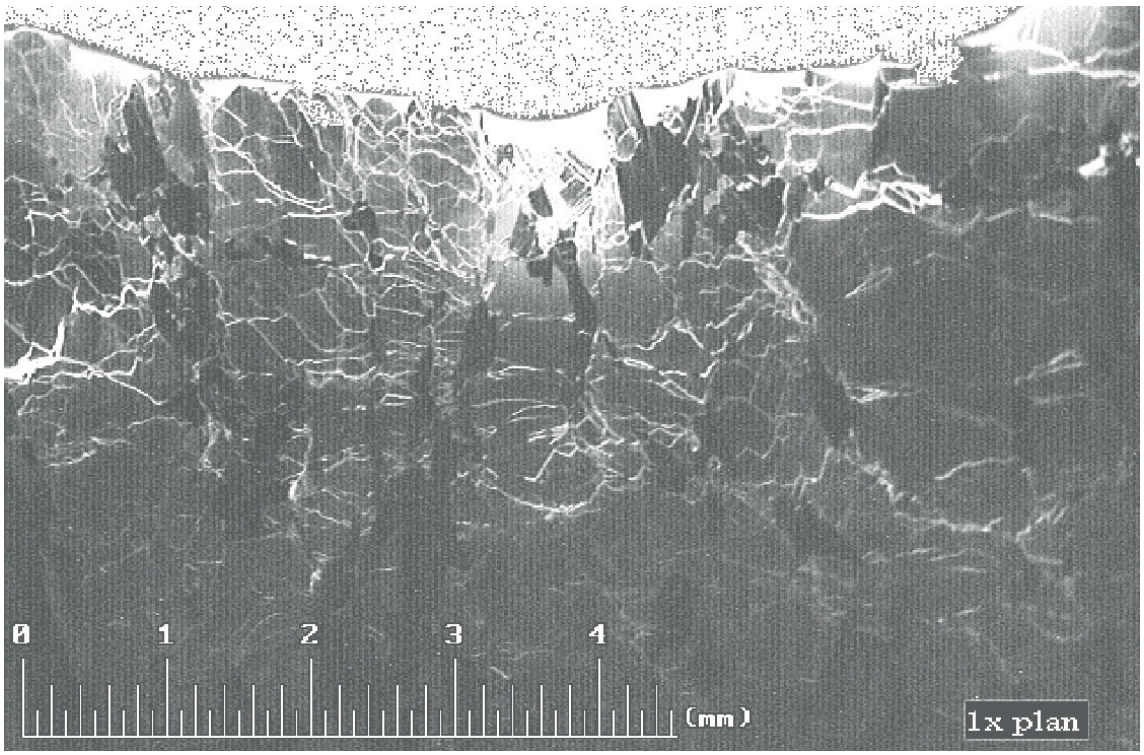

Figure D-7. *Fluorescene thin section image taken perpendicular to the disturbed surface (disturbed surface at top).*

2.3 Microfractured zone

The thickness of the microfractured zone starting from the crushed zone is 5 mm and the mean *additional* porosity in the fractured zone is approx. 0.2% (0.18% ± 0.10) /Autio et al. 2003/.

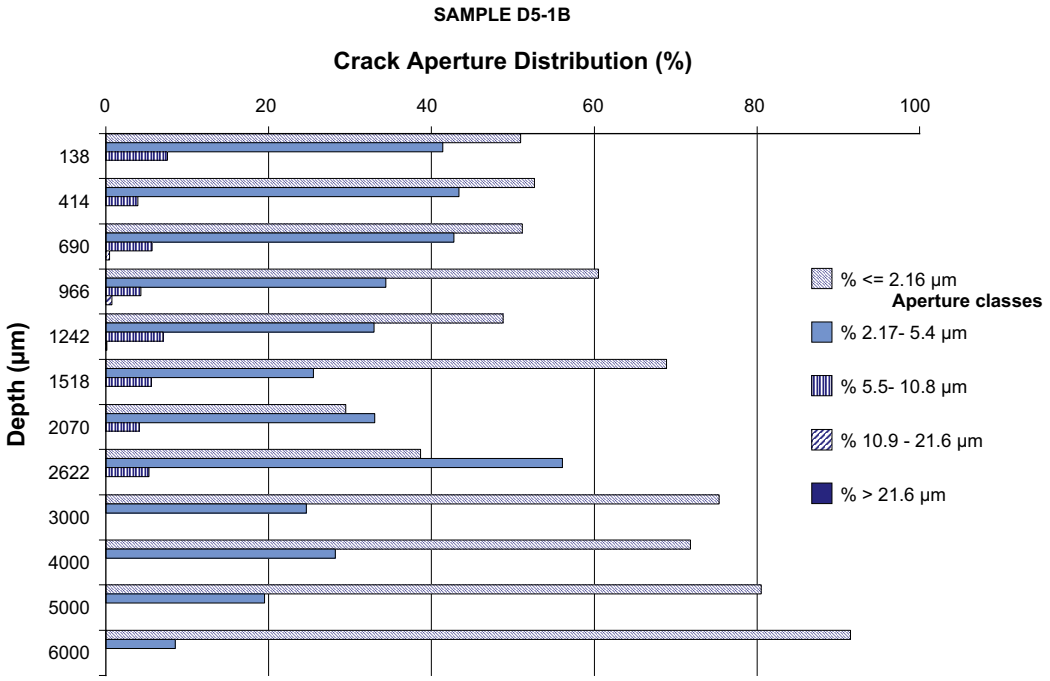

Figure D-8. *Fracture aperture distribution on the basis of microscopy and image analysis /Montoto et al. 1999/.*

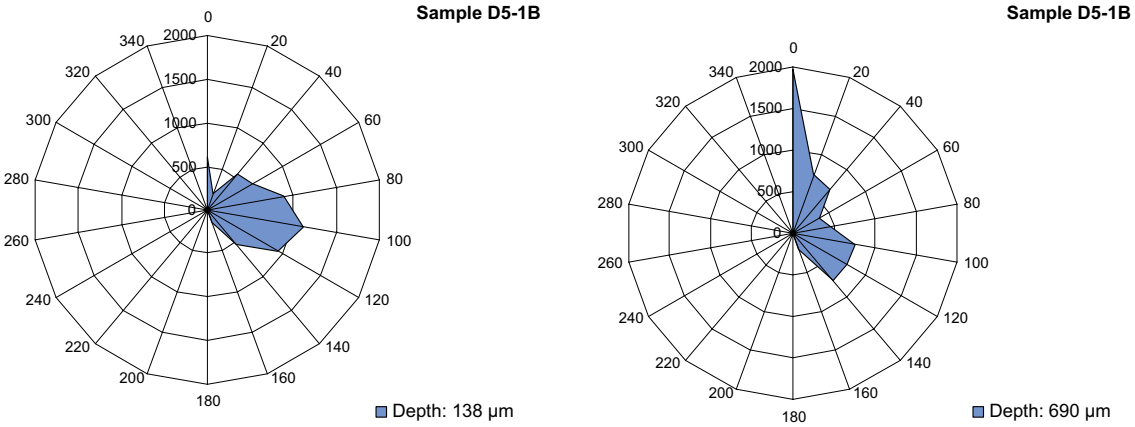

Figure D-9. *Examples of fracture orientation with respect to sum of fracture traces in µm at two different depths 0.138 and 0.690 mm. Fracture orientation is calculated with respect to the direction of the excavated surface (0° is parallel to surface) /Montoto et al. 1999/.*

The aperture of over 60% of fracture population is less than 2.16 µm. The crack specific surface is in the range of 0.004 μm^{-1}, being about one order of magnitude lower than in crushed zone /Montoto et al. 2003/.

2.4 Zone of minor damage

The porosity in the zone of minor damage zone is not significantly higher than the porosity of the undisturbed rock although slight differences can be seen in the porosity profiles (see Figure D-4). The thickness of the zone of minor damage starting from the microfractured zone is about 14 mm. Damage can be observed qualitatively in the form of increased fracture apertures, but no significant quantitative differences can be measured.

3 Permeability and diffusivity

Diffusivity and permeability of seven different granitic rock types were measured using He-gas method and the porosity was determined by using several other techniques including water immersion techniques and ^{14}C-PMMA method /Autio et. al 2003/. Results represented seven different crystalline rock types (gneissic tonalite, rapakivi granite, muscovite granite, porphyritic granodiorite, tonalite, mica gneiss and Palmottu granite).

The average values of the EDZ and Undamaged rock in full-scale experimental deposition holes at Olkiluoto Research Tunnel in Finland are shown separately in Figure D-10. The diffusivity and permeability of samples taken from the experimental deposition holes at Äspö was estimated using two empirical relationships; one between porosity and permeability and another between porosity and diffusivity. These were derived from the abovementioned set of results using Darcy's law type relationship between porosity and permeability and Archie's law type relationship between porosity and diffusivity.

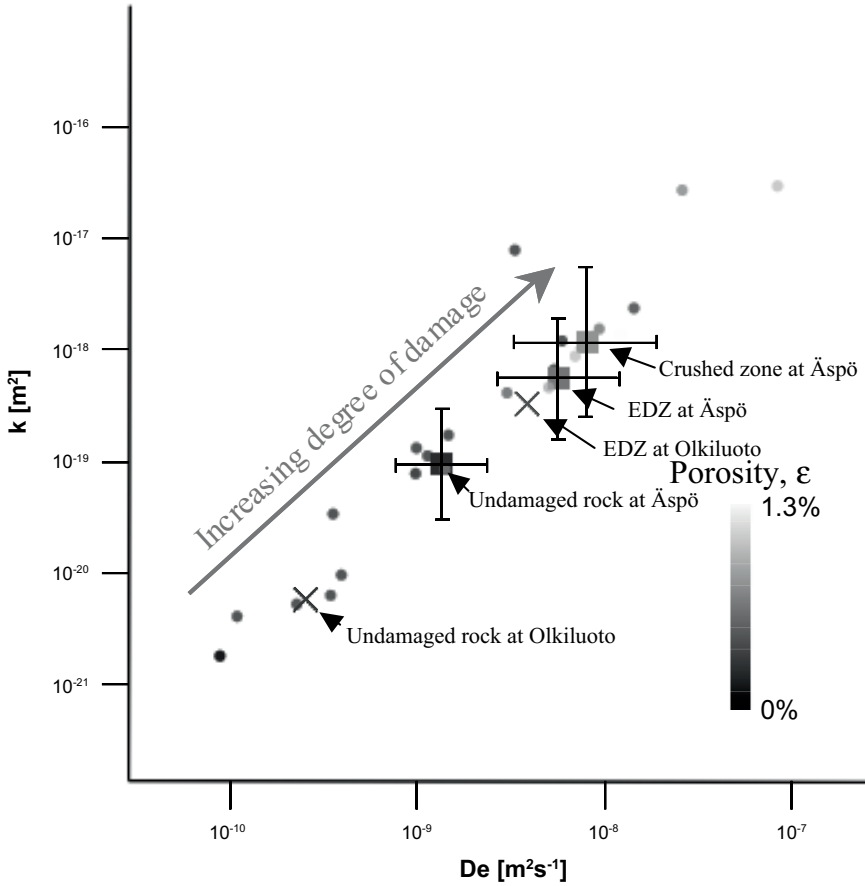

Figure D-10. *Results of effective diffusion coefficient (D_e) of helium in pore space filled with nitrogen, permeability (k) and porosity (ε, in gray scale) measurements presented in Table II representing eight different crystalline rock types (gneissic tonalite, rapakivi granite, muscovite granite, porphyritic granodiorite, tonalite, mica gneiss and Palmottu granite) are shown as dots. The average values of the EDZ and Undamaged rock in full-scale experimental deposition holes at Olkiluoto Research Tunnel in Finland are shown as crosses (ε = 0.34%, $D_e = 3.97 \cdot 10^{-9}$ m^{2}s^{-1}, $k = 2.96 \cdot 10^{-19}$ m^2, and ε = 0.14%, $D_e = 2.63 \cdot 10^{-10}$ m^{2}s^{-1}, $k = 5.16 \cdot 10^{-21}$ m^2, respectively). The estimated values of undamaged rock, EDZ, and the crushed zone, which is part of the EDZ, in samples taken from the experimental deposition holes at Äspö (ε = 0.26%, $D_e = 1.4 \cdot 10^{-9}$ m^{2}s^{-1}, $k = 8.4 \cdot 10^{-20}$ m^2; ε = 0.64%, $D_e = 6.0 \cdot 10^{-9}$ m^{2}s^{-1}, $k = 4.9 \cdot 10^{-19}$ m^2 and ε = 0.80%, $D_e = 8.5 \cdot 10^{-9}$ m^{2}s^{-1}, $k = 1.0 \cdot 10^{-18}$ m2 respectively) are shown as squares with error bars representing the 95% confidence intervals.*

References

Andersson C, Johansson Å, 2002. Boring of full-scale deposition holes at the Äspö Hard Rock Laoratory, Operational experiences including boring performance and a work time analysis. SKB Technical Report TR-02-26, Svensk Kärnbränslehantering AB.

Autio J, 1996. Characterization of the excavation disturbance caused by boring of the experimental full scale deposition holes at TVO-Research Tunnel, Report POSIVA-96-09, Posiva Oy, Helsinki.

Autio, J, Kirkkomäki, T, 1996. Boring of full-scale deposition holes using a novel dry blind boring method. Report POSIVA-96-07, Posiva Oy, Helsinki.

Autio J, Hjerpe T, Siitari-Kauppi M, 2003. Porosity, Diffusivity and Permeability of EDZ in Crystalline Rock and Effect on the Migration in a KBS-3 Type Repository. CLUSTER conference on "Impact of the EDZ on the performance of radioactive waste geological repositories", Luxembourgh 3–5 November 2003.

Montoto M, Rodriguez-Rey A, Matrtinez-Nistal A, Diez-sarriá I, 1999. Fractographic characterization by quantitative microscopy of the excavation disturbance caused by boring of the experimental full scale deposition holes in the Research Tunnel at Olkiluoto, Posiva Working Report 99-69, Posiva Oy, Helsinki.

Montoto M, Rodriguez-Rey A, Autio J, 2003. Microfractographic characterization of the excavation damage caused by boring of the experimental full scale deposition holes in the Research Tunnel at Olkiluoto. CLUSTER conference on "Impact of the EDZ on the performance of radioactive waste geological repositories", Luxembourgh 3–5 November 2003.

Appendix E

Olkiluoto site data for KBS-3H design and analyses

PM KBS-3H Safety Case
9/2004

Author	Checked by	Approved by
Timo Vieno	Margit Snellman	Reijo Riekkola
date	date	date
1.11.2004	4.11.2004	4.11.2004

At Olkiluoto, a KBS-3H type repository may be constructed as a one-storey repository at a depth of about 400 metres or as a two-storey repository at depths of about 400 and 500 metres.

The most comprehensive general compilations of Olkiluoto data for KBS-3H design and analyses are provided by

- Posiva 2003. Baseline conditions at Olkiluoto. POSIVA 2003-02.
- Johansson, E, Äikäs, K, Autio, J, Hagros, A, Malmlund, H, Rautakorpi, J, Sievänen, U, Wanne, T, Anttila, P, Raiko, H. 2002. Preliminary KBS-3H layout adaptation for the Olkiluoto site – Analysis of rock factors affecting the orientation of a KBS-3H deposition hole. Posiva Working Report 2002-57.

Additional references are given below when specific features of the Olkiluoto site are discussed.

Rock fracturing

The rock mass between fracture zones is sparsely fractured with a fracture density of 1–3 fractures per metre. Occasionally vein-like sections with 3–10 fractures per metre are encountered. Fractures are mostly tight or filled. Several fracture sets with different orientations (incl. subvertical, moderately dipping and subhorizontal) have been identified. Subhorizontal and gently dipping fractures dominate in borehole data.

Leakages during operation phase

A KBS-3H deposition drift at Olkiluoto may intersect several fractures and fracture zones with a transmissivity of the order of 10^{-8} m^2/s. Leakages into an open drift are difficult to predict accurately, as the outcome of the predictions depend, for example, on orientation, skin effect and the influence radius or gradient used in the calculations. For a deposition drift of 300 metres, following values may be used as a design basis of leakages without grouting or other sealing of the rock.

- several point leakages of ~0.1 litres/min,
- a few fractures or fracture zones leaking ~1 litre/min,
- occasionally a fracture zone leaking ~10 litres/min may be intersected. Such locations are presently considered clearly unsuitable for emplacement of KBS-3H disposal containers because of potential problems related to piping and erosion of the buffer as well as to displacement of the distance block due hydrostatic pressure. (Note that the tolerable inflow rate may be significantly lower than 10 litres/min, maybe even as low as 0.1 litre/min.) The high inflow sections may be unsuitable for locations of ordinary distance blocks, as well. Therefore, leaking fracture zones must be sealed or special arrangements, for example extra distance blocks, may be needed within the deposition drift.
- total leakage into the drift up to 10 litres/min,
- long sections of the drift may be dry, too
- relative humidity within the drift during the emplacement and operation phase is expected to be ~ 100% without ventilation.

Systematic grouting of the rock around the deposition drift with a large number of out-of-profile injection boreholes is considered unacceptable from the point of view of the safety case, as suitable low pH injection materials are still under development and because in the long-term the degrading injection boreholes may become preferential flow pathways.

Flow rates after saturation

Postclosure flow rates around the drift and solute transport in the fully saturated state have been discussed by /Nordman and Vieno 2004/. In the saturated state the hydraulic gradient around the drift may be taken as ~ 1%. The flow rate around the drift along a fracture with a transmissivity of ~ 10^{-8} m^2/s is thus ~ 6 litres/yr. From the point of view of radionuclide transport, such a flow rate (or even higher) is acceptable provided that the buffer is swollen and saturated, and no erosion or piping of the buffer occurs. The main resistance for solute transport between the canister and rock is then the boundary layer (film) resistance between the stagnant porewater in the buffer and the groundwater flowing along the fracture around the drift /Vieno and Nordman 2000/.

Geochemistry

Groundwater salinity issues and upconing of deep saline groundwater during construction and operation have been discussed by /Vieno 2000/ and /Vieno et al. 2003/. Presently salinity of groundwater at depths of 400 and 500 metres at Olkiluoto ranges from 10 to 25 g/litre of Total Dissolved Solids (TDS). Groundwater is of the Na-Cl and Ca-Na-Cl types.

Groundwater flow simulations indicate that locally the salinity of groundwater in the vicinity of the excavations may rise to 25–45 g/litre due to upconing during construction and operation, even if the excavations were tightly grouted to limit inflows. Accordingly, the design basis salinity should be at least 35 g/litre, and hopefully even higher.

At Olkiluoto, the deep, most saline groundwaters at a depth of about 800 metres contain a large amount (near saturation) of dissolved gases (methane, hydrogen).

In addition to a large salinity variation and increasing content of dissolved gases with depth the groundwater chemistry at Olkiluoto is characterised by reducing sulphidic conditions already at shallow depth, which in the saline groundwater is changing to a methanic system almost at –300 mV /Pitkänen et al. 2004/. Microbes are fundamental for the redox processes in the groundwaters at Olkiluoto. The microbiological studies have shown that methanogens and acetogens are found in SO_4-poor, brackish and saline waters where high concentrations of CH_4

and H_2 are present. Methanogenesis show increasing importance in saline groundwater. The pH seems to be controlled by the thermodynamic equilibrium with calcite in fractures, which is the most common fracture-filling mineral at Olkiluoto. The present pH in the saline groundwater is at a level of 7.5–8.2.

Rock mechanical analyses

In the previous KBS-3V analyses, the stress/strength ratio of the Olkiluoto bedrock has been of some concern, if the repository were excavated at a depth > 600 metres. At depths of about 400 and 500 metres, the analyses indicate fairly small rock mechanical effects for the KBS-3H deposition drift /Johansson et al. 2002/. The optimal orientation of the drift is parallel to the maximum principal stress.

Thermal analysis

/Ikonen 2003/ has performed a thermal analysis for a KBS-3H type repository at Olkiluoto. The thermal conductivity, heat capacity and thermal diffusivity of the Olkiluoto rock at the temperature of 60°C are 2.61 W/m/K, 784 J/kg/K, and $1.21 \cdot 10^{-6}$ m^2/s, respectively. For the thermal conductivity sof the buffer, a value of 1.0 W/m/K has been used in the analysis.

In the thermal dimensioning analysis the maximum temperature at the canister surface has been set to 90°C in order to have a safety margin of 10°C to the design basis maximum temperature of 100°C. With Posiva's planned disposal schedule, the length of the distance blocks needs to be 5.35 metres between disposal containers containing spent BWR fuel with an initial heat power of 1,700 W per canister, if the spacing between the drifts is 25 metres. With a drift spacing of 40 metres, the length of the distance blocks needs to be 3.05 metres. For disposal containers containing PWR fuel with an initial heat power of 1,370 W per canister, the required length of the distance blocks is 4.65 metres (drift spacing of 25 metres) and 2.55 metres (drift spacing of 40 metres), respectively.

References

Ikonen K, 2003. Thermal analyses of KBS-3H type repository. POSIVA 2003-11.

Johansson E, Äikäs K, Autio J, Hagros A, Malmlund H, Rautakorpi J, Sievänen U, Wanne T, Anttila P, Raiko H, 2002. Preliminary KBS-3H layout adaptation for the Olkiluoto site – Analysis of rock factors affecting the orientation of a KBS-3H deposition hole. Posiva Working Report 2002-57.

Nordman H, Vieno T, 2004. Equivalent flow rates from canister interior into the geosphere in a KBS-3H type repository. Posiva Working Report 2004-06.

Pitkänen P, Partamies S, Luukkonen A, 2004. Hydrogeochemical interpretation of baseline groundwater conditions at the Olkiluoto site. POSIVA 2003-07.

Posiva, 2003. Baseline conditions at Olkiluoto. POSIVA 2003-02.

Vieno T, 2000. Groundwater salinity at Olkiluoto and its effects on a spent fuel repository. POSIVA 2000-11.

Vieno T, Nordman H, 2000. Updated compartment model for near-field transport in a KBS-3 type repository. Posiva Working Report 2000-41.

Vieno T, Lehikoinen J, Löfman J, Nordman H, Mészáros F, 2003. Assessment of disturbances caused by construction and operation of ONKALO. POSIVA 2003-06.